BULETINUL INSTITUTULUI POLITEHNIC DIN IAŞI

Volumul 68 (72)
Numărul 1-4

Secția
ŞTIINŢA ŞI INGINERIA MATERIALELOR

2022 **Editura POLITEHNIUM**

BULETINUL INSTITUTULUI POLITEHNIC DIN IAŞI
PUBLISHED BY
“GHEORGHE ASACHI” TECHNICAL UNIVERSITY OF IAŞI
Editorial Office: Bd. D. Mangeron 63, 700050, Iaşi, ROMANIA
Tel. 40-232-278683; Fax: 40-232-211667; e-mail: buletin-ipi@tuiasi.ro

BULETINUL INSTITUTULUI POLITEHNIC DIN IAŞI
BULLETIN OF THE POLYTECHNIC INSTITUTE OF IAŞI
Volumul 68 (72), Numărul 1-4 2022

Secția

ŞTIINŢA ŞI INGINERIA MATERIALELOR

S U M A R

Pag.

ADRIAN-PETRU TEODORIU, LEANDRU-GHEORGHE BUJOREANU şi GHEORGHE BĂDĂRĂU, Construcția unui laminor cu patru role utilizat în studiul curgerii fluidelor ne-newtoniene (I). Componentele generale și sistemul mecanic (engl., rez. rom.) 9

ADRIAN-PETRU TEODORIU, LEANDRU-GHEORGHE BUJOREANU şi GHEORGHE BĂDĂRĂU, Construcția unui laminor cu patru role utilizat în studiul curgerii fluidelor ne-newtoniene (II). Componentele generale ale părții electronice și programarea acesteia (engl., rez. rom.) 25

RODICA TEODORIU, LEANDRU-GHEORGHE BUJOREANU, ANDREI CUCOȘ şi GHEORGHE BĂDĂRĂU, Studiu experimental al fenomenelor de curgere utilizând un laminor cu patru role (engl., rez. rom.) 41

ELENA BASALIC, IOANA SORINA ENŢUC, CARMEN NEJNERU, RALUCA FLOREA, COSTEL DOREL FLOREA, ANA-MARIA SCRIPCARIU, PETRONELA PARASCHIV şi CIMPOEȘU NICANOR, O Scurtă analiză asupra cunoaşterii mortarelor cu inserţii micro şi nanometrice de diferite geometrii în domeniul ingineriei civile (engl., rez. rom.) 55

NICOLINA MONTELLA, Optimizarea multi-disciplinară a unei nave spațiale pentru coborârea de reintrare în atmosferă de pe orbite terestre joase la o densitate de flux termic constantă (engl., rez. rom.) 63

ILIE COJOCARIU, Cercetări preliminare privind utilizarea magnetitei sintetice în conservarea și restaurarea fierului arheologic. Studiu privind posibilitatea utilizării ferofluidelor pe bază de magnetită sintetică ca medii de lustruire (engl., rez. rom.) 81

TEODORA IRINA BIRNOVEANU, SEBASTIAN MISTREANU, ANA MARIA SCRIPCARIU, ANA-MARIA ROMAN, CIPRIAN PARASCHIV şi NICANOR CIMPOEŞU, Materiale metalice cu capacitate de amortizare pentru aplicații automotive (engl., rez. rom.) 95

BULETINUL INSTITUTULUI POLITEHNIC DIN IAŞI
BULLETIN OF THE POLYTECHNIC INSTITUTE OF IAŞI
Volume 68 (72), Number 1-4 2022

Section

MATERIALS SCIENCE AND ENGINEERING

CONTENTS

Pp.

ADRIAN-PETRU TEODORIU, LEANDRU-GHEORGHE BUJOREANU and GHEORGHE BĂDĂRĂU, The Construction of a Four-Roll Mill Used in the Study of Non-Newtonian Fluid Flows (I). General Components and the Mechanical System (English, Romanian summary) 9

ADRIAN-PETRU TEODORIU, LEANDRU-GHEORGHE BUJOREANU and GHEORGHE BĂDĂRĂU, The Construction of a Four-Roll Mill Used in the Study of Non-Newtonian Fluid Flows (II). Electronic System General Components and Programming (English, Romanian summary) 25

RODICA TEODORIU, LEANDRU-GHEORGHE BUJOREANU, ANDREI CUCOȘ and GHEORGHE BĂDĂRĂU, Experimental Study of Flow Phenomena Using a Four-Roll Mill (English, Romanian summary) 41

ELENA BASALIC, IOANA SORINA ENȚUC, CARMEN NEJNERU, RALUCA FLOREA, COSTEL DOREL FLOREA, ANA-MARIA SCRIPCARIU, PETRONELA PARASCHIV and CIMPOEȘU NICANOR, A Short Introduction Over the Knowledge of Mortars with Micro and Nanometric Inserts of Different Geometries in the Field of Civil Engineering (English, Romanian summary) 55

NICOLINA MONTELLA, Multi-Disciplinary Optimization of a Spacecraft for a Re-Entry Descent from Leo Orbit at Costant Heat Flux Density (English, Romanian summary) 63

ILIE COJOCARIU, Preliminary Research on the Use of Synthetic Magnetite in the Conservation and Restoration of Archaeological Iron. Study on the Possibility of Using Ferrofluids Based on Synthetic Magnetite as Polishing Media (English, Romanian summary) 81

TEODORA IRINA BIRNOVEANU, SEBASTIAN MISTREANU, ANA MARIA SCRIPCARIU, ANA-MARIA ROMAN, CIPRIAN PARASCHIV and NICANOR CIMPOEŞU, Metallic Materials with Damping Capacity for Automotive Applications (English, Romanian summary) 95

BULETINUL INSTITUTULUI POLITEHNIC DIN IAŞI
Publicat de
Universitatea Tehnică „Gheorghe Asachi” din Iaşi
Volumul 68 (72), Numărul 1-4, 2022
Secţia
ŞTIINŢA ŞI INGINERIA MATERIALELOR

THE CONSTRUCTION OF A FOUR-ROLL MILL USED IN THE STUDY OF NON-NEWTONIAN FLUID FLOWS (I). GENERAL COMPONENTS AND THE MECHANICAL SYSTEM

BY

ADRIAN-PETRU TEODORIU, LEANDRU-GHEORGHE BUJOREANU and GHEORGHE BĂDĂRĂU*

“Gheorghe Asachi” Technical University of Iaşi,
Faculty of Materials Science and Engineering, Iaşi, Romania

Received: February 25, 2022
Accepted for publication: March 14, 2022

Abstract. Having as a purpose the preliminary study of the flow of various emulsion type materials we consider that there is no need to use state-of-the-art equipment, very sophisticated and very expensive at the same time. Moreover, at the didactic laboratory level, for putting into evidence of some phenomena it is preferable that the equipment used is reliable, and of course, if possible, to enable the understanding of the constructive principles and the way of operation of other more sophisticated equipment. Through this paper we put into evidence the constructive principles that formed the basis of a simple electromechanical equipment designed for the study of flow of various viscous fluids. There are shown briefly the history of some equipment having the same purpose and some details about the components proposed to be used in the construction of a four-roll mill for flow studying. This paper presents the general components and the mechanical part of the hardware of a piece of equipment which does not aim to be at the level of performances that could be reached in 2022 but it is accessible from the point of view of the price of components used.

Keywords: didactic laboratory equipment, viscous fluids flow, mechanical components, stepper motor, bolt coupling, strobe light, video camera, rotation speed adjusting.

---

*Corresponding author; *e-mail*: gheorghe.badarau@tuiasi.ro

1. Introduction

In the production of laboratory equipment in the materials science field there is always a contradiction between having multiple characteristics and price to be paid for. Some times the capacity of putting into evidence of a phenomenon or, to validate or invalidate a theory is more valuable that the quality of the measurements, the precision of tuning and so on but, this is true only in the early stages of study on a certain material. In the case of making laboratory equipment for didactic purpose many times it is enough to be able to produce and demonstrate a given phenomenon using simple schemes, easier to understand by a student or a pupil.

In the early stages of studying a phenomenon, a piece of equipment designed for another purpose, can sometimes, be very useful for studying something else. For example "the four roller apparatus" (Taylor, 1934) designed by Taylor in view of studying the mechanical steering conditions was found useful for rheological studies. The equipment described in this paper is made following the idea used by Taylor in his so called "four roller apparatus" but having the purpose of putting into evidence the flowing of viscous fluids.

2. Very short history

The first equipment in the family of the four-roll mill was proposed by the scientist G.I.Taylor in 1934, while performing some experiments about the manner two fluids can be stirred together to form an emulsion "in the Cavendish Laboratory through the kindness of Lord Rutherford, to whom the author wishes to express his thanks" (Taylor, 1934).

Taylor referred to his equipment as "four roller apparatus" and designed it, to be capable to obtain inside it an approximately definable fields of flow, more precisely to generate bidimensional shear forces in fluids in view of obtaining emulsions. Today, the name of the equipment used having as a base the same scheme, changed in "four roll mill".

The basic idea is to produce "the deformation and bursting of a drop of one fluid in another, under controlled conditions measuring the interfacial tensions of the two liquids, theirs viscosities and the rate of deformation of the outer fluid" (Taylor, 1934) using parts in motion, in this case, rolls. The scheme of the "four roller apparatus" is given in Fig. 1.

The apparatus was designed for the study of the conditions necessary for bursting a drop of fluid to be emulsioned, placed between four emulsifying fluid flows, having a hyperbolic shape in the cross section, created by rotating rollers immersed in a filled enclosure.

Figure 2 shows the way of deformation of the drop of fluid to be emulsioned by means of biaxial extension in the four roll mill by comparing it with the device using parallel band that uses sharing, device designed also by G.I. Taylor for carrying out the same study.

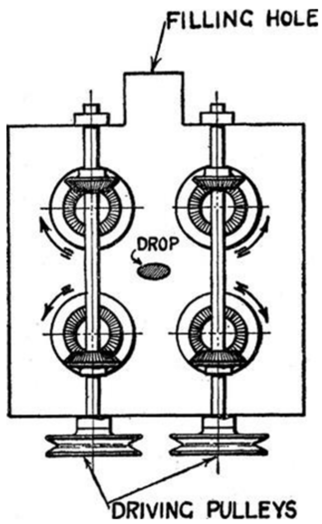

Fig. 1 – Four roller apparatus (Taylor, 1934).

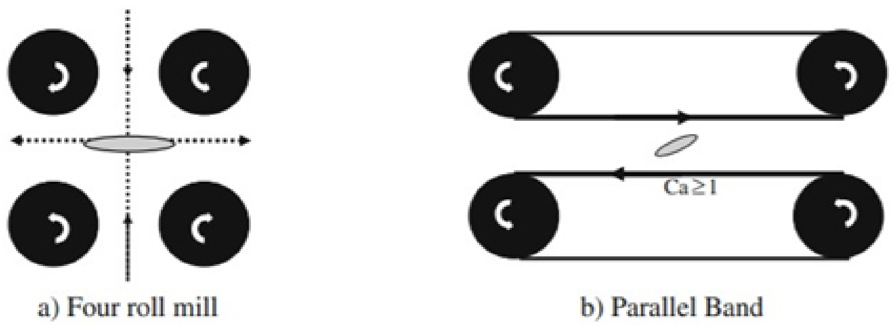

Fig. 2 – Droplet deformation G.I.Taylor, a) Four roll mill and b) Parallel band apparatus. (Mackley, 2010).

This idea of creating extension into a fluid was later used for polymer processing in viscous state, namely for stretching out the polymer chains and implicitly it lead to the designing of other types of equipment.

In this context, Mackley and Keller proposed a new way for obtaining an extension, this time a uniaxial one. They used two opposed jets of polymer exiting from nozzles of 1 mm in diameter and speeds of the order of mm/s. Figure 3 shows the streamline flow for uniaxial extension and the image of a uniaxial birefringent deformation zone in polyethylene.

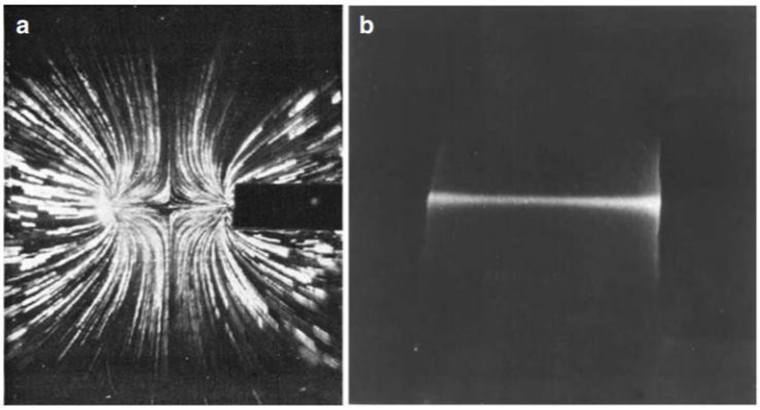

Fig. 3 – Streamline flow for uniaxial extension created by flow into opposed jets; b localised low birefringence associated with polyethylene solution flowing within region of uniaxial extension. (Mackley and Keller 1975).

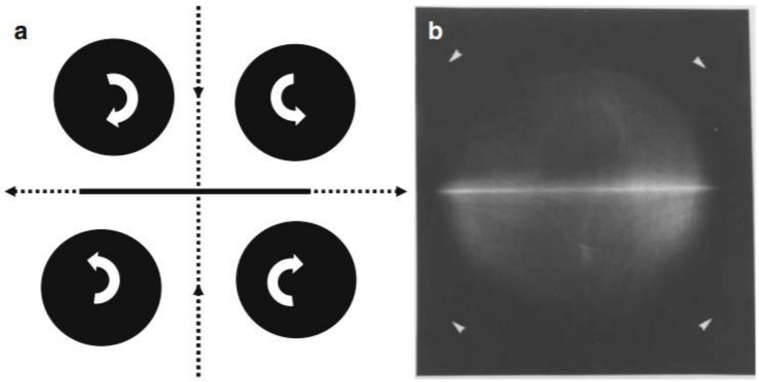

Fig. 4 – a) Schematic of four roll mill and localised birefringence – black continuous line; b) Photograph of localized birefringence – light line (Crowley *et al*., 1976).

It was later proven by experiment that this birefringent zone was associated with a high level of strain in the polymer chains. The reason for this localization was not immediately obvious. Following experiments made by Crowley in 1976 using a four-roll mill revealed very similar results with those obtained by Mackley and Keller.

Figure 4 shows schematically the four-roll mill, the positioning of the birefringent zone and the photograph of this zone. It was deduced that for straightening the chains of polymer they have to be under strain for a sufficient period of time fact that is ensured easily on the symmetry axis in the case of the double jet and in the symmetry plane in the case of the four-roll mill.

More over, in order to achieve high chain extension within an extension flow the applied extensional strain rate must be sufficiently strong to overcome the entropic elasticity of the chain that normally keeps the chain in a random coil configuration and simultaneous to ensures that the applied extensional strain rate acts for a sufficient length of time in order for the chain to have sufficient time to become fully stretched from its original random configuration. This is equivalent to saying that an adequate strain must be applied in order to stretch the chain (Mackley, 2010).

It can be rather surprising that the phenomenon can be observed also in a two roll mill as seen in Fig. 5 but this situation can appear in the conditions explained above. The stagnation point is visible in the flow pattern in the middle of the streamline photograph.

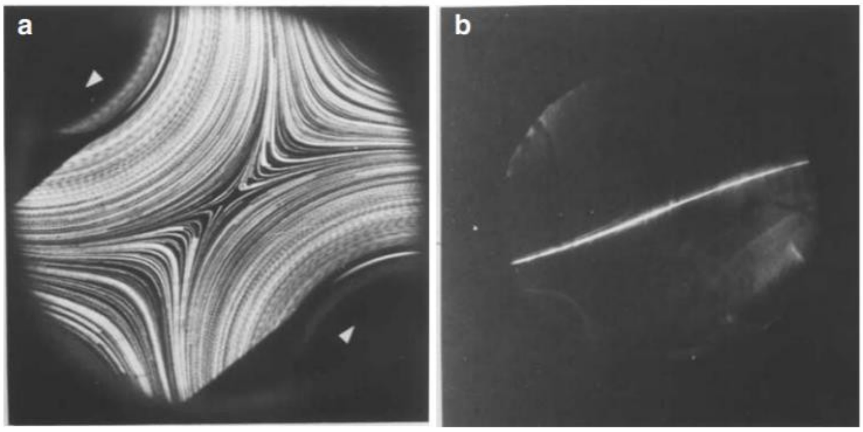

Fig. 5 – a) Streamline photograph of two roll mill flow pattern; b) Photograph of localized flow birefringence within a two roll mill (Frank and Mackley, 1976).

For studying the stagnation point in fluid flows a six roll mill was used by Berry and Mackley. Also theoretical studies concerning the catastrophe theory were carried out using this type of equipment shown in Fig. 6.

Another way to study the flowing phenomena is represented by the so called cross slot device. It was used for the first time by Scrivener in 1979, then by Odell and Carrington in 2006 for polymer solutions and applied by Han Meijer and Veerbeten in 2002 for studying polymer melts (Mackley, 2010).

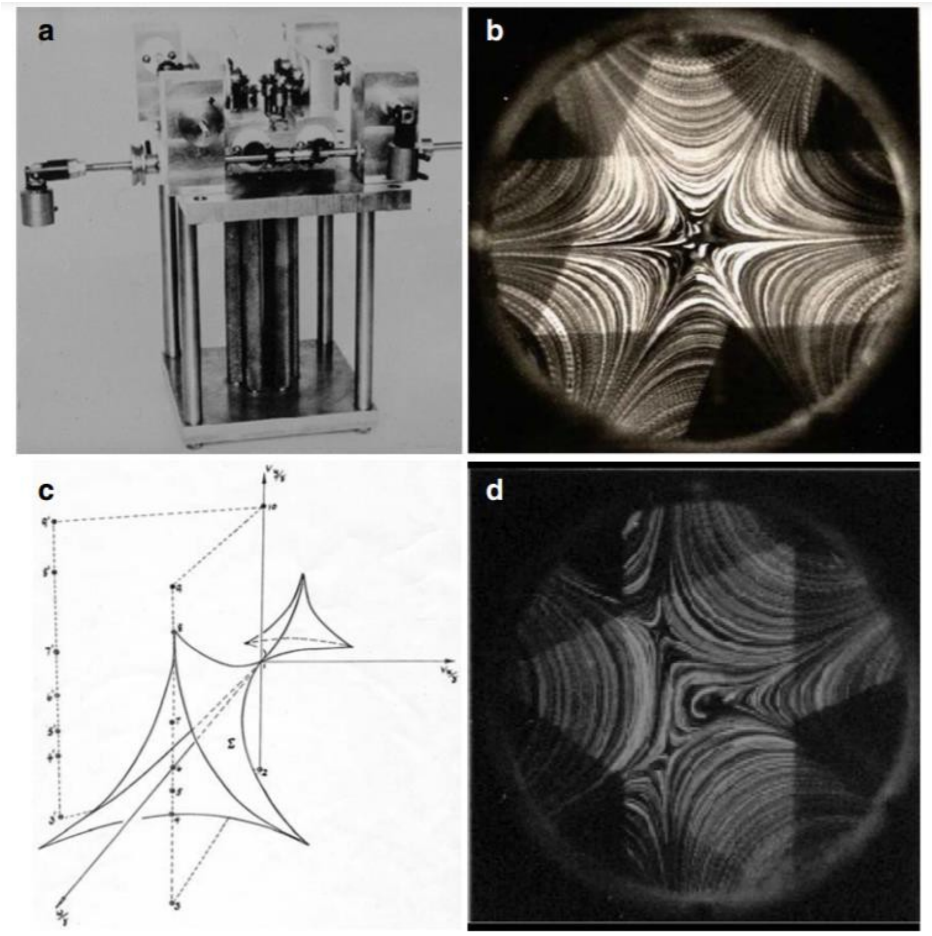

Fig. 6 – The Six Roll mill. a) Photograph of apparatus; b) Photograph of symmetrical Six roll mill flow pattern, the germ of umbilic catastrophe surface; c) Schematic of the elliptic umbilic catastrophe surface. d Photograph of flow with control settings set on the catastrophe surface and showing a flow singularity within the flow (Berry and Mackley, 1977).

Figure 7 shows a schematic of pure shear streamlines superimposed on Cross Slot geometry. Also there can be seen the spatial configuration of the multipass rheometer (MPR) and a photograph of flow birefringence pattern obtained for a certain type of polystyrene.

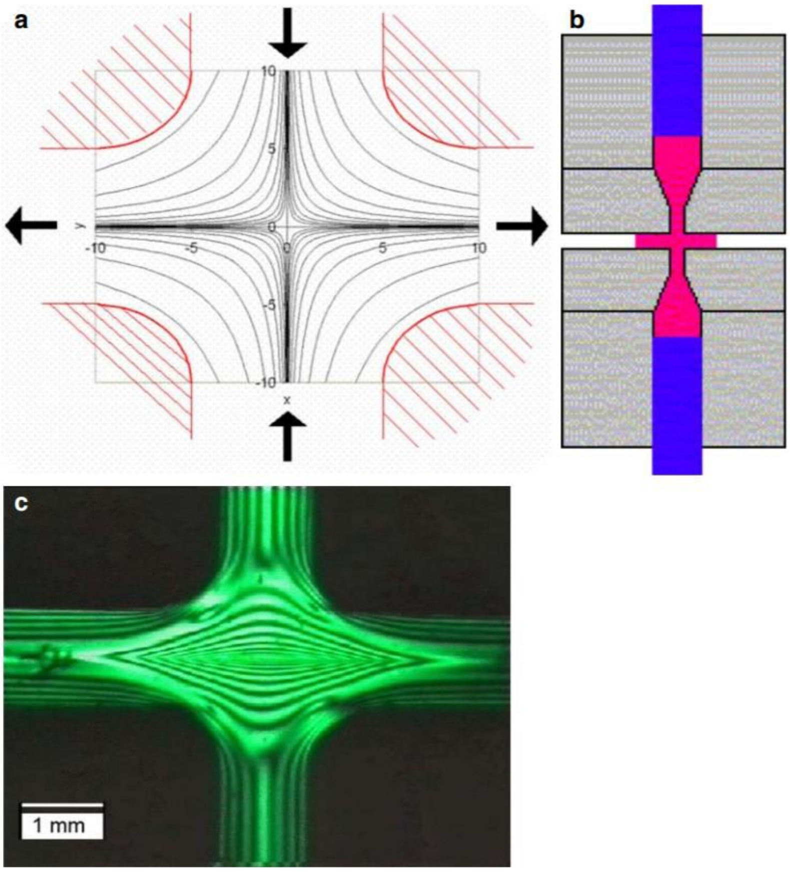

Fig. 7 – The Cross Slot geometry. a) Schematic of pure shear streamlines superimposed on Cross Slot geometry. b) Schematic of Cross Slot MPR configuration. c) Flow birefringence pattern for Dow PS680 polystyrene. Piston velocity of 0.5 mm/s (maximum extension rate = 4.3 s^{-1}). Inlet slit width = 1.5 mm. Section depth = 10 mm. T = 180°C (Mackley, 2010).

In this case the birefringence shows the presence of some lines of delay corresponding to different level of forces in the studied field of flow. The high levels of flowing are positioned in the central zone and near the walls of the device. If the flowing would be Newtonian type, these lines would start from the centre toward the exterior of the stagnation central point. The viscoelasticity produces en elliptic asymmetry with the development of some picks along the symmetry plane fact that shows a highest degree of stretching of polymer chains in this zone.

By numerical methods it is possible to achieve a flowing model very close to the experimental observations. Figure 8 represents by comparison the validity, for this case, of the Pom–Pom numerical model, introduced by

McLeish and Larson in 1998, in the central zone and near the wall and also in the transition zones.

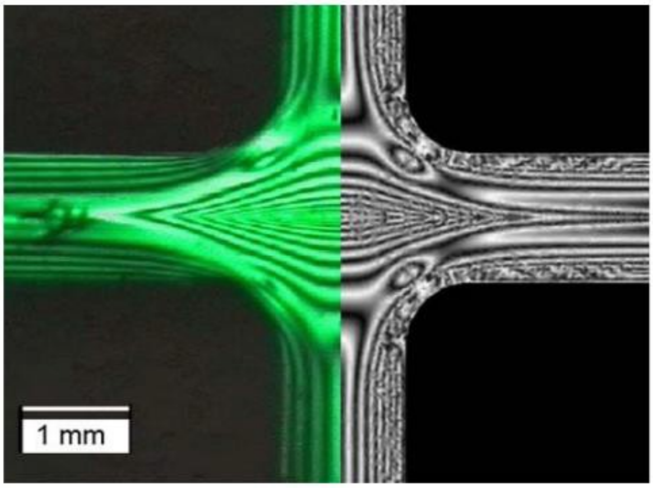

Fig. 8 – Comparison of experiment (left hand side) and simulation (right hand side) for Cross Slot geometry. Eight mode 2D, Pom Pom simulation (Mackley, 2010).

Starting from the Taylor's system of four roller apparatus, Bentley and Leal have developed in 1986 a computerised system by which a stagnation point can be maintained in the observation field a longer period of time. This thing was possible by implementing new technologies that enabled the fast correlation of the position in the field of observation with the parameters that influence the fluid flow, namely the rotation of rolls.

To control the position of the particle, in the visual field, the computer automatically adjusts the rotation speed of each motor apart due to the high rotation precision the stepper motors used. Actually, starting from the coordinates variation of a certain point taken by a video camera, the computer computes the frequency of the number of impulses needed to each one of the motor drivers. The aim of the experiment is to keep for a long period of time "the interesting particle" in the neutral central point of observation. This means that the parameters of flow must be modified by means of the speed rotation values of the rolls in a manner that do not abruptly modify the conditions of the experiment, in view of not loosing control on the position of the particle under observation. It is obvious that there is a certain imposed threshold value for the positioning error.

Automat controlling of the position in such installation involves video cameras and specialised sophisticated software systems that integrates image motion with motion control by motors using multiple channels, all of them with very high speed of calculation, and it can be rather expensive.

The execution of parts and the assembly, the positioning and operation of this type of equipment must be very precise to ensure horizontality, vibration insulation and other specific conditions, to obtain a fine balance during the experiment.

3. The four-roll mill for didactic laboratory

The equipment proposed is a simple variant of the Taylor apparatus but constructively adapted at the level of today technique evolution. It do not have the aim to ensure conditions of study obtainable at the level of 2020 but it can be a demonstrative material for students offering in the same time the possibility to develop new variants.

The designed four-roll mill is shown in Fig. 9. It is made by a cylindrical waterproof enclosure enhousing the stepper motors 2. Each roll is inserted by pressure on an axel coaxial with the motor shaft, outside of it. The four rolls are being precisely positioned. All the four rolls are controlled all together by means of drivers that commands the stepper motors.

Fig. 9 – Photograph of the four roll mill:
1 – control unit; 2- enclosure for stepper motors; 3- fluid cuvette; 4-support;
5 – video camera (Teodoriu, 2021).

The electronic part that commands the stepper motors are connected by means of a cable to a control unit 1.

The fluid tank 3 in which the fluid to be studied must be introduced is placed on a special support and has the bottom made by glass to enable lightening and filming by means of the video camera 5 connected to a computer.

Lightening is being ensured by a LED projector producing a parallel beam of light placed above the fluid level for the case the fluid is transparent enough. For the other cases it is used a direct light source placed under the bottom of the fluid tank inside the support 4.

The inside light source can operate in stroboscopic mode with adjustable frequency ensured by the control unit. This characteristic is useful for better seeing the flow, in a sequence of images of the marker particles, in a more suggestive manner.

The control unit contains the command modules of the stepper motors, their drivers, the frequency regulation unit of the stroboscopic LED projector, the main power source of the entire equipment, the potentiometers for rotation speed and for light pulse frequency regulation and also a LED display. The control unit contains also the on/off button, the fusible and the cooling system of the components. The both parts of the equipment are foreseen with an electrocution protection circuit.

The construction of the equipment allows the cuvette to be detached in such a way that it can be emptied and cleaned from one experiment to another.

The cuvette has a cylindrical shape and it is made by polished stainless steel to limit as much as possible the effects upon flowing in the interest zone, namely the space between rolls.

The stepper motors are positioned in a stainless steel sealed case to avoid the penetration of liquid inside of it. The shafts exit this compartment through double bearings made by graphite bronze between which are positioned felt seals. Each roll axel is coupled to the stepper motor shaft by a bolt coupling with a high degree of mobility to reduce vibrations and positioning or mounting errors.

The critical components in the precision of operation of the equipment were executed using CNC controlled machine tools.

3.1. The control possibilities

The command unit of the equipment contains the electronic part of it and by means of these components the following parameters can be adjust:

- the rotation speed of the motor – all motors can have the same speed and this can be regulated by means of a potentiometer;
- the frequency of the stroboscopic light – can be regulated by means of a potentiometer.

The display placed on the control unit shows values of the regulated parameters.

3.2. Mechanical system

Figures 10, 11 and 12 show the main parts of the mechanical system of the four-roll mill.

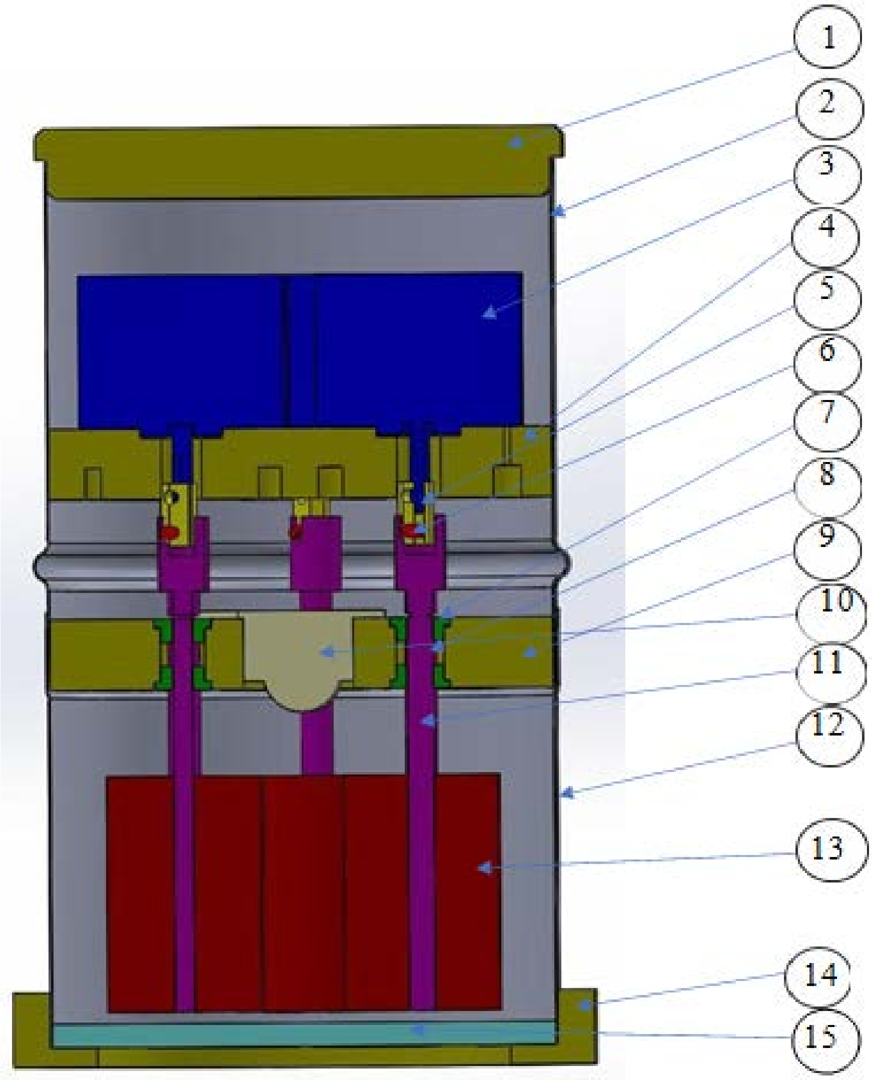

Fig. 10 – Representation of the four-roll mill: 1 – cover ; 2 – water proof enclosure; 3 – stepper motor; 4 – supporting plate; 5 – coupling; 6 – bolt; 7 – graphite bronze double bearings; 8 – felt sealing; 9 – intermediary plate; 10 – LED lamp; 11 – axel; 12 – cuvette; 13 – cylindrical roll; 14 – ring; 15 – round window glass.

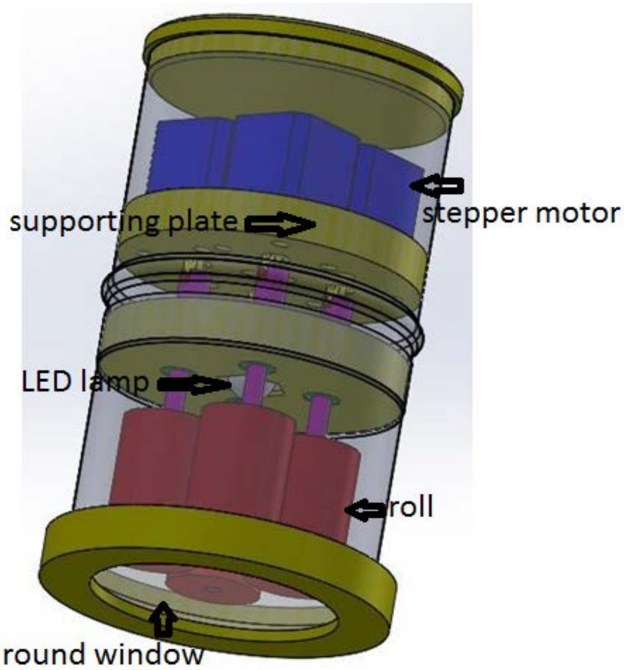

Fig. 11 – Axonometric view of the equipment.

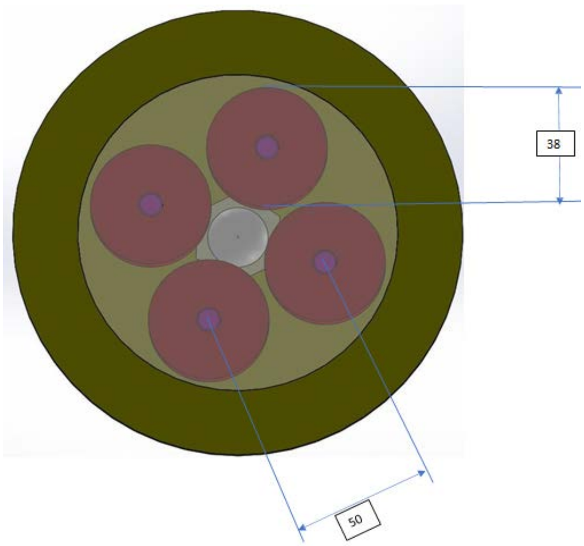

Fig. 12 – Detail for rolls positioning.

Figure 13 shows the stepper motor, NEMA 17 type, used in the equipment.

NEMA 17 is a hybrid stepping motor with a 1.8° step angle (200 steps/revolution). Each phase draws 1.2 A at 4 V, allowing for a holding torque of 3.2 kg-cm. NEMA 17 Stepper motor is generally used in Printers, CNC machines and Laser Cutters (https://components101.com/motors/nema17-stepper-motor).

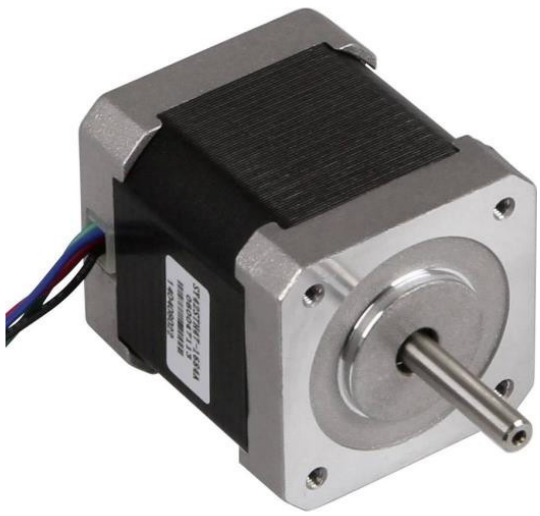

Fig. 13 – Stepper motor NEMA 17 (https://components101.com/motors/nema17-stepper-motor).

The motors are controlled by A4988 drivers using Arduino Uno microcontroller boards based on the ATmega328P chip, especially programed. (Teodoriu, 2021).

4. The operation of the equipment

The procedure for the equipment operation is rather simple. First, fill the cuvette with the fluid to be analysed to the mark inside the cuvette.

The upper body with the rollers attached on shafts is attached to the cuvette.

Connect the equipment to the power source by means of the socket.

Turn on the device by means of the button on the control unit. In this moment the LED display will show the initialization message.

After three seconds the rotors will start to rotate and the light source to emit light pulses. It is recommended that before starting to put the potentiometers in the position for minimum speed rotation.

Step by step one can increase the rotation speed value, value that is displayed on the screen of the control unit. Because stepper motors are being used the rotation speed remains constant as long as the potentiometer stays in a given position and the rotation speed can be adjust. The eventual variations by one unit of speed rotation own to the fact that the rotation speed is not an integer but is between the two values shown. By fine adjustment of the potentiometer the speed value can be stabilised.

The digital camera is introduced under the cuvette in the space destined for it and is connected to a computer with the proper software installed for obtaining images from the camera.

The flowing process can be seen on the screen of the computer and the frequency of the stroboscopic light and the speed rotation can be modified according to the experiment needs.

The computer has the possibility to record the experiment in a video format from which, images can be extracted or photographs taken.

After finishing the set of experiments the rotation speed is turn to the minimum and the apparatus is turned off. After stopping, the fan of the central unit will continue to operate during 5 seconds for evacuate the heat inside the case.

The upper part of the roll mill is detached, the used rolls are disassembled and the cleaning procedure can be done.

The fluid in the cuvette is collected properly and the cuvette must be cleaned too using suitable substances and materials to avoid corrosion or mechanical damages.

After complete drying, the equipment can be used again.

5. Conclusions

Without the pretensions of very sophisticated equipment, the designed and made four-roll mill can be used for didactic laboratory work to produce, control and visualize the flow phenomena.

Moreover, the use of a programmable interface offers the possibility of future adaptation and improvement of this equipment (Teodoriu, 2021).

REFERENCES

Bentley B.J., Leal L.G., *A computer-controlled four-roll mill for investigations of particle and drop dynamics in two-dimensional linear shear flows*, J. Fluid Mech., vol. 167, 219-240 (1986).

Berry M.V., Mackley M.R, *The six roll mill: unfolding an unstable persistently extensional flow*, Phil. Trans. Roy. Soc. London 287 (1337), 1-16 (1977).

Crowley D.G., Frank F.C., Mackley M.R., Stephenson R.G., *Localised flow birefringence of polyethylene oxide solutions in a four roll mill*, J. Polym. Sci. 14, 1111-1119 (1976).

Frank F.C., Mackley M.R., *Localized flow birefringence of polyethylene oxide solutions in a two roll mill*, J. Polym. Sci. A2 (14), 1121-1131 (1976).

Lagnado R.R., Leal L.G., *Visualization of three-dimensional flow in a four-roll mill*, Experiments in fluids, 9, 25-32 (1990).

Mackley M.R., *Stretching polymer chains*, Rheol Acta, 49, 443-458, Springer (2010).

Mackley M.R., Keller A., *Flow induced polymer chain extension and its relationship to fibrous crystallization*, Phil. Trans. Roy. Soc., London, A 278 (29), 4-79 (1975).

Scrivener O., Berner C., Cressely R., Hocquart R., Sellin R., Vlaches N.S., *Dynamical behaviour of drag-reducing polymer solutions*, J. Non-Newtonian Fluids Mech., 5, 475-495 (1979).

Taylor G.I., *The formation of emulsions in definable fields of flow*, Proc. Roy. Soc., London, A l46, 501–523, (1934)

Teodoriu A., *Proiectarea și realizarea unui laminor cu patru role*, Lucrare de disertație, Universitatea Tehnică "Gheorghe Asachi" din Iași, Facultatea de Știința și ingineria materialelor, Iași, 2021.

https://components101.com/motors/nema17-stepper-motor - consulted 01.02.2021.

CONSTRUCȚIA UNUI LAMINOR CU PATRU ROLE UTILIZAT ÎN STUDIUL CURGERII FLUIDELOR NE-NEWTONIENE (I). COMPONENTELE GENERALE ȘI SISTEMUL MECANIC

(Rezumat)

Având drept scop studiul preliminar al curgerii unor materiale diverse de tipul emulsiilor considerăm că nu este nevoie să fie utilizate echipamente de ultimă generație, foarte sofisticate și foarte scumpe în același timp. Mai mult, la nivel de laborator didactic, pentru a pune în evidență unele fenomene, este preferabil ca echipamentul utilizat să fie robust și fiabil și desigur, dacă este posibil, să permită înțelegerea principiilor constructive și a modului de operare a altor echipamente mai sofisticate. Prin această lucrare punem în evidență principiile constructive care au stat la baza unui echipament electromecanic simplu proiectat pentru studiul curgerii diferitelor fluide viscoase. Sunt arătate pe scurt istoricul unor echipamente având același scop și câteva detalii despre componentele propuse a fi utilizate în construcția unui laminor cu patru role pentru studiul curgerii. Această lucrarea prezintă componentele generale și partea mecanică a echipamentului care nu-și propune să aibă performanțele ce ar putea fi atinse în domeniu la nivelul anului 2022, dar este accesibil din punctul de vedere al prețului componentelor utilizate.

BULETINUL INSTITUTULUI POLITEHNIC DIN IAŞI
Publicat de
Universitatea Tehnică „Gheorghe Asachi” din Iaşi
Volumul 68 (72), Numărul 1-4, 2022
Secţia
ŞTIINŢA ŞI INGINERIA MATERIALELOR

THE CONSTRUCTION OF A FOUR-ROLL MILL USED IN THE STUDY OF NON-NEWTONIAN FLUID FLOWS (II). ELECTRONIC SYSTEM GENERAL COMPONENTS AND PROGRAMMING

BY

ADRIAN-PETRU TEODORIU, LEANDRU-GHEORGHE BUJOREANU and GHEORGHE BĂDĂRĂU*

“Gheorghe Asachi” Technical University of Iaşi,
Faculty of Materials Science and Engineering, Iaşi, Romania

Received: February 25, 2022
Accepted for publication: March 14, 2022

Abstract. The present paper aims to present the command unit of a didactic laboratory equipment destined for the study of non-Newtonian fluids flow phenomena, namely a four-roll mill built after the model conceived and used by G.I. Taylor, using technologies available in 2021. Without aiming to be a state-of-the art equipment, in what concerns the mechanical system and the automation command part the four-roll mill can produce the viscous fluid flow, can control it by variation of rotation speed of the four rolls and can film or photograph it in stroboscopic light, using a video camera plugged in an external computer. Besides the basic components of the command unit there are shown details specific to a mounting able to produce the adjustment and control of operation of the mechanical system made by four stepper motors, by means of Arduino Uno boards and A4899 drivers. The command system of the equipment can achieve simultaneously the actuation of the stroboscopic LED lamp and present on a display the current parameters adjusted. The paper presents also the programming of the Arduino Uno boards used in the command unit. The electronic elements used for the command unit were chosen having in mind the price accessibility and the market availability.

*Corresponding author; *e-mail*: gheorghe.badarau@tuiasi.ro

Keywords: didactic laboratory equipment, viscous fluids flow, mechanical components, stepper motor, bolt coupling, strobe light, video camera, rotation speed adjusting.

1. Introduction

In the case of making laboratory equipment for didactic purpose many times it is enough to be able to produce and demonstrate a given phenomenon using simple schemes, easier to understand by a student or a pupil (Teodoriu, 2021).

In the early stages of studying the non–Newtonian fluids flowing phenomenon it is enough to be able to produce and control it somehow roughly. For this it was designed and built a four-roll mill starting from the idea of “the four roller apparatus” used by G.I.Taylor during his study about the emulsion obtaining “in approximately definable fields of flow” (Taylor, 1934), namely for finding the mechanical steering conditions (Teodoriu, 2021).

2. Very short history

A.P. Teodoriu succeeded to design and produce an equipment from the family of the four-roll mill, proposed for the first time by the scientist G.I.Taylor in 1934, “in the Cavendish Laboratory through the kindness of Lord Rutherford, to whom the author wishes to express his thanks” (Taylor, 1934) and presented only the main components and the mechanical system of it in a previously presented paper (Teodoriu, 2021).

Fig. 1 – Photograph of the four roll mill: 1 – control unit; 2- enclosure for stepper motors; 3- fluid cuvette; 4-support; 5 – video camera (Teodoriu, 2021).

Such equipment was later used for studying the viscous fluids flow. An example is that used by B.J. Bentley and L.G. Leal from The Chemical Engineering Department, California Institute of Technology, Pasadena, U.S.A. who have developed in 1986 a computerised system by which a stagnation point inside a fluid flow can be maintained in the observation field a longer period of time. The schematic of that equipment is shown in Fig. 2.

This thing was possible by implementing new technologies that enabled the fast correlation of the position in the field of observation with the parameters that influence the fluid flow, namely the rotation of rolls (Teodoriu, 2021).

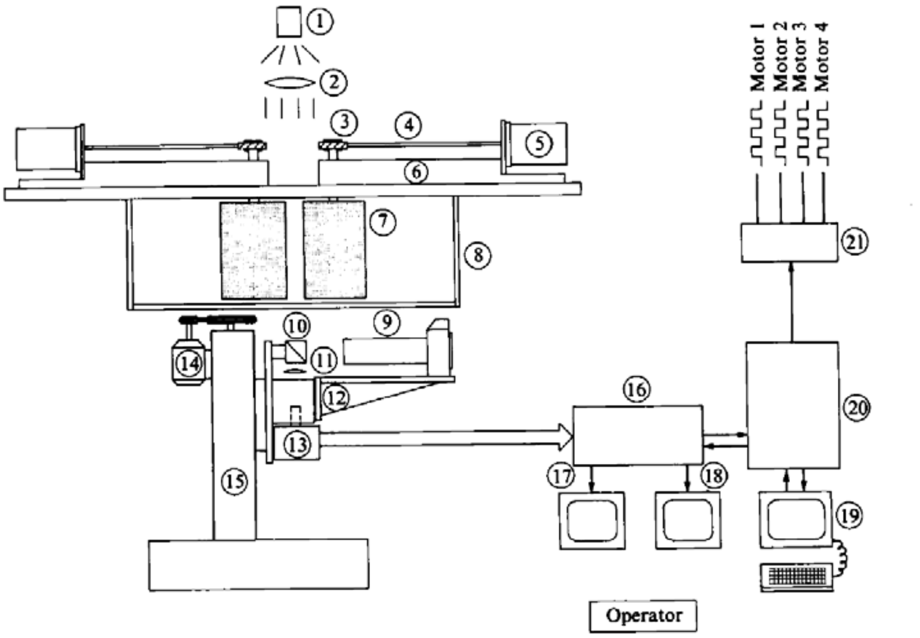

Fig. 2 – Side-view schematic of four-roll mill. (1) Point light source; (2) collimating lens; (3) worm gears; (4) drive shafts; (5) d.c. stepping motors; (6) roller mounting arms; (7) rollers; (8) glass tank; (9) still camera; (10) cubic beam splitter; (11) converging lens; (12) still-camera mount; (13) digital video camera; (14) motor for moving camera assembly vertically; (15) modified measuring microscope mount; (16) video pre-processor; (17) monitor for viewing unprocessed video; (18) monitor for viewing threshold video; (19) video terminal; (20) DEC minicomputer; (21) Apple microcomputer (Bentley, 1986).

Automat controlling of the position, in such installation involves video cameras and specialised sophisticated software systems that integrates image motion with motion control by motors using multiple channels, all of them with very high speed of calculation, and it can be rather expensive.

The execution of parts and the assembly, the positioning and operation of this type of equipment must be very precise to ensure horizontality, vibration insulation and other specific conditions, to obtain a fine balance during the experiment (Teodoriu, 2021).

3. Electronic and command hardware of the control unit of the four-roll mill for didactic laboratory

The control unit of the Teodoriu four-roll mill contains the command modules of the stepper motors, their drivers, the frequency regulation unit of a stroboscopic LED projector, the main power source of the entire equipment, the potentiometers for rotation speed and for light pulse frequency regulation and also a LED display. The control unit contains also the on/off button, the fusible and the cooling system of the components and it is foreseen with an electrocution protection circuit (Teodoriu, 2021).

For the control of the stepper motors rotation speed, of the stroboscope frequency and for displaying these operation values there were used three Arduino Uno boards, one i2C module for reducing the number of wires, two multi-turn potentiometers 10 kΩ, a LCD display and four A 4988 drivers for the four motors. Photographs of the A 4988 driver and Arduino Uno board are shown in Fig. 3.

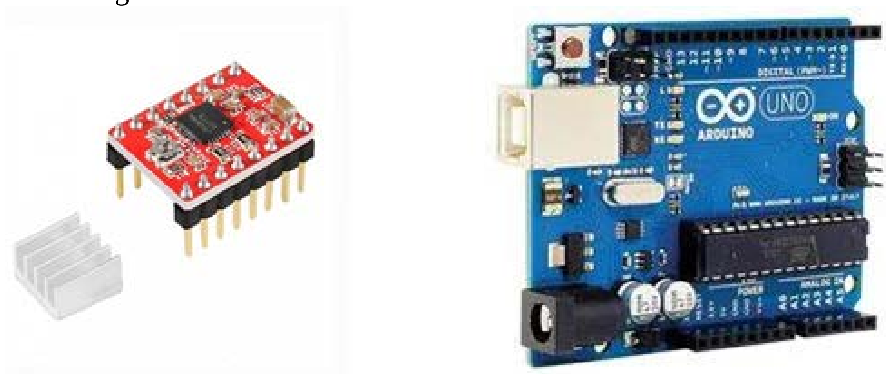

Fig. 3 – Photographs of the A 4988 driver and Arduino Uno board: left side – the A4988 driver and heat sink; right side - Arduino Uno board (Teodoriu, 2021).

Because of the precision available for the rotation speed control there were used for the four-roll mill stepper motors type NEMA 17.

NEMA 17 is a hybrid stepping motor with a 1.8° step angle (200 steps/revolution). Each phase draws 1.2 A at 4 V, allowing for a holding torque of 3.2 kg-cm. NEMA 17 Stepper motor is generally used in Printers, CNC machines and Laser Cutters. (https://components101.com/motors/ nema17-stepper-motor). NEMA 17 is shown in the photograph below, Fig. 4.

Fig. 4 Photograph of NEMA 17 stepper-motor
(https://components101.com/motors/ nema17-stepper-motor).

For the power supply of the equipment it was used a stabilised source of 19.5 V and 5A. For the stroboscopic lamp a 5V LED was chosen.

Because of the high value of the absorbed current needed by the motors the chips of the drivers can reach rather high temperatures and need to be cooled down to maximum 60°C. For doing this, besides the heat sinks of the drivers, it was used a cooler at 220 V, 50 Hz, the type used for cooling of the PC power sources.

The first Arduino Uno board called A1 with Atmega 328 p chip was used for ensuring enough calculation power for delivering an exact number of pulses to the motors, such ensuring a good control of the rotation speed. The rotation speed adjustment of the stepper motors need pulses ranging between 600 µs and 3400 µs (Teodoriu, 2021).

The exact values for the pulses computed by the chip depend also on the number of instructions programmed for a given Arduino board. A slowing down of the calculation speed of the Atmega 328p mounted on the Arduino Uno board can be produced, if more instructions are programmed on it, and this could cause finally to inacceptable interferences on the rotation speeds of the motors and this must be avoid during programming and testing.

A potentiometer called R2 having fine adjustment capabilities were used for delivering high precision values as inputs used by the board when determining the pulse duration and such to ensure a better control of the motors.

The 19.5 V stabilised power source is set to be activated at 8 seconds after pressing the on/off button placed on the command unit by means of a command relay placed on the third Arduino microcontroller board called A3 responsible for showing values about the equipment operation on the LCD display (Teodoriu, 2021).

3.1. The control of the motors

The control of the motors was achieved by means of a multi-turn potentiometer of 10 kΩ, R2, connected to the A0 pin (analogic input/output pin) of the Arduino microcontroller board A1 called MOTOARE in, Fig. 5.

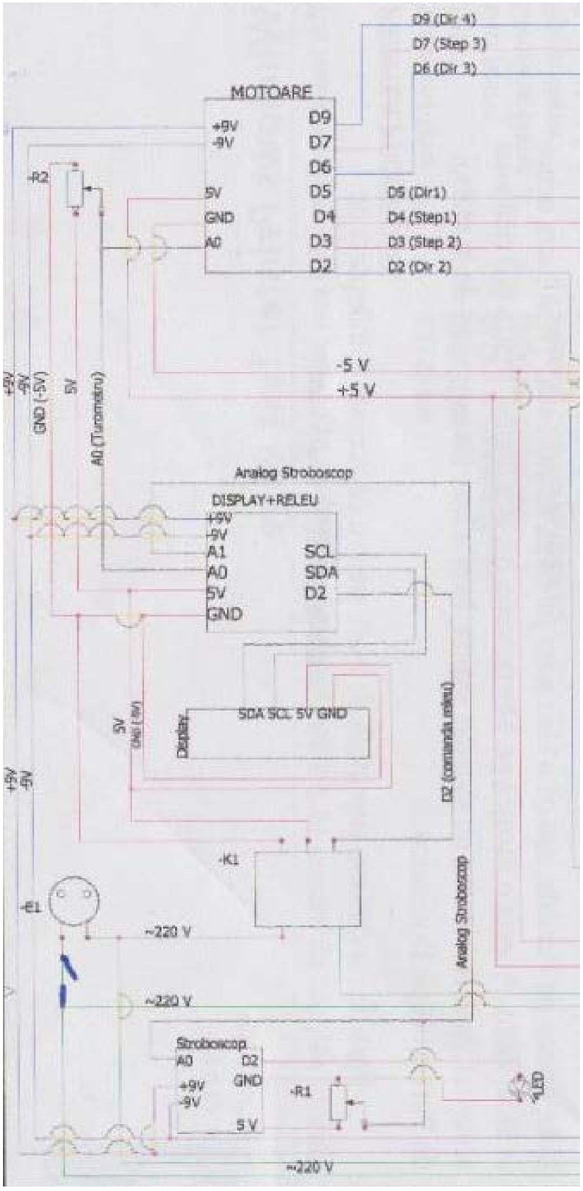

Fig. 5 – Part of the electronic scheme - rotation speed regulation and stroboscope blinking control (Teodoriu, 2021).

The potentiometer R2 was connected to the analogic pin A0. It can record, according to the voltage applied on it, values between 0 and 1023 fact that enable the use of it for controlling the motors speed (Teodoriu, 2021).

The four motors of the rollers are controlled by four circuits named drivers. They, as a function of the duration of the 5 V voltage pulse received from the Arduino board send toward the motors the same pulse duration but at 19.5 V voltage.

The duration of electric pulses is linked to the frequency of motor’s steps, in this manner being easy to compute the motor rotation speed. This frequency is given by the value read by the Arduino microcontroller board from the A0 pin that varies as a function of the variable resistance of the potentiometer R2, responsible for the motors rotation speed, Fig. 6.

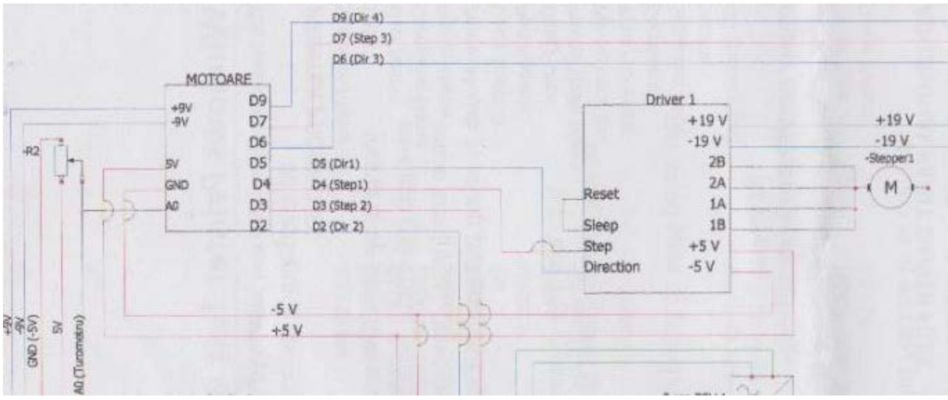

Fig. 6 – Part of the electronic scheme – command of the driver and stepper motor (Teodoriu, 2021).

When the motors have the minimum rotation speed 89 rpm the duration of an electric pulse is 3400 μs and at the maximum rotation speed 300 rpm the duration of a pulse is 600 μs.

These values can be modified, if needed, from the program run by the microcontroller board.

The construction of the electronic part is shown partially in Figs. 5 and 6:

- pins D2, D5, D6 and D9 (pins for digital input/output) of the Arduino board are connected to the direction of the motors drivers;

- pins D3, D4 and D7 (pins for digital input/output) of the board are connected to the step pins of the motors drivers.

D7 – is common for the motors 3 and 4 because the pin D8 from the microcontroller board can not give (by construction) enough current for controlling motor number 4 (not shown on the scheme). This is not a problem because the motors of the equipment are designed to produce the same rotation speed (Teodoriu, 2021).

If somebody would want to improve the equipment this could be a place to work on.

The power supply for the drivers A 4988 come from the Arduino board A1 at a voltage of 5V. The pins RESET and SLEEP of the drivers are being short circuited and so the driver circuit is permanently on, figure 6.

3.2. The program for controlling motors running on the Arduino Uno A1 microcontroller board

The program of the Arduino Uno A1 microcontroller board (MOTOARE) destined for motors controlling and the signification of instructions are given in Table 1.

Table 1

Program running on the Arduino Uno A1 (MOTOARE) microcontroller board (Teodoriu, 2021)

Instruction	Significance
#define dirPin 5 //dir rotor 1;	the digital pin 5 is attributed the value of pin for direction for driver 1
#define stepPin 4 //step rotor 1;	the digital pin 4 is attributed the value of pin for step for driver 1
#define dirPin2 2 //directie rotor 2;	the digital pin 2 is attributed the value of pin for direction for driver 2
#define stepPin2 3 //step rotor 2;	the digital pin 3 is attributed the value of pin for step for driver 2
#define stepPin3 7 //step rotor 3;	the digital pin 7 is attributed the value of pin for step for driver 3
#define dirPin3 6 //dir rotor 3;	the digital pin 6 is attributed the value of pin for direction for driver 3
#define stepPin4 10 //step rotor 4;	the digital pin 10 is attributed the value of pin for step for driver 4
#define dirPin4 9 //dir rotor 4;	the digital pin 9 is attributed the value of pin for direction for driver 4
#define stepsPerRevolution 200;	equalises the number of steps of the rotor corresponding to one revolution with 200
int potVal;	declares variable Val as integer
int valoare;	declares variable valoare as integer
int const potPin = A0;	communicates to the processor that the analogic pin A0, for reading the potentiometer, has a constant value during the program running
void setup() {	start of the structure setup that executes once the instructions inside it at the starting of the board
pinMode(stepPin, OUTPUT);	atributes the digital pin 1 as OUTPUT pins for controlling steps

Instruction	Significance
pinMode(dirPin, OUTPUT);	atributes the digital pin 1 as OUTPUT pins for controlling direction
pinMode(stepPin2, OUTPUT);	atributes the digital pin 2 as OUTPUT pins for controlling steps
pinMode(dirPin2, OUTPUT);	atributes the digital pin 2 as OUTPUT pins for controlling direction
pinMode(stepPin3, OUTPUT);	atributes the digital pin 2 as OUTPUT pins for controlling steps
pinMode(dirPin3, OUTPUT);	atributes the digital pin 3 as OUTPUT pins for controlling direction
pinMode(stepPin4, OUTPUT);	atributes the digital pin 2 as OUTPUT pins for controlling steps
pinMode(dirPin4, OUTPUT);	atributes the digital pin 4 as OUTPUT pins for controlling direction
}	end of the structure setup
void loop() {	start the repetitive structure loop – this structure repeats during the operation of Arduino microcontroller board
potVal = analogRead(potPin);	equalise the value of the variable potVal with that read from the analogic pin A0
valoare = map(potVal, 0, 1023, 500, 1700);	atributes the variable valoare the value of potVal and transforms the scale 0–1023 in 500-1700 correspondingly
digitalWrite(dirPin, LOW);	communicate to the board to not apply tension on the pin driver 2, thus establishing the rotation direction clock wise for the motor 2
digitalWrite(dirPin2, HIGH);	communicate to the board to apply 5V on the pin driver 1, thus establishing the rotation direction counter clock wise for the motor 1
digitalWrite(dirPin3, HIGH);	communicate to the board to apply 5V on the pin driver 4, thus establishing the rotation direction counter clock wise for the motor 4
digitalWrite(dirPin4, LOW);	communicate to the board to not apply tension on the pin driver 3, thus establishing the rotation direction clock wise for the motor 3
for (int i = 0; i < stepsPerRevolution; i++) {	start the repetitive structure for that controls the motors revolution speed
digitalWrite(stepPin, HIGH);	communicate to the board to apply 5V tension on the step pin 1 enhancing the rotation speed of motor 1
digitalWrite(stepPin2, HIGH);	communicate to the board to apply 5V tension on the step pin 2 enhancing the rotation speed of motor 2

Instruction	Significance
digitalWrite(stepPin3, HIGH);	communicate to the board to apply 5V tension on the step pin 3 enhancing the rotation speed of motor 3
digitalWrite(stepPin4, HIGH);	communicate to the board to apply 5V tension on the step pin 4 enhancing the rotation speed of motor 4
delayMicroseconds(valoare);	holds the program running for the duration valoare that can be modified by the potentiometer between 500 µs and 1700 µs
digitalWrite(stepPin, LOW);	communicate to the board to not apply tension on the step pin 1 diminishing the rotation speed of motor 1
digitalWrite(stepPin2, LOW);	communicate to the board to not apply tension on the step pin 2 diminishing the rotation speed of motor 2
digitalWrite(stepPin3, LOW);	communicate to the board to not apply tension on the step pin 3 diminishing the rotation speed of motor 3
digitalWrite(stepPin4, LOW);	communicate to the board to not apply tension on the step pin 4 diminishing the rotation speed of motor 4
delayMicroseconds(valoare);	holds the program running for the duration valoare that can be modified by the potentiometer between 500 µs and 1700 µs
}	marks the end of the repetitive structure for
}	marks the end of the repetitive structure loop

The positions of the motors programed above can be seen in Fig. 7.

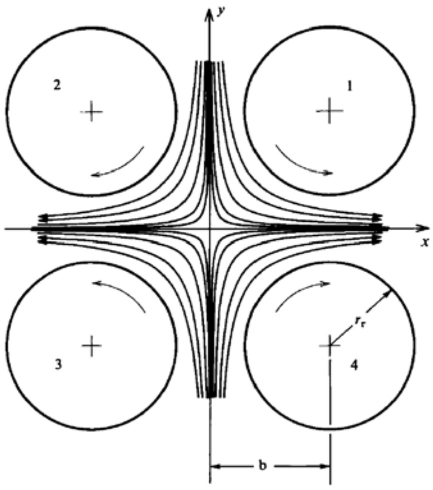

Fig. 7 – Motors positioning (Bentley, 1986).

3.3. The stroboscope control

For control the stroboscope we used another Arduino Uno microcontroller board called A2 dedicated only for it.

With a multi-turn potentiometer having fine adjustments capabilities, R1 shown in Fig. 5, of 10 KΩ, mounted on the case of the command unit, besides the one called R2 used for the regulation of motors speed, the pulse duration pulse can be adjusted and so the frequency of LED blinking can be enhanced or diminished (Teodoriu, 2021).

The LED does not request a separate power source. The needed 5V for operation can be obtained directly from the Arduino board A2 at which it is connected. The LED's anode (-) must be connected to pin GND (ground) of Arduino Uno microcontroller board. Pins 1 and 3 of the potentiometer are connected to the 5V pin of the board respectively at the GND and pin 2 of the potentiometer R1 is connected at the analogic INPUT A0 of the Arduino. Connecting pin 2 of the potentiometer at an analogic INPUT in Arduino was achieved because the digital pins can send toward the processor only two values: 0 if the voltage applied is 0 V or 1 if the voltage applied is 5V. The analogic pins can send as a function of the input voltage values between 0 and 1023 and this make possible the use of the potentiometer for the blinking frequency control of the stroboscope (Teodoriu, 2021).

3.4. The program for stroboscope control running od the Arduino Uno A2 microcontroller board

The program of the Arduino microcontroller board A2 destined for stroboscope controlling and the signification of instructions are given in Table 2.

Table 2
Program running on the Arduino Uno A2 microcontroller board for frequency blinking control (Teodoriu, 2021)

Instruction	Significance
int potPin = A0;	communicates to the processor the fact that the analogic reading pin of the blinking frequency adjustment potentiometer will be A0 for all the duration of program running
int potVal;	declare variable Val as integer
int frecventa;	declare variable frecventa as integer
void setup() {	start of the structure setup that executes once the instructions inside it at the starting of the board
pinMode(2, OUTPUT);	atributes the digital pin 2 as OUTPUT pins for controlling frequency

Instruction	Significance
}	end of the structure setup
void loop() {	start the repetitive structure loop – this structure repeats during the operation of Arduino microcontroller board
potVal = analogRead(potPin);	equalise the value of the variable potVal with that read from the analogic pin A0, value determined by the position of the fine tuning potentiometer position for setting the frequency of stroboscope blinking
int citire = map(potVal, 0, 1023, 0, 150);	declare variable citire and attribute to it the value potVal and also transforms the scale 0-1023 of possible values in 1-150 correspondingly
digitalWrite(2, HIGH);	sends the voltage 5V on the digital pin 2 thus lighting the LED
delay(citire);	stops the execution of the program – the time of delay is given by the value of the variable citire
digitalWrite(2, LOW);	sends the voltage 0V on the digital pin 2 thus light off the LED
delay(citire);	stops the execution of the program – the time of delay is given by the value of the variable citire
}	end of repetitive structure loop

3.5. Displaying information on the LCD screen

We have used another Arduino Uno controller board to display the rotation speed of the motors and the stroboscope blinking frequency on a LCD screen. We have attached an I2C module to the LCD display to reduce the number of wires from 16 to 4.

We have connected the potentiometers for rotation speed adjustment and that for controlling the stroboscope at pins A0 and A1 of the Arduino Uno microcontroller board. We used analogic pins because the digital pins read only two values as a function of the applied voltage on them by comparison with the analogic ones which have a larger scale of recordable values between 0 and 1023.

So the potentiometer for motors rotation speed is connected to both Arduino boards A1 – (MOTOARE) and to the third board A 3 – (Display) destined for displaying the operation values and the value read by the pin A0 on the A1 board (MOTOARE) is the same with that of A0 from the A3 board (Display) because the voltages applied on the pins are the same, the wires being connected at the same potentiometer R2. Also the pin A1 on the board A3 (Display) receives a value equal with that received by the A0 from the A2 board responsible with the stroboscope frequency control, because both pins are connected to the same potentiometer R1 that controls the stroboscope frequency (Teodoriu, 2021).

We have connected both potentiometers at the board A3 (Display) to be able to show the exact values corresponding to motor rotation speed and of the stroboscope frequency as a function of the voltages applied on the analogic pins. The values displayed obtained in this manner are very precise; a sensor can not reach a greater precision (Teodoriu, 2021).

The relay that closes the circuit of the power supply of 19.5V for motors is connected at the digital pin D2 of A1 and closes at a precise programmed time after pushing the on/off button. This is foreseen to let enough time to start for the other two Arduino Uno boards, protecting them and the drivers of the stepper motors.

3.6. The program for displaying information on the LCD screen running on the Arduino Uno A3 microcontroller board

The program of the Arduino Uno A3 microcontroller board destined for stroboscope control and the signification of instructions are given in Table 3.

Table 3
Program running on the Arduino Uno A3 (DISPLAY) board (Teodoriu, 2021)

Instruction	Significance
#include <LiquidCrystal_I2C.h>	set of instructions that simplify the use of the display
LiquidCrystal_I2C lcd(0x27, 20, 4);	communicates to the processor the address and the characteristics of the display
int potVal;	declares variable Val as integer
int const stroboscop = A1;	declare the named constant stroboscop as integer and atributes the value A1 from the analogic pin 1, the same of the potentiometer R1
int valoare;	declares variable valoare as integer
int frecventa;	declares variable frecventa as integer
int strobo;	declares variable strobo as integer
int valoare2;	declares variable valoare2 as integer
int const potPin = A0;	declare the named constant potPin as integer and atributes the value A0 from the analogic pin 0
int RPM;	declares variable RPM as integer
int releu = 2;	declares variable releu as integer and associate it with the digital pin 2
void setup() {	start of the structure setup that executes once the instructions inside it at the starting of the board

Instruction	Significance
pinMode(releu, OUTPUT);	atributes the digital pin 2 associated with variable releu as OUTPUT pin
lcd.init();	Initialise the communication of the board with the LCD screen
lcd.clear();	deletes the screen ensuring no displaying
lcd.backlight();	ensure lighting of the LCD display
lcd.setCursor(0,0);	sets the coordinates of the point where the first sign will be displayed on screen in this case (row 0, column 0)
lcd.print("LAMINOR CU 4 ROLE");	displays the text “LAMINOR CU 4 ROLE”
lcd.setCursor(0,2);	sets the coordinates of the point where the first sign will be displayed on screen in this case (row 0, column 2)
lcd.print("Initializare sistem");	displays the text “Initializare sistem”
delay(5000);	stops the running of the program for 5000 ms (5 seconds)
digitalWrite(releu, HIGH);	activates the digital pin releu – starting the fan and the 19.5 V power source
}	end of the structure setup
void loop() {	start the repetitive structure loop – this structure repeats during the operation of Arduino microcontroller board
potVal = analogRead(potPin);	atributes the variable potVal the value read on the analogue pin of the potentiometer R2 for rotation speed control
strobo = analogRead(stroboscop);	atributes the variable strobo the value of the constant stroboscop at which is connected the analogic pin of the potentiometer R1 that regulates the blinking frequency of the LED
valoare = map(potVal, 0, 1023, 500, 1700);	atributes the variable valoare the value of potVal and transforms the scale 0–1023 in 500-1700 correspondingly for potentiometer R2 that regulates the rotation speed
valoare2 = map(strobo, 0, 1023, 0, 150);	atributes the variable valoare2 the value of strobo and transforms the scale 0–1023 in 0-150 correspondingly
RPM = round(150000/valoare);	atributes to variable RPM the round value resulted from the calculus 150000/valoare
frecventa = (valoare2);	atributes variable frecventa the value of valoare 2
lcd.clear();	the screen does not display anything when the instruction is executed
lcd. print("Turometru rotoare");	displays on screen the text “Turometru rotoare”
lcd.setCursor(0,1);	sets the coordinates of the point where the first sign will be displayed on screen in

Instruction	Significance
	this case (row 0, column 1)
lcd.print(RPM);	displays on screen the value of variable RPM
lcd.setCursor(3,1);	sets the coordinates of the point where the first sign will be displayed on screen in this case (row 3, column 1)
lcd.print(" RPM")	displays on screen the text “RPM”
lcd.setCursor(0,2);	sets the coordinates of the point where the first sign will be displayed on screen in this case (row 0, column 2)
lcd.print("Stroboscop");	displays on screen the text “Stroboscop”
lcd.setCursor(12,2);	sets the coordinates of the point where the first sign will be displayed on screen in this case (row 12, column 2)
lcd.print("(Puls/2)");	displays on screen the text “Puls/2”
lcd.setCursor(0,3);	sets the coordinates of the point where the first sign will be displayed on screen in this case (row 0, column 3)
lcd.print(frecventa);	displays on screen the value of variable frecventa
lcd.setCursor(3, 3);	sets the coordinates of the point where the first sign will be displayed on screen in this case (row 3, column 3)
lcd. print(" ms");	displays on screen the text “ms”
if(frecventa == 0){	starts the IF construction verifying the relation expression frecventa = 0; if true the two following two instructions are executed
lcd.setCursor(8, 3);	sets the coordinates of the point where the first sign will be displayed on screen in this case (row 8, column 3)
lcd.print("(continuu)");	displays on screen the text “continuum”
}	end the IF construction
delay(250);	stops the running of the program for 250 ms (5 seconds)
}	end the repetitive construction loop

4. Conclusions

Without the pretensions of very sophisticated equipment, the electronic equipment of the designed and made four-roll mill can be used for didactic laboratory work to produce, control and visualize the flow phenomena.

By using a programmable interface the possibility of studying the microcontroller board programming principles and understand it is ensured.

Improvements of this equipment or/and of the programme can be at hand for many students and such one can extend its use in the field of mechanics or automated control.

REFERENCES

Bentley B.J., Leal L.G., *A computer-controlled four-roll mill for investigations of particle and drop dynamics in two-dimensional linear shear flows,* J. Fluid Mech., vol. 167, 219-240 (1986).

Mackley M.R., *Stretching polymer chains*, Rheol Acta, 49, 443-458, Springer (2010).

Taylor G.I., *The formation of emulsions in definable fields of flow,* Proc. Roy. Soc., London, A l46, 501–523 (1934).

Teodoriu A., *Proiectarea și realizarea unui laminor cu patru role*, Lucrare de disertație, Universitatea Tehnică "Gheorghe Asachi" din Iași, Facultatea de Știința și Ingineria Materialelor, Iași, 2021.

https://components101.com/motors/nema17-stepper-motor - consulted 01.02.2021.

CONSTRUCȚIA UNUI LAMINOR CU PATRU ROLE UTILIZAT ÎN STUDIUL CURGERII FLUIDELOR NE-NEWTONIENE (II). COMPONENTELE GENERALE ALE PĂRȚII ELECTRONICE ȘI PROGRAMAREA ACESTEIA

(Rezumat)

Lucrarea de față își propune să prezinte unitatea de comandă a unui echipament didactic de laborator destinat studiului fenomenelor de curgere a fluidelor non-newtoniene, și anume un laminor cu patru role construit după modelul conceput și utilizat de G.I. Taylor, folosind tehnologiile disponibile în anul 2021. Fără a avea pretenția unui echipament de ultimă generație, în ceea ce privește sistemul mecanic și partea de comandă a automatizării, laminorul cu patru role poate produce curgerea unui fluid vâscos, o poate controla prin variația vitezei de rotație a celor patru role și o poate filma sau fotografia în lumină stroboscopică, folosind o cameră video conectată la un computer extern. Pe lângă componentele de bază ale unității de comandă sunt prezentate detalii specifice unui montaj capabil să producă reglarea și controlul functionării sistemului mecanic realizat prin patru motoare pas cu pas, prin intermediul unor microcontrolere tip Arduino Uno și driverelor A4899. Sistemul de comandă al echipamentului poate realiza concomitent acționarea lămpii LED stroboscopice și prezenta pe un ecran parametrii de reglaj curenți. Lucrarea prezintă în detaliu programarea plăcilor Arduino Uno utilizate în unitatea de comandă. Elementele electronice utilizate pentru unitatea de comandă au fost alese având în vedere accesibilitatea prețului și disponibilitatea pe piață.

BULETINUL INSTITUTULUI POLITEHNIC DIN IAŞI
Publicat de
Universitatea Tehnică „Gheorghe Asachi” din Iaşi
Volumul 68 (72), Numărul 1-4, 2022
Secţia
ŞTIINŢA ŞI INGINERIA MATERIALELOR

EXPERIMENTAL STUDY OF FLOW PHENOMENA USING A FOUR-ROLL MILL

BY

RODICA TEODORIU[1], LEANDRU-GHEORGHE BUJOREANU[1], ANDREI CUCOŞ[2] and GHEORGHE BĂDĂRĂU[1,*]

[1]"Gheorghe Asachi" Technical University of Iași,
Faculty of Materials Science and Engineering, Iași, Romania
[2]"Gheorghe Asachi" Technical University of Iași,
Faculty of Mechanics, Iași, Romania

Received: June 27, 2022
Accepted for publication: July 24, 2022

Abstract. This paper aims to analyse the flowing phenomena using an experimental didactic equipment, namely a four-roll mill from the Faculty of Materials Science and Engineering from the Technical University "Gheorghe Asachi" from Iași.

Studying the fluid flow patterns by visualisation is a method which provides a intuitive understanding of processes (Lagnado and Leal, 1990). During the tentative of mixing of two fluids in order to obtain emulsions (Taylor, 1934) or stretching polymer chains in fluid state (Mackely and Keller, 1975) is efficient to directly link the parameters of equipment and the result obtained, and this can be done sometimes by visualisation.

For studying a Newtonian fluid flow in a four – roll mill it was used the method of visualizing the fluid. The observations made on the effect of enhancing the rollers rotation speed upon the evolution of the constant three dimensional flow between rollers are reported. The experiments of flow visualisation were made in sets, investigating a certain composition of a fluid, looking for the aspect of flow pattern versus the rotation velocity imposed. The rollers were made to rotate in such a manner that generates an approximate

*Corresponding author; *e-mail*: gheorghe.badarau@tuiasi.ro

bidimensional linear flow near the centre of the apparatus at low speeds. Observations shown stable vortexes, symmetric positioned growing near the superior and inferior walls of the fluid tank, as the Reynolds number grows up to a critical value.

A supplementary growing in the Reynolds number beyond a critical value results in loosing of the symmetric aspect of flow. The experiments also certified the capability of the experimental equipment to provide video data about viscous fluids flow.

Keywords: didactic laboratory equipment, viscous fluid flow, visualization of fluid patterns, stroboscopic light, video camera, rotation velocity adjusting

1. Introduction

The four–roll mill was proposed by Taylor (Taylor, 1934) for the experimental study of the deformation and tearing of a drop of fluid suspended into a second fluid subject to an extensional flow. This device is made by four cylindrical rolls that rotate inside a container filled with fluid. The axes of the cylinders are parallel and symmetrically disposed in the corners of a square. Taylor invented this device aiming to generate a bidimensional approximately homogenous extensional flow in the central region between rolls. However the device was later considered as more valuable for experimental purposes because it is capable to simulate a wide range of homogenous bidimensional fluxes, the pure extensional one being just one of these.

In the majority of experimental studies it is necessary to obtain well defined cinematic conditions for a correct interpretation of measurements. One can make the hypothesis that a bidimensional flux is predominant in the region between rolls, at least, inside the most of it.

However the three dimensional effects of the fluxes are inevitable because the finite length of rolls and of the presence of upper and lower walls of the container and not least because of the eccentric movement of rolls. Some of the effects mentioned can be avoided but not in the visual measurements that need transparent solid walls.

The evolution of secondary three dimensional fluxes and the occurrence of instabilities according Fuller and Leal are frequently reported as factors that diminish the range of experimental applications of the four-roll mill (Bentley and Leal, 1986).

This paper aims to contribute at the understanding of these effects by means of some simple experiments of flux visualisation.

Giesekus had demonstrated for the first time that good approximations of bidimensional homogenous fluxes can be obtained at least in a small region between the roll of a four-roll mill. These fluxes are obtained when each of the rolls of a diagonal pair (namely the pair made by the rolls 1 and 3 or the pair made by the rolls 2 and 4 from Fig. 1) rotate in the same direction with the same angular velocity (Bentley and Leal, 1986).

Figure 1 shows a top view of the four–roll mill. The rolls positioning and their rotation direction and velocity are very important to obtain a bidimensional flow of the fluid inside the container.

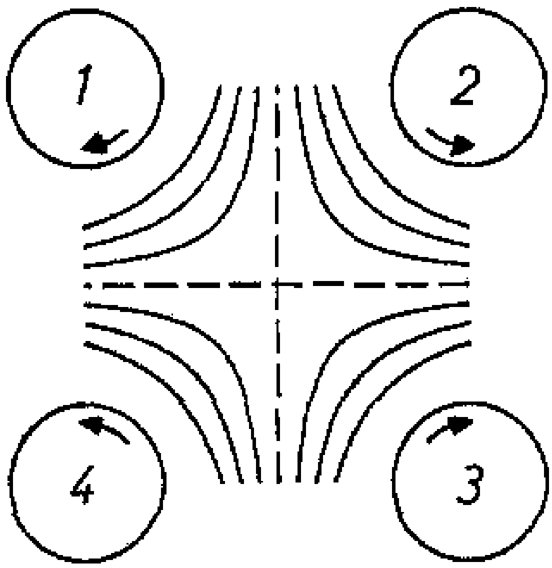

Fig. 1 – Cross section of the rolls, the rotation direction and flux lines in a viscous fluid placed in a four-roll mill (Bentley and Leal, 1986).

A quantitative research of the flux lines obtained using the four-roll mill was achieved by Fuller *et al*. in 1980. The measurements have shown the homogeneity of the fluid flow in a small region around the central stagnation point. The dimensional scale of this region is approximately equal with the size of the distance between rolls.

2. Equipment

2.1. Equipment description

It was used a didactic four-roll mill designed and manufactured by the master student Adrian Teodoriu in 2021 from the Faculty of Materials Science and Engineering, from the Tehnical University "Gheorghe Asachi" from Iași.

The equipment was described in detail in a previous article by Teodoriu *et al*. and a principle scheme showing the sizes and the rotation directions of the rollers is given in Fig. 2.

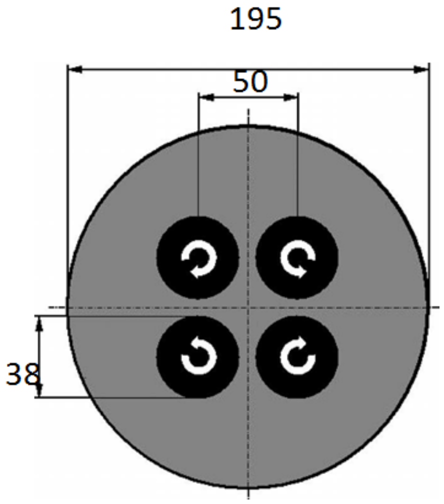

Fig. 2 – Principle scheme of the four-roll mill: sizes and rotation directions of the rolls (Teodoriu A., 2021; Teodoriu R., 2021).

The four rollers are suspended inside a cylindrical tank with the diameter 195 mm and height 85 mm made by stainless steel with the bottom made by transparent glass to enable visualization. The cylindrical rollers having 38 mm in diameter and 50 mm length are made of felt as shown in Fig. 3. They are mounted on stainless steel axels enabling a gap of about 1 mm facing the bottom of the fluid tank and 10 mm space to the fluid tank lateral cylindrical wall.

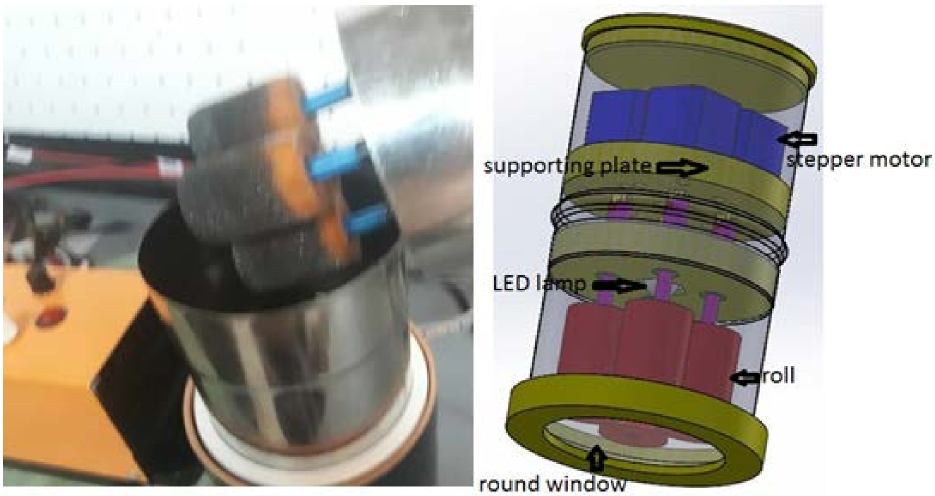

Fig. 3 – Four-roll mill - photograph of the rollers and axonometric view of the four-roll mill (Teodoriu A., 2021).

The rollers axels are parallel and their centres of symmetry are positioned in the corners of a square with a side 47 mm. The dimension of the free space between rollers is 12 mm and the ratio between the roller diameter and this value is 3.16. This particular value of the ratio was chosen by the designer taking into account the experience of Taylor and Bentley (Bentley, 1986).

The rollers are independently driven using stepper motors, fact that ensure an important capability of the equipment, namely the fine adjustment of rotation velocity. The stepper motors positioning can be seen in figure 3 right side. The range of rotation velocity can be adjusted in the range 85-200 rot/min by means of an electronic controller board.

2.1.1. Lighting and photography

The lighting of the flowing field is very important for the visualization experiments. A strong contrast is necessary between the drop and background.

The central position of the flowing field was illuminated by a beam of light from a LED light source with a parallel beam. Its position can be seen in Fig. 3 – right side. Also it was used the capability of the equipment to produce light in stroboscopic pulses.

The ray of light passes through the field of flow and reaches the camera sensor. After recording, the image was processed using video editing software, to increase the contrast and improve the observations.

2.1.2. The control of four-roll mill

In order to succeed in the experiments of liquid drop deforming it is necessary to keep the drop as close as possible in the central stagnation point.

The stagnation point is the same with the centre of the device and can be considered as origin point when the fluid flow is in the equilibrium state.

To keep the drop as close as possible in the central stagnation point can be done only by changing the fluid flow by adjusting the rollers rotation velocity. These changes must be done slowly in small steps to avoid significant perturbation of the fluid flow studied, for example the sharing rate during flow.

When the drop deviates from the centre of the device the modifications of the flowing field must be made in such a manner that the drop to be brought back to the centre, in the stagnation point. For example, if the drop goes right the pair of rollers from the left side accelerates and the pair from the right side slows down accordingly. This has as a consequence the imposing of a displacement from right to left of the flowing field. It is obvious that for making the drop to go back to the centre it has to be placed in a position inside the new flow flux where the net speed is towards the origin, fact that is equivalent with that the stagnation point is farther from the centre by comparing to the drop mass centre.

This kind of action can be taken for all turbionary fluxes except one, the case when the drop moves on along the exit flow line. For correcting this is necessary to adjust the speeds of all four rollers in the same time and a complex computer controlled device is necessary. Such an equipment was designed and built and used by Bentley and Leal from California Institute of Technology, Pasadena, USA, in 1985 (Bentley, 1986).

Our case is a less complex equipment at which the possibilities of control are limited to rotation speed adjustment, manually and concomitant for all the four rollers. This is why such equipment can offer only punctual information, as photographic snapshots of the fluid flow phenomena.

3. Experiment

The experiments were done using the mill as follows:

- the rollers rotate with identical velocities;

- the rollers forming a diagonal pair rotate clock wise and the rollers forming the other pair rotate in the opposite direction.

This setting ensures the conditions for laminar flow at low speeds and the resulted ideal pattern is shown in Fig. 1.

The Reynolds number can be varied by adjusting the rotation velocity of the rollers.

There were used three types of fluids:

1. Emulsion 30% silicon oil in distilled water;
2. Emulsion made from emulsion 30% silicone oil in distilled water + 15% quartz powder and distilled water;
3. Silicone oil 98% + distilled water (without forming an emulsion).

The emulsions were prepared by strong mechanical mixing followed by a treatment in a bath with ultrasounds at 40000 Hz during 30 minutes.

Figure 4 shows a photograph of the emulsion making process.

Fig. 4 – Photograph of the emulsion making process (Teodoriu A., 2021).

The third mixture made from silicone oil and distilled water (without forming an emulsion) has been used to obtain information about the macroscopic drop behaviour.

In all the cases it was used a trace marker for putting into evidence the flowing pattern.

The temperature was kept constant at a value of 20°C.

There were used direct and/or transparency lighting conditions depending upon the opacity of the fluid under observation.

The experiment was done in the conditions illustrated in Fig. 1, using the same rotation velocity for the rollers and the sense indicated. The speed can be varied simultaneous for the four rollers. These facts lead to the strong instability of the particle position by comparing to the central zone. To obtain photographs with the particle in the origin it was necessary to select from the film certain images.

A droplet having about 2 mm in diameter was introduced inside the device. After this it was adjusted the value for the lighting threshold to ensure the conditions for observation. There were used a series of coloured filters for light: red, yellow, blue or combinations of them for obtaining enough contrast. The video camera was constantly focussed on the same spot for the entire duration of the experiment. The position of the droplet was determined using the filmed material.

The motors have been started at the lower speed, 89 [rpm] and then the rotation velocity was increased using a multi-turn potentiometer and shown on the display.

The chain of events in a typical use was: starting the rollers at a minimum sharing rate; waiting a period of time to enable the droplet to came closer to a stable shape – this time varies as a function of the droplet viscosity, taking values ranging from less of 1 second for the less viscous liquids to 1 minute for those having high viscosities.

During the step by step enhancing of the rotation velocity the droplet passes through various relatively stable shapes with more and more deformations. For the majority of the ratios between the type of flow and viscosity it was reached a rate of sharing were the forces of surface tensions were not able to equilibrate the viscosity loads and so, it was not possible to obtain a stable shape for the droplet. These points were defined as points of dispersion of the droplet in the experiments conducted.

In the cases in which the dispersion of the droplet was achieved, the flowing continued at the critical sharing rate for a variable duration in time after it was obvious the fact that no droplet was able to maintain the stable shape. The droplets became more and more deformed but did not decompose further in fragments during flowing. Some extended droplets fragmented into a number of droplets by a complicated motion controlled by the superficial tension, others coming back to the initial spherical shape. The type of behaviour depended on the degree of extension obtained before the flowing stopped and on the viscosity ratio.

Photographs taken on the droplets during deforming and in dispersed state for various experiments are given in Fig. 5.

4. Results

The experimental results are presented in sequences of photographs that show the evolution of the flowing lines between rollers during an increasing of the Reynolds number.

For understanding the photographs, the diagram in Fig. 2 have to be considered. There are three planes of orthogonal symmetry that intersect in the centre of the device. One plane of symmetry is the horizontal plane placed in the middle of the rollers. The other two are vertical planes. The rollers 1 and 3 rotate in the clock wise direction and the rollers 2 and 4 in the counter clock wise direction. The fluid enters in the region between rollers 1 and 2 and rollers 3 and 4 and exits from this region through the space between the rollers 1 and 4 and the space between rollers 2 and 3. One vertical plane can be considered referring to the entrance spaces and the other can be defined referring to the exit spaces between rollers.

The set of photographs in Fig. 5 shows modifications during the enhancing of rotation velocity in the thin region containing the horizontal base plane for a ration aspect 3.16.

Parts of the rollers can be seen in the corners of the photographs. The rollers positioned in the uppers left side and lower right side rotate clock wise and the other pair in the opposite direction. The fluid will enter from above and below and will exit through the spaces placed on the right hand and on the left hand.

Going up to an approximate rotation velocity of 180 [rot/min] the flow in the medium horizontal plane can be defined as an extensional and pure bidimensional one, near the stagnation point between rollers. The occurrence of a vertical component of the speed on the medium horizontal plane takes place when the rotation velocity overcomes 230 [rot/min]. It can be observed that at higher velocities turbulences occurred disturb the flow in the central zone. However the flowing field near the rollers surfaces and along the axels of entrance appears essentially unchanged for the range of rotation velocities 120 – 280 [rot/min].

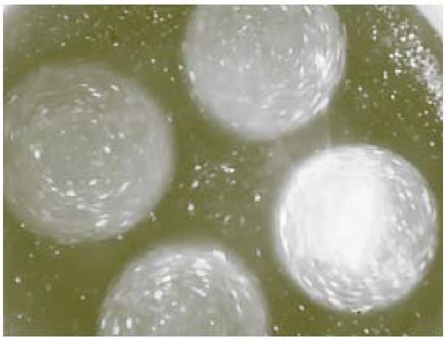

120 rpm

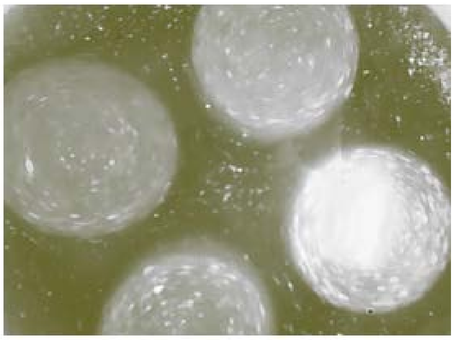

140 rpm

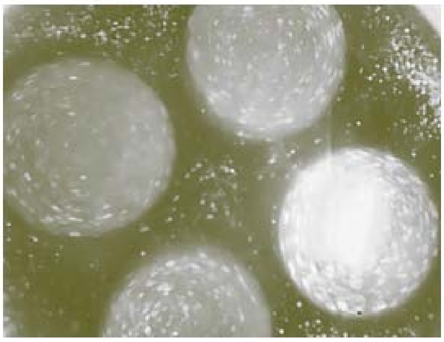

160 rpm

180 rpm

Fig. 5a – Set 1 – Photographs obtained for: Emulsion 30% silicone oil in distilled water (obtained in ultrasonic bath) at 120; 140; 160 and 180 [rot/min] (Teodoriu R., 2021).

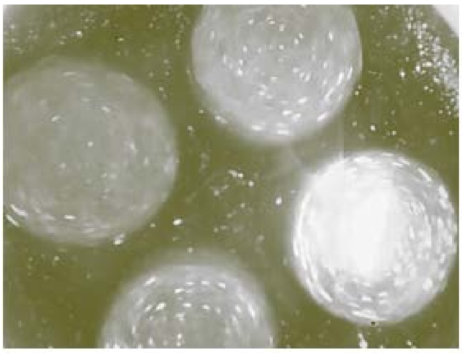

200 rpm

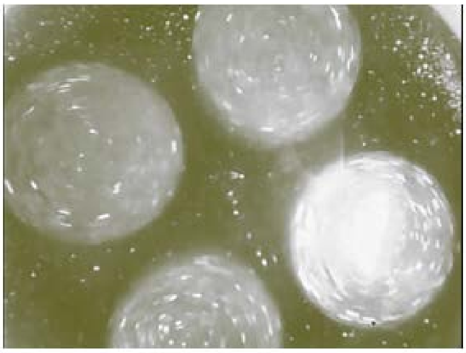

240 rpm

Fig. 5b – Set 1 **–** Photographs obtained for: Emulsion 30% silicone oil in distilled water (obtained in ultrasonic bath) at 200; and 240 [rot/min] (Teodoriu R., 2021).

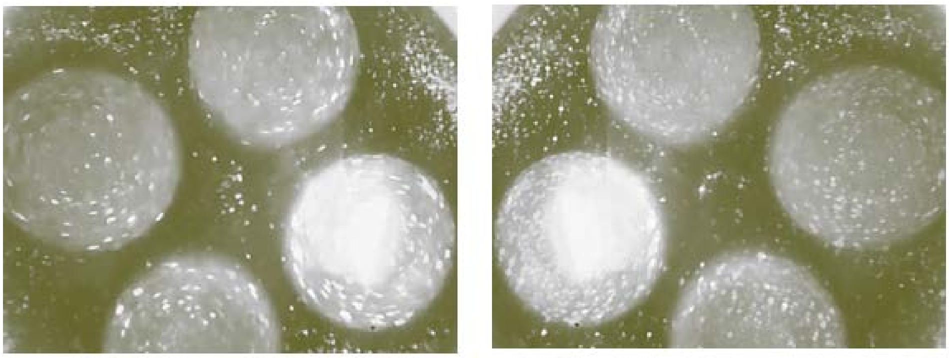

260 rpm 280 rpm

Fig. 5b – Set 1 – Photographs obtained for: Emulsion 30% silicone oil in distilled water (obtained in ultrasonic bath) at 260 and 280 [rot/min] (Teodoriu R., 2021).

120 rpm

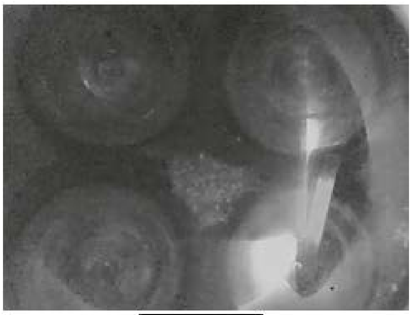

160 rpm

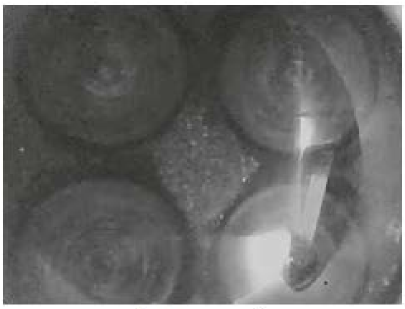

200 rpm

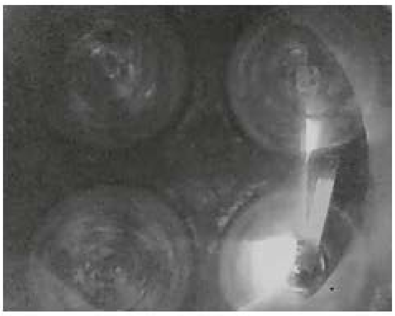

240 rpm

Fig. 5c – Set 2 – Photographs obtained for: Emulsion 30% silicone oil in distilled water; 15% quartz powder and distilled water at 120; 160; 200 and 240 [rot/min] (Teodoriu R., 2021).

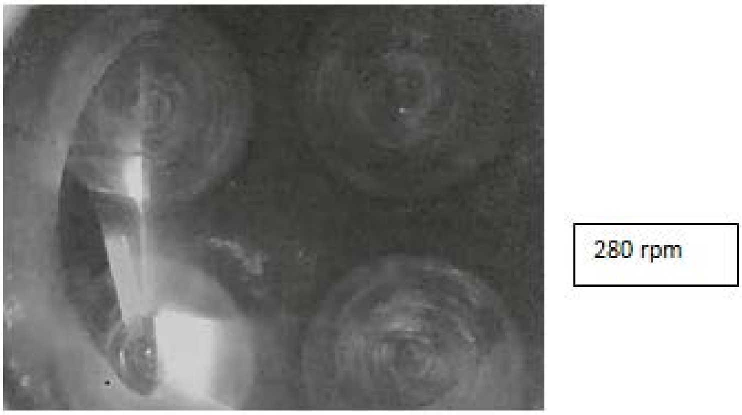

Fig. 5d – Set 2 – Photographs obtained for: Emulsion 30% silicone oil in distilled water; 15% quartz powder and distilled water at 280 [rot/min] (Teodoriu R., 2021).

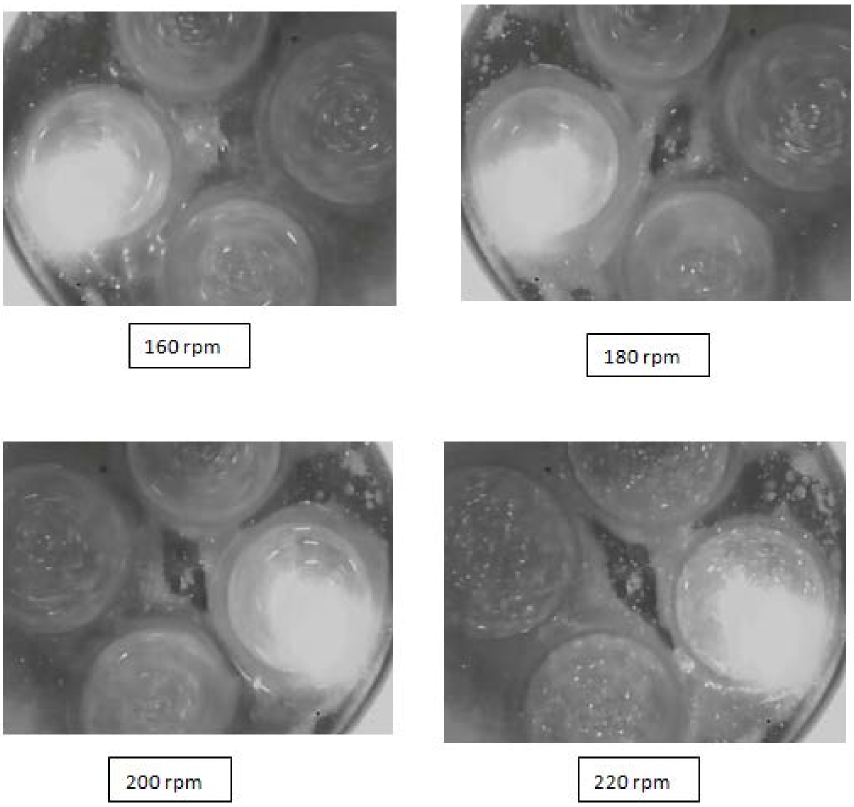

Fig. 5e – Set 3 – Photographs obtained for: silicone oil 98% + distilled water without forming an emulsion at 160; 180; 200 and 220 [rot/min] (Teodoriu R., 2021).

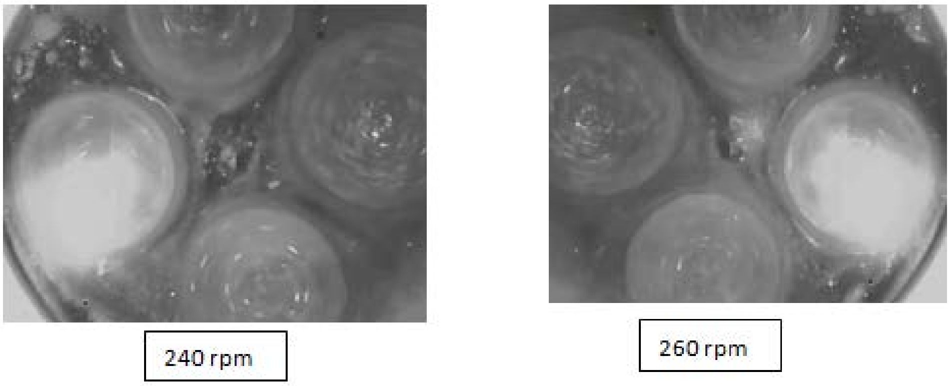

Fig. 5f – Set 3 – Photographs obtained for: silicone oil 98% + distilled water without forming an emulsion at 240 and 260 [rot/min] (Teodoriu R., 2021).

5. Conclusions

Experiments have shown the possibility of visualisation of flowing phenomena inside the four-roll mill designed and constructed by Adrian Teodoriu based on digital collected video data processed using dedicated software and thus confirming the equipment capability.

Fourty years ago, Wong imagined the theoretical solution “the precise control of the processes where more information is needed requires programs and specialised apparatus” (Wong, 1979).

Comparing with the results reported in 1990 by Lagnado and Leal using their sophisticated equipment, the one used by us is far away in what concern the possibilities of control.

Today, the continuous control in real time for the processes based on video images and video feedback is still difficult to achieve. The motives are known and they are: the great content of data colected and contained in each video frame. Solving the problem requires a large computing power capable of receiving, processing and delivering results in fractions of a second.

Taking into account the fact that calculus power increases day by day due to efforts and results already obtained in the field of hardware and software improvements, we believe that the complex control problems will be soon handled using feed back from video sources.

Similar applications in the robotics determined the technology to advance toward that moment. Such a technology is being tested nowadays, in a much more complex situation, with relative success in transportation, the case of autonomous car.

REFERENCES

Bentley B.J., Leal L.G., *A computer-controlled four-roll mill for investigations of particle and drop dynamics in two-dimensional linear shear flows*, J. Fluid Mech., vol. 167, 219-240, (1986).

Lagnado R.R., Leal L.G., *Visualization of three-dimensional flow in a four-roll mill*, Experiments in fluids, 9, 25-32, (1990).

Mackley M.R., Keller, A., *Flow induced polymer chain extension and its relationship to fibrous crystallization*, Phil. Trans. Roy. Soc., London, A 278 (29): 4–79, (1975).

Taylor G.I., *The formation of emulsions in definable fields of flow*, Proc. Roy. Soc., London, A l46, 501–523, (1934).

Teodoriu A., *Proiectarea și realizarea unui laminor cu patru role*, Lucrare de disertație, Universitatea Tehnică “Gheorghe Asachi” din Iași, Facultatea de Știința și ingineria materialelor, Iași, 2021.

Teodoriu R., *Studiul experimental al fenomenelor de curgere într-un laminor cu patru role*, Lucrare de disertație, Universitatea Tehnică “Gheorghe Asachi” din Iași, Facultatea de Știința și Ingineria Materialelor, Iași, 2021.

Wong V.S., *Computational structures for extracting edge features from digital images for real time control applications*, Ph.D. Disertation, California Institute of Ttechnology, 1979.

STUDIU EXPERIMENTAL AL FENOMENELOR DE CURGERE UTILIZÂND UN LAMINOR CU PATRU ROLE

(Rezumat)

Această lucrare își propune să analizeze fenomenele de curgere utilizând un echipament experimental și anume, un laminor cu patru role din dotarea laboratorului Facultatii de Știința și Ingineria Materialelor de la Universitatea Tehnică “Gheorghe Asachi” din Iași. Metoda vizualizării fluxului de fluid a fost utilizată pentru a studia mişcarea unui fluid newtonian într-un laminor cu patru role. Sunt raportate observațiile efectului creșterii turației rotoarelor asupra evoluției fluxului constant tridimensional între role. Experimentele de vizualizare a fluxului au fost efectuate în seturi, prin variația turației. Rolele au fost constrânse să se rotească într-o manieră care generează o curgere liniară aproximativ bidimensională în apropierea centrului aparatului, la viteze mici. Vortexurile stabile, poziționate simetric cresc în apropierea pereților superiori și inferiori ai cuvei, pe măsură ce numărul Reynolds creşte până la o valoare critică. O creştere a numărului Reynolds dincolo de această valoare critică are ca rezultat o pierdere de simetrie în aspectul fluxului.

BULETINUL INSTITUTULUI POLITEHNIC DIN IAŞI
Publicat de
Universitatea Tehnică „Gheorghe Asachi” din Iaşi
Volumul 68 (72), Numărul 1-4, 2022
Secţia
ŞTIINŢA ŞI INGINERIA MATERIALELOR

A SHORT INTRODUCTION OVER THE KNOWLEDGE OF MORTARS WITH MICRO AND NANOMETRIC INSERTS OF DIFFERENT GEOMETRIES IN THE FIELD OF CIVIL ENGINEERING

BY

ELENA BASALIC*, IOANA SORINA ENȚUC, CARMEN NEJNERU, RALUCA FLOREA, COSTEL DOREL FLOREA, ANA-MARIA SCRIPCARIU, PETRONELA PARASCHIV and CIMPOEȘU NICANOR

“Gheorghe Asachi” Technical University of Iaşi,
Department of Materials Science and Engineering, Iași, Romania

Received: August 5, 2022
Accepted for publication: September 9, 2022

Abstract: With an average of about a ton of cement produced each year for every person in the world, the cement industry is the second largest producer of greenhouse gases on our planet. Carbon is not just a simple singular element in the periodic table of elements, is the sixth most abundant element in the universe: about 0.5 ppm and with about 0.20% by weight only in the terrestrial environment, and it is a fundamental element for the all living world. As Primo Levi had once mentioned, carbon can bind itself or other light atoms without spending much energy. Our interest goes to properties and characteristics of carbon as a solid and as a material.

If we consider the potential of carbon nanotubes (CNT) as superior additives for hardening concrete and improve the appropriate impermeability against different water-cement (W / C) ratios, we can consider a transition zone between aggregates and cement paste, which is the most vulnerable concrete component and always limits the properties and applicability of concrete (Cwirzen, 2021a). Construction as a work sector requires about 85% of the planet's natural resources and has a huge impact on the environment using about

*Corresponding author; *e-mail*: mocanu.basalic.elena@gmail.com

60% of raw materials extracted from the lithosphere, most reaching waste, which produced the need to develop other types of concrete and mortars that may reduce greenhouse gas emissions (Cwirzen, 2021b). Begin with the 1980s, the only known allotropic forms of carbon have been diamond and graphite. But, in 1985 and 1991, respectively, two new forms of trigonal carbon (sp 2 hybridized) were discovered: fullerenes and nanotubes (Delha`es *et al*., 2006). Carbon nanotubes (CNTs) are allotropic forms of carbon with a nanostructure that can have a length-to-diameter ratio greater than 10,000. These cylindrical carbon molecules have useful properties in many applications in nanotechnology, electronics, optics and in many fields of materials science. The calculation methodology of the reinforcement of the reinforced concrete structural elements follows the behavior at efforts at macrolevel of the structural elements, the followed result being the capacity of the reinforced concrete element itself to take over a predetermined effort (Dresselhaus *et al*., 1995).

Keywords: nanotechnology, nanaotubes, sustenability, SWCNT, Carbon nanotubes, Portland cement, Hydration, porosity, mechanical property.

1. Introduction

The discovery of new nanostructures by Sumio Iijima (Japanese physicist and inventor) led to various applications of nanomaterials in various fields of study. Undoubtedly, the excellent properties and high strength/weight ratio of the structures have greatly helped the various applications that are exemplified in nanomechanical systems, nanoelectronics, nanobiological systems, nanodevices, nanocomposites (Endo *et al*., 1996). This is because the CNT’s undergo large deformations in the elastic limit and vibrate at a frequency in the order of GHz and THz.

Such are the interests of researchers to provide a physical and practical perspective on the dynamic behaviors of new structures. In a later paper on the dynamic behavior of nanostructure, Civalek *et al.* applied Eringen's theory of non-local elasticity to investigate the static analysis of single-walled carbon nanotubes (SWCNT).

A few years later, Akgöz and Civalek adopted the strain gradient theory to analyze the bending of embedded carbon nanotubes that rest on an elastic foundation. Meanwhile, in another paper, the authors studied the effects of size on the static response of SWCNT using the elasticity of the deformation gradient. Civalek and Demir used non-local Euler-Bernoulli beam theory to explore behaviors those bent microtubes (Shahriar Dastjerdi *et al*., 2018).

2. Materials and Processes

Graphite or carbon nanomaterials offer different characteristics for the efficient consolidation of cemented matrices. Cemented composites have good compressive strength, but low strength, ductility and flexibility. They can be improved by nanotechnology due to the physical behavior and size of hydration products.

Nanomaterials have distinct physical and chemical properties that can lead to improved material performance. Nanomaterials have distinct chemical and physical properties that can lead to improved material performance (Li *et al*., 2004) but are also easy to manipulate through nanotechnology. The behavior of concrete structures over time is partially determined by the quality of the microstructure and mass transfer at the nanoscale (Tasis, 2013). Cemented materials are fragile and have low tensile strength, but the physical structure Cement hydration products show defects in the cemented matrix that exists at the nanoscale.

The usage of nanoscale fibers can significantly control cracks in the nanoscale cement matrix and result in more resilient and hard composites. The superior mechanical properties of CNTs make it a better candidate as a reinforcement material in cement matrix composites. CNT can be considered an exceptional reinforcement material due to its extremely high strength/mass ratio (Yang Mu Han *et al.*, 2004), ultralight, high tensile strength, excellent electrical conductivity of the module and elasticity, chemical and thermal stability. CNT nano-dimensions allow them to be distributed in the cement matrix on a much finer scale, compared to traditional reinforcement fibers.

The mechanism of growth of MWNT without a catalyst is not known exactly. A very important step, called nucleation, may include the formation of the C2 precursor and its subsequent incorporation into the primary structure of graphene. Based on observations of transmission electron microscopy (TEM), Ijiima and colleagues proposed a growth mechanism in which carbon atoms are added to the open ends of the tubes and the growth ends remain open during growth. The thickening of the tube occurs by increasing on the island the basal planes of graphite on the surfaces of the existing tube. Tube growth ends when conditions are not suitable for growth. Generally, the quality and yield of nanotubes depend on the processing conditions employed, such as efficient cooling of the cathode, the gap between electrodes, reaction chamber pressure, uniformity of the plasma arc, plasma temperature, and so on.

Original report of Iijima (Iijima and Ichihashi, 1993) about research in the field of carbon nanotubes has been recognized as exceptional materials with nanometric dimensions and could create new interesting fields of carbon chemistry and physics. Nanotubes prepared in a direct current discharge using graphite electrodes at temperatures above 3000°C below helium were first reported by Iijima and later by Ebbesen and Ajyayan. Similar tubes, which we call pyrolytic carbon nanotubes (PCNTs), are produced by the pyrolysis of hydrocarbons (benzene at about 110°C); PCNTs can be prepared using the same technique used to produce so-called steam-grown carbon fibers (VGCF).

The idea of discovering carbon nanostructures (CNT) came from the physicist and inventor Sumio Iijima and had and has applications of nanomaterials in various fields of study such as nanomechanics, nanoelectronics, nanobiological systems, nanodevices, nanocomposites, due to their distinct chemical and physical properties. And the high strength/weight ratio of the structures because CNTs suffer large deformations in the elastic limit and vibrate at frequency in the order of GHz and THz and can lead to improved material performance (Li *et al*., 2004; Iijima and Ichihashi, 1993).

The application of nanoscale fibers can significantly control cracks in the nanoscale cement matrix and result in stronger and harder composites. The excellent mechanical properties of CNT's make it a good candidate as a reinforcement material in cement matrix composites. CNT can be considered an exceptional reinforcement material due to its extremely high strength / mass ratio, ultra-high strength, ultra-light, high tensile strength, conductivity, excellent modulus electrical and elasticity, chemical and thermal stability. CNT nanodimensions allow them to be distributed in the cement matrix on a much finer scale, compared to traditional reinforcement fibers (Kazuyoshi *et al*., 1999).

Carbon nanotubes are microscopic structures similar to graphite, discovered in 1990 and have a diameter of about 50,000 times smaller than hair (Fig. 1). Carbon nanotubes have special electrical, mechanical and thermal properties: high electrical conductivity - can be 1000 times higher than that of copper, a hardness approximately equal to that of diamond - the hardest material in nature (high frequency vibrations of CC bearing ensures a higher intrinsic thermal conductivity even than that of diamond) and a mechanical tensile strength approximately 14 times higher than kevlar - polyamide 5 times stronger than steel considered at an equal weight (according to YOUNG Modulus, a scale of stiffness measurement, the stiffness of CNTs is 5 times higher than that of steel).

Calculations show that the wire of multi-layered carbon nanotubes, with a thickness of 1 mm, could maintain a weight of up to 15 tons. Simultaneously, in a cross-section, it keeps the heat the same as brick or concrete. One review was given by Sattler, who succeeded in his study in obtaining scanning-casting microscopy (STM) images of the surfaces of carbon nanotubes with atomic resolution (Loiseau *et al*., 2006).

A comparative study of common defects found in carbon nanotubes, including topological, hybridization, and solder defects, was conducted by Ebbesen and Takada. The application of nanometer-scale carbon or graphene fibers can significantly control cracks that occur in the nanoscale cement-based mortar matrix and result in stronger composites with higher compressive strength / tensile / conductivity/ electrical / elasticity and chemical and thermal stability due to the nano-dimensions that allow them to be distributed in the cement mortar matrix on a much finer scale, compared to traditional reinforcement fibers. A schematic classification of the different forms of carbon is presented in Table 1.

Table 1
Schematic classification of the different forms of carbon (Loiseau et al., 2006)

Cristalline Form	Diamonds	Graphites	Carbynes*	Nanotubes
Hybridization	sp3	sp2	sp1	sp2+e
Coordinance z	4	3	2	3
Physical dimensionality D	3	2	1	0 and 1
Bond length (A)	1.54	1.4	1.21	1.33 to 1.40
Bond energy (e V/ mole)	15	25	35	>25
*Also mixed sp1 and sp3 hybridizations (α form)				

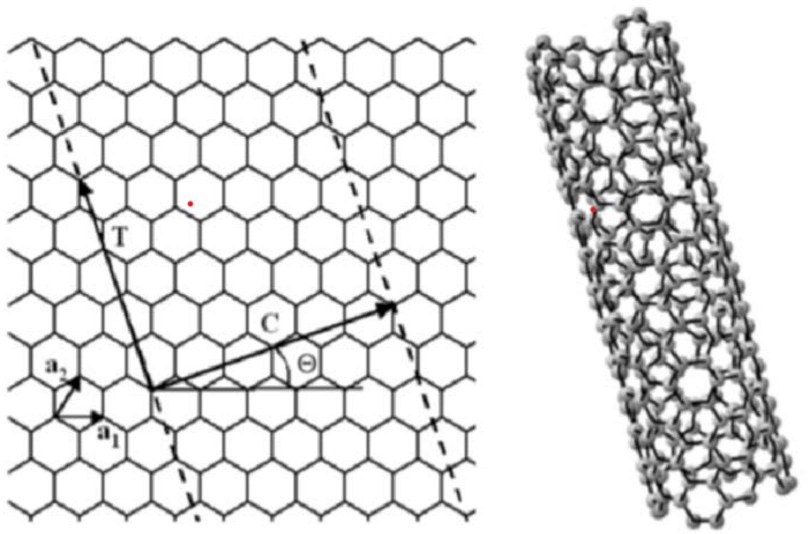

Fig. 1 – Left: the principle of nanotube construction from a graphene sheet.
Right: Example of a nanotube (Loiseau *et al*., 2006).

3. Conclusions

The global nanomaterials market, including carbon nanotubes (CNTs) and carbon nanofibers (CNFs), has drastically grown over the last few decades, and continues to attract attention from numerous industries, including the construction sector. Continuous research and development efforts in the academic and industrial sectors have led to innovative technologies for the manufacture of low-weight carbon nanotubes (CNTs), excellent electrical, mechanical and thermal characteristics. Consequently, CNTs provide opportunities for the development of advanced functional materials. The researchers reported a remarkable improvement in the mechanical properties of metals and ceramics by adding low loading levels of CNTs. Carbon nanotubes can strengthen metals and ceramics through the load transfer effect and can strengthen brittle ceramics through a crack-bonding mechanism (Loos, 2015; Marcaccio and Paolucci, 2013). CNT-reinforced composites also have excellent electrical and thermal conductivity.

The principles of consolidation, deformation, mechanical failure, electrical and thermal transport of these nanocomposites, viewed from a fundamental perspective, are not fully understood and tested. in specific applications (Meyyappan, 2005). To date, only a few of the inventions have been recognized by patent authorities for the possible marketing of CNT-reinforced composites. This is due to the low production efficiency and high cost of CNTs.

Thus, multifunctional composites with improved mechanical, electrical and thermal properties can be prepared by adding a low nanotube content. Such nanocomposites are considered as an important new class of structural materials for mechanical components of microelectromechanical systems, such as high frequency micromechanical resonance devices (Ramírez *et al*., 2018; Tanaka *et al*., 1999). One of the obstacles to the sale of reinforced metals with CNT is the high cost of CNT and the agglomeration of fillers in metal matrices. If there are more efficient applications of CNT-reinforced light metals as structural and functional materials in the future to further improve processing techniques and reduce costs, they will be more affordable (Tasis, 2013; Tjong, 2008).

REFERENCES

Cwirzen A., *Introduction to concrete and nanomaterials in concrete applications, Carbon Nanotubes and Carbon Nanofibers in Concrete-Advantages and Potential Risks*, Science Direct, Micro and Nano Technologies, 2021a, 1-58.

Cwirzen A., *Potential hazardous effects of carbon nanotubes and carbon nanofibers, Carbon Nanotubes and Carbon Nanofibers in Concrete-Advantages and Potential Risks*, Science Direct, Micro and Nano Technologies, 2021b, 335-347.

Delha`es P. *et al*., *Polymorphism and Structure of Carbons*, Lect. Notes Phys. 677, 1-47 (2006), www.springerlink.com.

Dresselhaus M.S., Dresselhaus G., Eklund P.C., *Science of Fullerenes and Carbon Nanotubes*, Copyright 1995 University of Kentucky (~ Copyright 9 1996, Elsevier Science (USA).

Endo M., Sumio Iijima, Mildred S. Dresselhaus, *Carbon nanotubes*, 1996 Elsevier Science Limited.

Iijima S., Ichihashi T., *Single-shell carbon nanotubes of 1-nm diameter*, Nature, 363, 603-605 (1993).

Kazuyoshi T., Tokio Yamabe, Kenichi Fukui, *The Science and Technology of Carbon Nanotubes*, 1999, Elsevier.

Loiseau A., Launois P., Petit S., Roche J.-P. Salvetat, *Understanding Carbon Nanotubes*, Springer, Berlin Heidelberg 2006.
Loos M., *Carbon Nanotube Reinforced Composites*, 2015.
Marcaccio M., Paolucci F., *Making and Exploiting Fullerenes, Graphene, and Carbon Nanotubes*, 2013.
Meyyappan M., *Carbon nanotubes, Science and applications*, 2005.
Ramírez C.P., Evangelina Atanes Sánchez, Mercedes del Río Merino, Carmen Viñas Arrebola, Alejandra Vidales Barriguete, *Feasibility of the use of mineral wool fibres recovered from CDW for the reinforcement of conglomerates by study of their porosity* , Science Direct, Volume 191, 10 December 2018, 460-468.
Tanaka K., Tokio Yamabe, Kenichi Fukui, *The Science and Technology of Carbon Nanotubes,* 1999, Elsevier.
Tasis D., *Carbon Nanotube–Polymer Composites*, RSC Nanoscience & Nanotechnology, No. 27, The Royal Society of Chemistry 2013.
Tjong S.C., *Carbon Nanotube Reinforced Composites Metal and Ceramic Matrices*, 2008.
Shahriar Dastjerdi, Bekir Akgöz, Leila Yazdanparast, *A new approach for bending analysis of bilayer conical graphene panels considering nonlinear van der Waals force*, 2018, Journal- Composites ,124-134.
Xiaodong Li, Hongsheng Gao, Wally A Scrivens, Dongling Fei, Xiaoyou Xu, Michael A Sutton, Anthony P Reynolds and Michael L Myrick, *Nanomechanical characterization of single-walled carbon nanotube reinforced epoxy composites*, 2004.
Yang Mu Han, QingYu Jia, Chuan Zheng Shu, Juan Zhang Guo, PingSheng, *Reductive degradation of nitrobenzene in aqueous solution by zero-valent iron*, Vol. 54, Issue 7, February 2004, Pages 789-794.

O SCURTĂ ANALIZĂ ASUPRA CUNOAŞTERII MORTARELOR CU INSERŢII MICRO ŞI NANOMETRICE DE DIFERITE GEOMETRII ÎN DOMENIUL INGINERIEI CIVILE

(Rezumat)

Consumul excesiv în materie de consumabile în domeniul materialelor de construcţii a dus, treptat, la o necesitate de optimizare atât în ceea ce priveşte compoziţia materialelor compozite ranforsate cât şi în ceea ce priveşte minimalizarea/ încetarea / întârzierea mecanismelor de degradare ale materialelor compozite care cauzează reducerea proprietăților mecanice, în special rezistenţa la tracţiune sau la încovoiere, sau a proprietăţilor elastice, apărute la interfaţa lucrărilor cu mortare în domeniul ingineriei civile.

Nanomaterialele din grafit oferă, astfel, caracteristici distincte pentru consolidarea optimă a matricilor cimentate în intervalele de comportament pre-fisură şi post-fisură.

Cercetarea în vederea introducerii unui material compozit ranforsat hibrid a apărut din nevoia de a spori rezistenţa la întindere, blocarea fisurilor, eliminarea

tensiunilor reziduale interne şi reducerea comportamentului ductil al materialului şi are ca scop optimizarea compoziţiei / dozajului unui material compozit pe baza nanotuburilor de carbon, care să fie axat pe mortar de ciment îmbunătăţit cu fibre sau cu adaosuri de polimeri, datorită avantajului pe care microstructura acestuia o reprezintă în comparaţie cu betonul când este vorba de armare cu fibre la nivel micro în matricea minerală. Matricea de ciment este practic un material compus din calciu hidroxid (portlandit), aluminaţi, şi ciment nehidratat (clincher), dizolvat într-un produs de hidratare amorf nanostructurat numit gel C-S-H (hidrat de silicat de calciu), care este esenţial pentru proprietăţile mecanice bune ale pastei de ciment.

BULETINUL INSTITUTULUI POLITEHNIC DIN IAŞI
Publicat de
Universitatea Tehnică „Gheorghe Asachi” din Iaşi
Volumul 68 (72), Numărul 1-4, 2022
Secţia
ŞTIINŢA ŞI INGINERIA MATERIALELOR

MULTI-DISCIPLINARY OPTIMIZATION OF A SPACECRAFT FOR A RE-ENTRY DESCENT FROM LEO ORBIT AT COSTANT HEAT FLUX DENSITY

BY

NICOLINA MONTELLA[∗]

University of Campania, “L. Vanvitelli”
Department of Engineering, Via Roma 29, I-81030, Aversa (CE), Italy

Received: June 20, 2022
Accepted for publication: July 25, 2022

Abstract. This paper deals with a pre-feasibility analysis of a new re-entry approach for manned missions based on a longer and more gradual conversion of the internal energy of the vehicle into thermal energy, which means keeping the heat flux constant and having lower thermal peaks. This implies the possibility of using less performing and, therefore, less expensive materials.

This approach has been developed for a highly innovative re-usable wing-body concept with high surface-to-mass ratio. A flight path angle lower than typical Shuttle-like values, namely -0.1 deg, is used to carry out the gradual dissipation of vehicle’s total energy. To assure the desired convective heat flux level for a certain time, the selected flight approach uses a prescribed guidance law which modulates the glider angle of attack as a function of Mach number.

Consequently, an optimization procedure developed to keep a constant heat flux with a parametric guidance law is performed.

Keywords: Spacecraft, LEO re-entry, heat flux control, multi-disciplinary optimization, guidance law.

[∗]*e-mail*: nicolina.montella@unicampania.it

1. Introduction

One of the main reasons why the Space Shuttle has been retired is the high cost of the windside Thermal Protection System (TPS) replacement after each re-entry (Dirkx and Mooij, 2017). Conversely, a reusable re-entry vehicle is currently required for the increasing demand of space tourism and to provide the International Space Station (ISS) crew with safe and fast way to return to Earth in case of emergency.

The Space Shuttle re-entered the Earth atmosphere with a high Angle of Attack (AoA) and with a blunt shape. Therefore, a high amount of vehicle total energy is dissipated in a very short time interval during re-entry (Han *et al.*, 2020). In this paper, different strategies to improve LEO re-entry are analyzed. In particular, a specific modulation of AoA is implemented to ensure a heat flux peak lower than a prefixed value and to keep this flux constant for enough time to take advantage of radiative cooling. For this purpose, a small flight path angle is considered ($\gamma = -0.1°$). In this way, a re-usable TPS, with a very big advantage in terms of maintenance costs, can be used. In addition, if the TPS has not to be replaced after every re-entry, the vehicle is immediately available as crew support in the case of necessity.

For all these purposes, an innovative re-usable Blended Wing Body (BWB) concept with rather high surface-to-mass ratio (S_r/m) is considered, see Fig. 1.

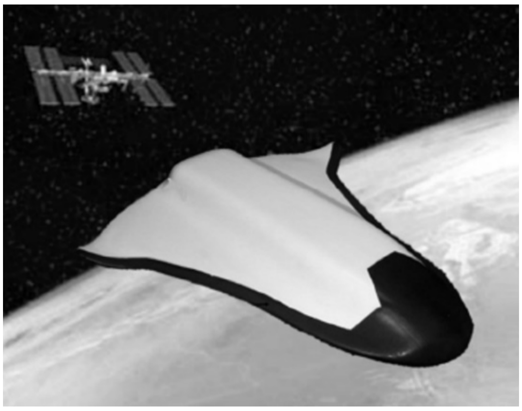

Fig. 1 – Pictorial representation of the Spacecraft under investigation.

This vehicle configuration is the result of a multi-disciplinary optimization of a previous work in which the mass was minimized, and the cross-range maximized, in order to ensure a safe landing on a conventional runaway (Viviani *et al.*, 2017a, b). In addition, a more effective TPS modelling procedure, consistent with a shallower re-entry, was developed (Aprovitola, 2019). Then, CFD simulations are performed in order to validate the vehicle aeroshape at hypersonic and supersonic speeds (Viviani *et al*., 2020a).

Finally, preliminary information about spacecraft landing capability on runway was provided by adding to the vehicle design two functionally independent body flaps (Viviani *et al*., 2020b).

In this framework, using this prefixed aeroshape, a heat flux tracking procedure based on a prescribed Guidance Law (GL), which modulates the AoA in function of the – Mach number, was performed. The GL was implemented with a parametric model and the best GL was found in order to obtain a rather constant heat flux at stagnation point with a peak lower than 600 kW/m^2, which is the maximum heat flux that the TPS material considered can withstand. Parametric cubic spines have been used to model the GL and a single-objective optimization procedure driven by a genetic algorithm has been performed.

2. Research background

During re-entry, a winged vehicle experiments very critical thermal load. In the case of the Shuttle, at about 80 km of altitude, the heat flux is about 70% of its maximum value (Walter, 2018). In literature, two approaches are considered to develop guidance schemes based on re-entry corridor (Zhou *et al*., 2020). These approaches exploit both offline and online trajectory design. In the offline approach, a feedback is assigned to keep the vehicle inside the re-entry corridor (Guo and Wang, 2015), while in the online approach the trajectory is repeatedly optimized online with a big computational cost (Guo *et al*., 2011).

In (Mooij, 2017) a guidance system for heat flux tracking is designed to test new insulating materials. In (Vernis *et al*., 2007), a genetic algorithm was used in order to perform a global optimization of the re-entry trajectory.

In (Chawla *et al*., 2010) a trajectory optimization of a Hypersonic Gliding Vehicle (HGV) accounting maximum dynamic pressure and heat rate constraint was designed. In (Zhao and Song, 2017), the orbit re-entry trajectory of a Common Aerial Vehicle (CAV) satisfying no fly-zone constraints and path requirements was analysed using convex programming.

3. Research framework

The aim of this paper is to approach a shallow re-entry flight (*i.e.*, $\gamma \ll 1$) of a spacecraft which low wing loading (*i.e.*, high S_r/m) which re-enters from LEO. The vehicle configuration adopted in this work is shown in Fig. 2.

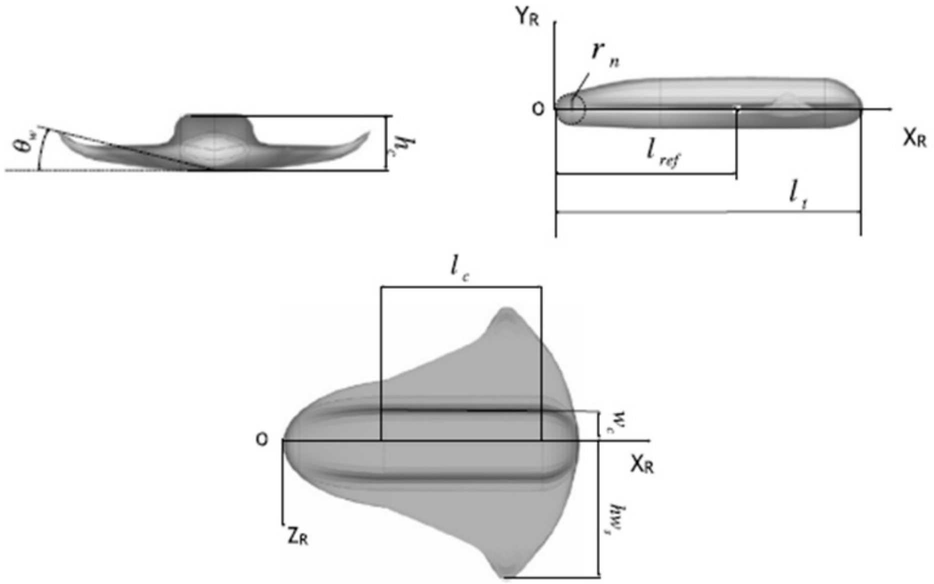

Fig. 2 – Vehicle overall dimensions.

The overall aeroshape dimensions are: $l_t = 9.25\text{m}$; $h = 1.5\text{m}$; $h_{ws} = 4.3\text{m}$; $r_n = 0.469\text{m}$; $\theta = 40°$. This vehicle configuration is characterized by a rather blunt flat-bottomed aeroshape to improve the thermal dissipation at high-speeds, and a delta planform shape with high swept to improve low speed aerodynamics through the vortex-lift contribution (Viviani *et al*., 2020a). This aeroshape is the result of a multi-disciplinary optimization as discussed in (Viviani *et al*., 2017a, b) and (Viviani *et al*., 2020a, b).

The vehicle structure is insulated by a passive TPS, made of ceramic tiles and blankets. A high-temperature, carbon silicon-carbide hot structure with a surface coating is used for the more stressed vehicle surfaces (nose, wing leading-edge, tip fins and aerodynamic control surfaces) (Marley and Driscoll, 2017; Stanley, 2000).

The vehicle aeroshape was validated in (Viviani *et al*., 2020a).

After defined the vehicle configuration, it is mandatory to define a mathematical model of a re-entry flight. In particular, a point mass over a non-rotating spherical Earth model is considered (Fig. 3), leading to the following equations:

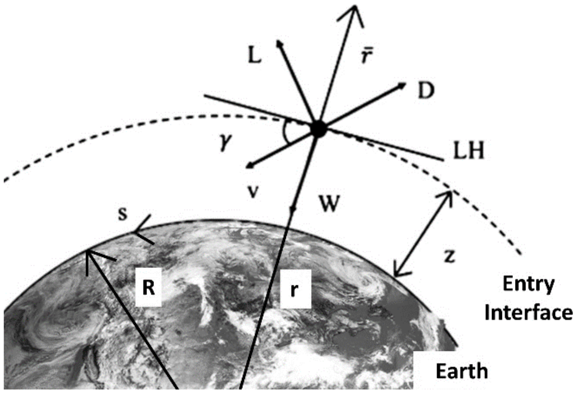

Fig. 3 – Re-entry layout.

$$\frac{dv}{dt} = -\frac{D}{m} - g\sin\gamma \tag{1}$$

$$v\frac{d\gamma}{dt} = \frac{L}{m}\cos\mu_a - \left(g - \frac{v^2}{r}\right)\cos\gamma \tag{2}$$

where the bank angle μ_a is the angle between the lift vector **L** and the x_k-axis (Fig. 4).

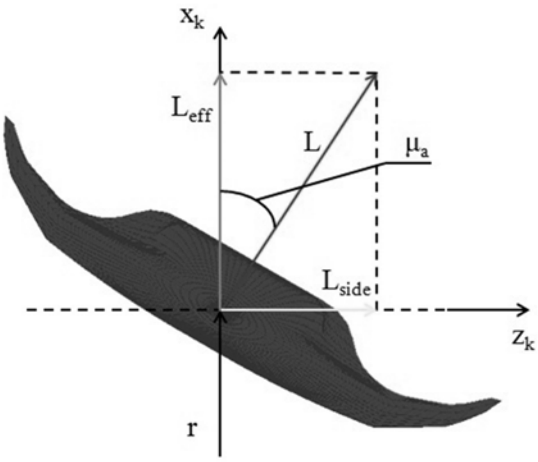

Fig. 4 – Bank angle definition.

The flight path coordinate system, or k-frame, is defined by the velocity vector (Fig. 5).

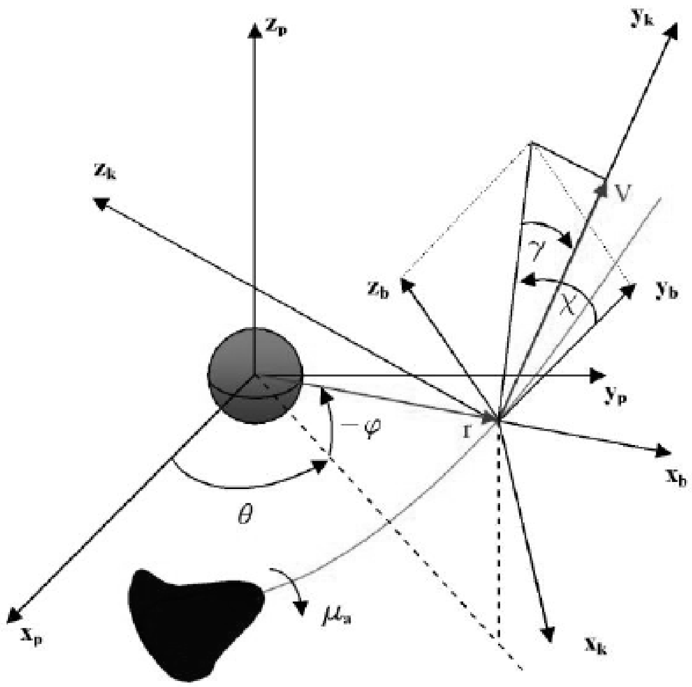

Fig. 5 – Flight path coordinate system definition

Altitude (z), and down-range (s) are expressed as follows:

$$\frac{dz}{dt} = v \sin \gamma \tag{3}$$

$$\frac{ds}{dt} = \frac{R}{r} v \cos \gamma \tag{4}$$

where r is the distance between the vehicle and the Earth center, and:

$$g = g_0 \left(\frac{R}{r}\right)^2 \tag{5}$$

and:

$$\begin{cases} L = \frac{1}{2}\rho v^2 c_L S_{ref} \\ D = \frac{1}{2}\rho v^2 c_D S_{ref} \end{cases} \tag{6}$$

where S_{ref} is the reference area.

For the sake of simplicity, banking modulation is not considered in the present model. Therefore, aerodynamic coefficients C_L and C_D depend on the AoA, α, and the flight Mach number, M_∞, and Reynolds number, Re_∞.

Initial conditions are given assuming $h(t_0) = 120\ \mathrm{km}$ and speed $V(t_0) = 7830\ \mathrm{m/s}$ for the integration of these equations.

Starting values for latitude, longitude and flight azimuth are set to zero.

In (Aprovitola *et al.*, 2021), the dependence between the flight re-entry time Δt and the aerodynamic efficiency was analyzed:

$$\Delta t \cong \frac{\overline{C_L}}{\overline{C_D}} \bar{f}_t(\rho, v) \tag{7}$$

where $\overline{C_L}/\overline{C_D}$ is the average aerodynamic efficiency along the trajectory and $\bar{f}_t(\rho, v)$ is the average of $\left(g - \frac{v^2}{r}\right)\frac{v}{\sqrt{\rho}}$ along the trajectory.

From Fig. 3, the dependence between the aerodynamic efficiency and flight path angle is simple to see. Therefore, considering Eq. (7), the dependence between flight path angle and re-entry time is easily to recognize.

In order to withstand the thermal and mechanical loads during the re-entry, the spacecraft should fly within a proper re-entry corridor bounded by: *i*) the aeroheating boundary and the normal load factor constraint at lower altitudes; *ii*) the equilibrium glide limit at high altitudes, as shown in Fig. 6:

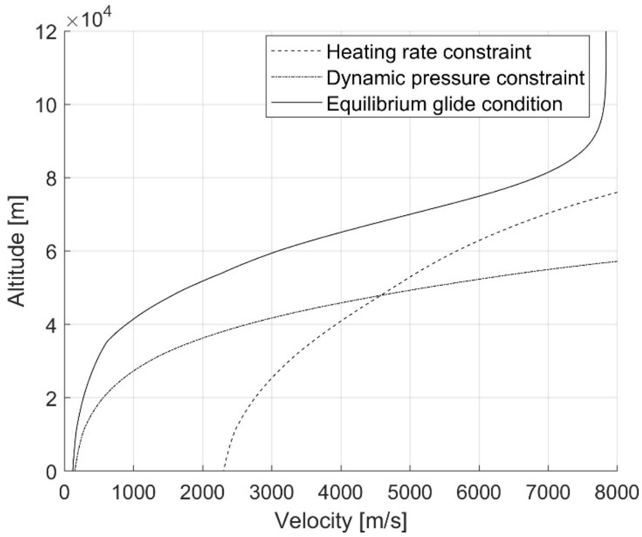

Fig. 6 – Re-entry corridor.

The aeroheating constraint identifies the couple (ρ_∞, v_∞) related to maximum stagnation point temperatures T_{wr0}. It depends, at a given altitude, on the geometrical radius of curvature of the vehicle leading-edge and the Thermal Protection Material (TPM) of the heatshield.

For this analysis, it is assumed $T_{wr0} = 1792\ K$. The Zoby's relationship describes the heat flux as:

$$\dot{q}_0 = K_Z \sqrt{\frac{p_s}{R_N}}(H_0 - h_w) \quad \left(\frac{W}{m^2}\right) \tag{8}$$

Where ρ_s is the stagnation pressure and $K_Z = 3.88 \times 10^{-4}$. $R_N = 0.469\ m$ is the vehicle's curvature radius.

Eq. (1-4) has been integrated by using a Runge-Kutta fourth order integrator. This integrator requires in input the GL and the Aerodynamic Database (DB) which provides for a prefixed aeroshape the aerodynamic coefficients that Eq. (6) needs. The GL has defined through natural splines and must be parametric in order to define the optimization problem. For this purpose, a variable number of control points (assigned in terms of couple (M_∞, α)) are analyzed to find the one that meets our requirements. In particular, the boundary control points corresponding to initial and final re-entry condition are fixed ($P_1(0.3, 10°)$ and $P_2(25, 45°)$), while the intermediate points are parametric:

$$\alpha_{i+1} = (\alpha_{i+2} - \alpha_1) \cdot Y_i + \alpha_1 \qquad (i = N-2, \dots, 1) \tag{9}$$

Expression (9) allows to represent only plausibly useful trends of the GL.

In Fig. 7, an example of GL is shown:

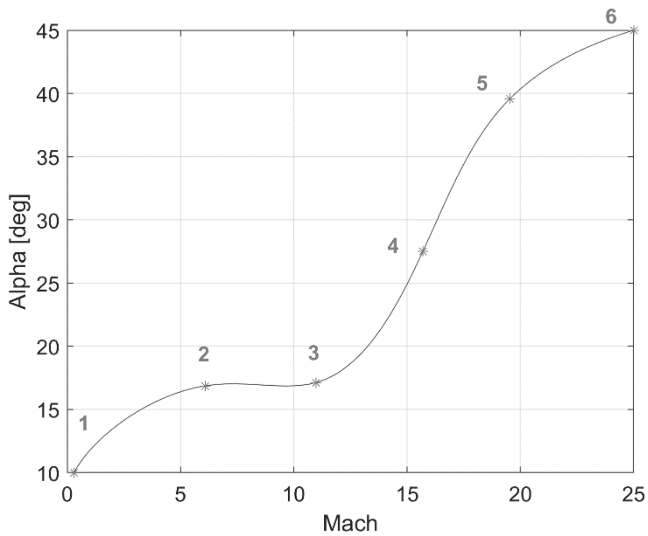

Fig. 7 – Example of GL.

4. Optimization procedure

The searched GL must guarantee a target heat flux of 600 kW/m^2 (aeroheating constraint in Fig. 6), which corresponds to a local radiative cooling temperature of about 1900 K, for a surface emissivity of 0.88. The chosen vale for the target heat flux value is, therefore, compliant with the operating temperature range (from 116.50 K to about 1922.05 K) of the material typically used for the fuselage nose heat shield, that is the Reinforced Carbon Carbon (RCC). The optimization problem is formulated with reference to the vehicle configuration described in Fig. 2. Initial entry conditions are given assuming: $V_e = 7830\ m/s$, $\gamma_0 = -0.1$, $\mu_{a_0} = 0$. The initial flight path angle (γ_0) are set on this value in order to ensure a re-entry as shallow as possible, while the initial bank angle (μ_{a_0}) is set equal to zero because, as said in the paragraph 3, no bank modulation is considered in this paper.

The re-entry corridor is bounded by the following operational constraints: dynamic pressure boundary $Q_{max} = 14\ kPa$; landing speed $V_L = 110\ m/s$; heat flux boundary $q_{max} = 600\ kW/m^2$, as shown in Fig. 4.

To have a constant heat flux at stagnation point, the trajectory must lie on the heat flux boundary. To make this possible, the objective function has defined as the area between the trajectory and the thermal constraint curve, starting from the beginning of the re-entry, up the intersection between the heat flux constraint curve and the dynamic pressure constraint curve (Fig. 8), as described in (Aprovitola *et al*., 2021).

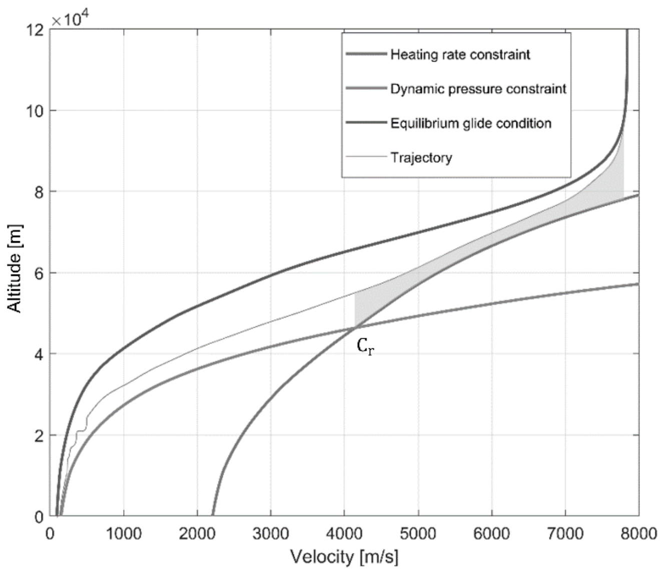

Fig. 8 – Objective function.

Formally, the objective function is expressed as follow:

$$\Delta A(\mathbf{x}) = \int_{M_{C_r}}^{M_\infty} (h^t - h^q) dM_\infty \approx \sum_{i=1}^{n-1} (A_i^t - A_i^q) \tag{10}$$

where $h^t = h^t(M_\infty)$ and $h^q = h^q(M_\infty)$ are respectively the trajectory and the assigned thermal constraint curve as functions of Mach number, while $\mathbf{x}$ is the current design vector and A_i^t and A_i^q are the areas below the curves numerically evaluated, providing a uniform sampling of h^t and h^q with n points.

To account for negative values of $\Delta A(\mathbf{x})$, Eq. (10) has been rewritten in this way:

$$\Delta A(\mathbf{x}) \approx \begin{cases} \sum_{i=1}^{n-1} (A_i^t - A_i^q) & \text{if} \quad A_i^t > A_i^q \\ \sum_{\substack{i=1 \\ i \neq (k_1 \dots k_n)}}^{n-1} (A_i^t - A_i^q) + \sum_{k=k_1}^{k_n} p \cdot |A_k^t - A_k^q| & \text{if} \quad A_k^t < A_k^q \end{cases} \tag{11}$$

where p is the penalty factor, which takes into account negative contributions to sum. If $(A_i^t - A_i^q) < 0$, its modulus is multiplied with coefficient p, and cumulated according to Eq. (11). The trajectory must also satisfy the dynamic pressure constraint in order to reach a globally feasible solution. For $M_\infty > M_{C_r}$ the dynamic pressure constraint is always satisfied (Eq. (11)); for Mach numbers $M_\infty < M_{C_r}$ an explicit constraint is required to take into account that the dynamic pressure constrain could be violated:

$$g(\mathbf{x}) = \begin{cases} 0 & \text{if} & h_i^t - h_i^d \geq 0 \\ \sum_{i=k_1}^{k_q} |h_i^t - h_i^d| & (k_1, \dots, k_q)| & h_i^t - h_i^d < 0 \end{cases} \tag{12}$$

where $h_i^t - h_i^d$ represents the altitude difference between current trajectory h_t and dynamic pressure limit h_d calculated at the same i-th point along the descent. If at generic point k_i the trajectory overcomes the dynamic pressure constraint, the difference $|h_i^t - h_i^d|$ is accumulated into the function $g(\mathbf{x})$ that becomes bigger and bigger as violations increase. Therefore, if we have a fully feasible trajectory with respect to the dynamic pressure, Eq. (12) becomes: $g(\mathbf{x}) = 0$.

The optimization problem is then formalized in this way:

$$\min \Delta A(\mathbf{x})$$

$$\underline{x_i} \leq x_i \leq \overline{x_i} \qquad i = 1, 2, \dots, I \tag{13}$$

$$g(\mathbf{x}) = 0$$

Each optimization process has been performed using the Multi-Optimization Genetic Algorithm (MOGA) available in the Ansys™ Workbench.

5. Optimization results

Different solutions are found modifying the number of parametric points.

Four equidistant (internal) control point are used for the first optimization procedure:

$$M_{i+1} = \frac{i}{5}(M_6 - M_1) + M_1 \qquad (i = 1, \ldots, 4)$$

$$\alpha_{j+1} = (\alpha_{j+2} - \alpha_1) \cdot Y_j + \alpha_1 \qquad (i = 1, \ldots, 4) \tag{14}$$

where $M_1 = 0.3$, $\alpha_1 = 10°$, $M_6 = 25$, $\alpha_6 = 10°$ are the boundary conditions. The re-entry trajectory path can be obtained by varying Y_i within normalized ranges:

$$Y_1 \in [0.1, 1]$$

$$Y_2 \in [0.2, 1]$$

$$Y_3 \in [0.5, 1]$$

$$Y_4 \in [0.6, 1] \tag{15}$$

The optimization results are show in Fig. 9.

This procedure considers acceptable a heat flux peak within a 3% range with respect to the prefixed heat flux limit.

The optimal design vector is $\mathbf{Y}_{\mathbf{opt}} = [0.676, 0.397, 0.656, 0.706]$, while the objective function is equal to $\Delta A(\mathbf{x}) = 0.7833e + 07$.

From Fig. 9b it is possible to observe that the trajectory lies on the thermal boundary curve only in a little velocity range (from about 6500 to about 5500 m/s). Consequently, the heat flux at stagnation point is not perfectly constant, even though there are no peaks.

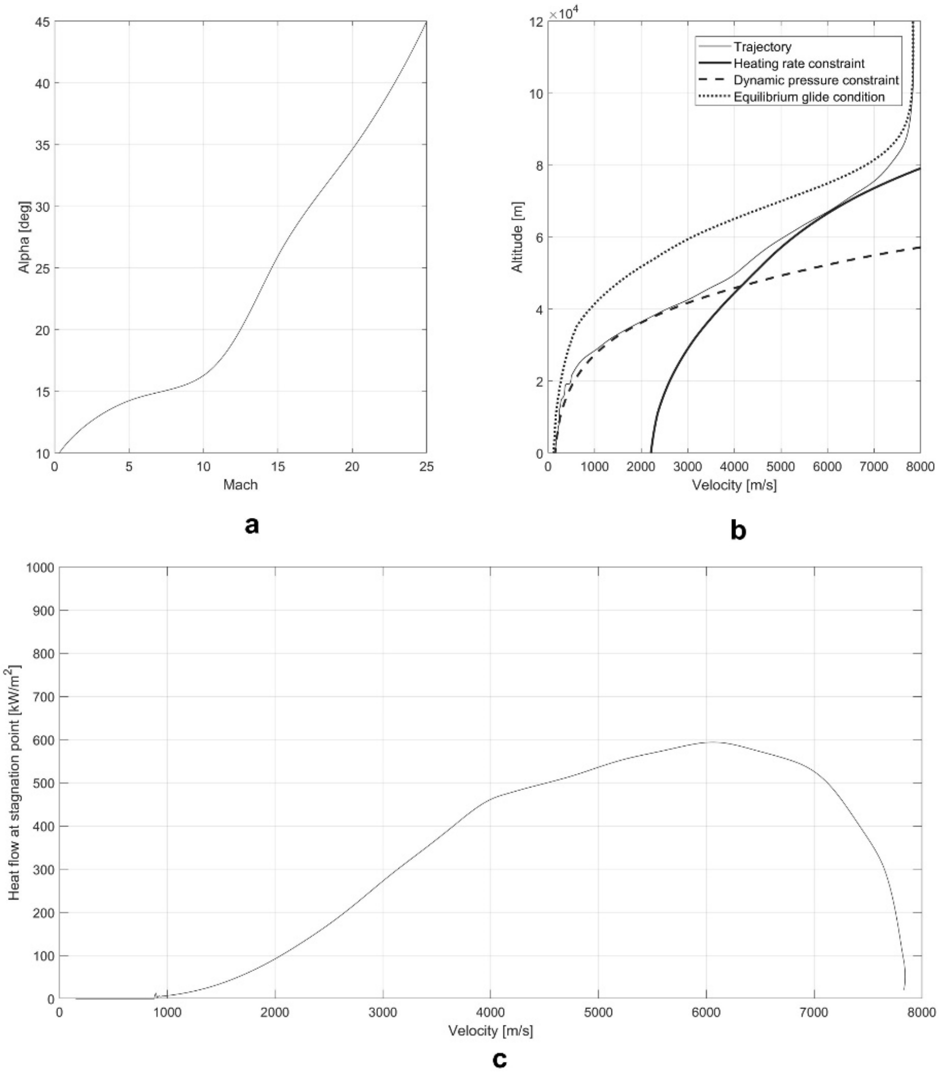

Fig. 9 a-c - Optimization results for 4 design points: Guidance Law (a); Optimized trajectory (b), Zoby's stagnation point heat-flux (c).

To give the trajectory the possibility to better follow the thermal boundary curve around the point C_r, two additional control points were added just near C_r, defined according to the following relations:

$$M_2 = \frac{1}{2}(M_{cr} - M_1) + M_1$$

$$M_3 = M_{cr} - \frac{1}{2}(M_{cr} - M_1)$$

$$M_4 = M_{cr} + \frac{1}{2}(M_{cr} - M_1)$$

$$M_5 = \frac{1}{4}(M_8 - M_{cr}) + M_{cr}$$

$$M_6 = \frac{2}{4}(M_8 - M_{cr}) + M_{cr}$$

$$M_7 = \frac{3}{4}(M_8 - M_{cr}) + M_{cr}$$

$$\alpha_{i+1} = (\alpha_{i+2} - \alpha_1) \cdot Y_i + \alpha_1 \quad (i = 6, \ldots, 1) \tag{16}$$

where $M_{cr} = 12.63$ is the Mach number at point C_r. Considering the boundary points $P_1(0.3, 10°)$ and $P_2(25, 45°)$, a eight control point spline is considered. The design variables vary within the following ranges:

$$Y_1 \in [0.1, 1]$$

$$Y_2 \in [0.2, 1]$$

$$Y_3 \in [0.3, 1]$$

$$Y_4 \in [0.5, 1]$$

$$Y_5 \in [0.5, 1]$$

$$Y_6 \in [0.5, 1] \tag{17}$$

The optimization results are shown in Fig. 10.

The optimal design vector is $\mathbf{Y}_{opt} = [0.910, 0.818, 0.561, 0.641, 0.746, 0.783]$, while the objective function is equal to $\Delta A(\mathbf{x}) = 0.7560e + 07$. The objective function has a value lower than which we have found in the previous case. Indeed, as shown in Fig. 10b, the trajectory lies nearly perfectly on the thermal curve. This happens because the two adding points around C_r allow to obtain the knee that we can see for a Mach number value between 10 and 15 and AoA of about 16° in Fig. 10a. This trend in turn gives the trend of the trajectory in Fig. 10b, that follows the thermal boundary trend better than the previous case. In fact, as you can see in Fig. 10c, the heat flux at stagnation point is nearly constant within a velocity range of about [4500, 6500] m/s.

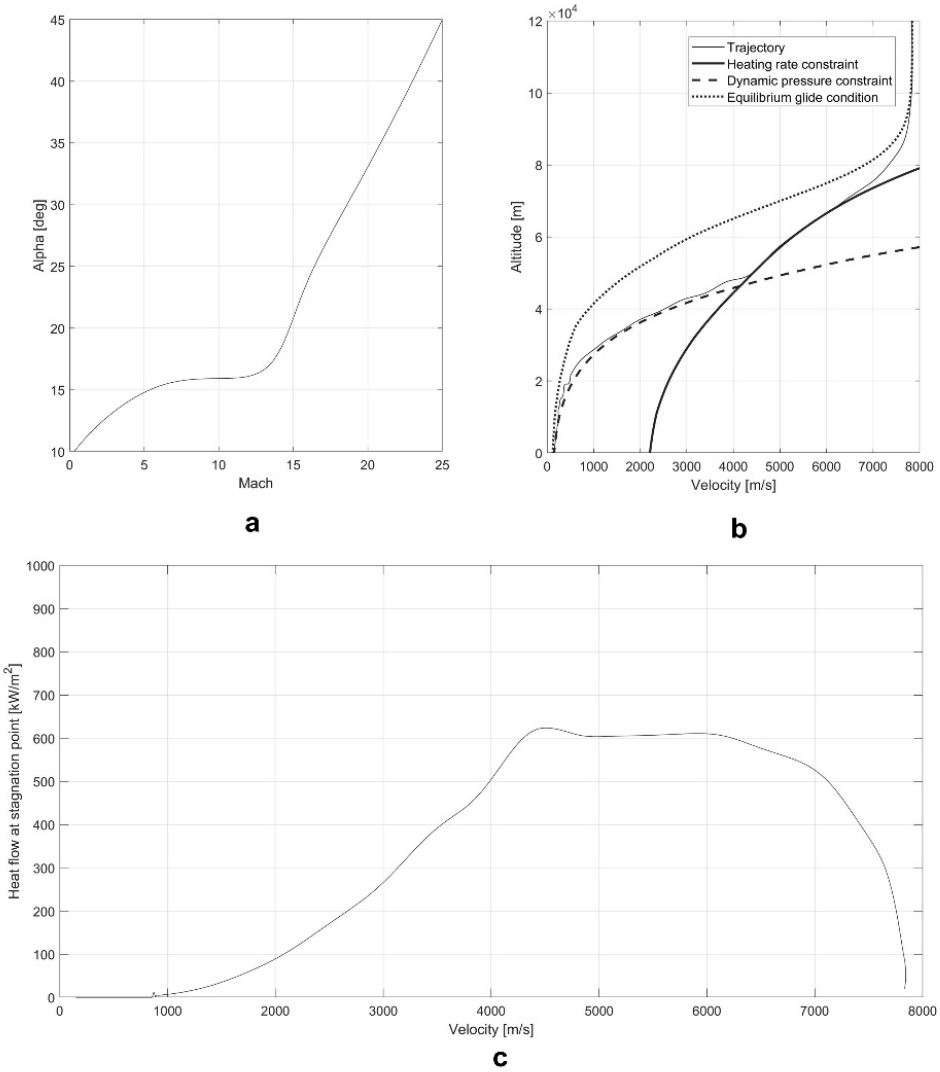

Fig. 10 a-c - Optimization results for 6 design points: Guidance Law (a); Optimized trajectory (b), Zoby's stagnation point heat-flux (c).

If we further increase the number of design variables, we can improve the modulation of AoA. In this case, we want to use only four intermediate equidistant control points, as in the first case described, but we want to consider not only the variation of the Mach component of every point but also the AoA component. Therefore, it is necessary to introduce the parameters X_j:

$$\alpha_{i+1} = (\alpha_{i+2} - \alpha_1) \cdot Y_i + \alpha_1 \qquad (i = 4, \ldots, 1)$$

$$M_{j+1} = (M_{j+2} - M_1) \cdot X_j + M_1 \qquad (j = 4, \ldots, 1) \tag{18}$$

The design variables are defined within the following ranges:

$$X_1 \in [0.1, 0.9]$$

$$Y_1 \in [0.1, 1]$$

$$X_2 \in [0.4, 0.9]$$

$$Y_2 \in [0.2, 1]$$

$$X_3 \in [0.5, 0.9]$$

$$Y_3 \in [0.5, 1]$$

$$X_4 \in [0.5, 0.9]$$

$$Y_4 \in [0.6, 1] \tag{19}$$

The optimization results are shown in Fig. 11.

The optimal design vector is:
$\mathbf{XY}_{opt} = [0.541, 0.958, 0.764, 0.425, 0.768, 0.517, 0.803, 0.667]$, while the objective function is equal to $\Delta A(\mathbf{x}) = 0.6079e + 07$.

As you can see in Fig. 11b, this solution is the one that best follows the thermal boundary curve. In fact, the knee in Fig. 11a is at lower AoAs than the previous case. As a consequence, the trajectory in Fig. 11b follows better the thermal constraint curve around C_r than the previous case. This leads to the best heat flux trend at stagnation point, that is constant in about the velocity range [4500, 6500] m/s. You can indeed observe that the objective function $\Delta A(\mathbf{x})$ is the one that gives the lowest value.

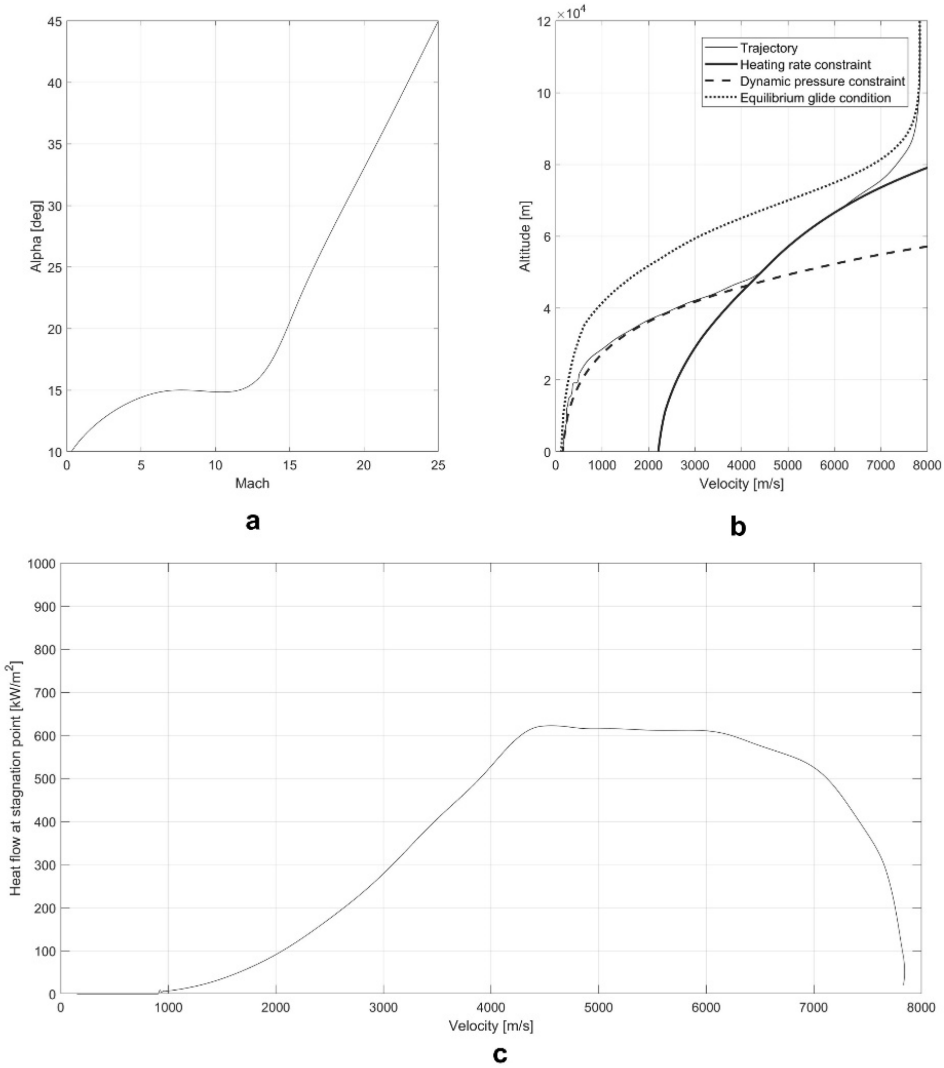

Fig. 11 a-c – Optimization results for 8 design points: Guidance Law (a); Optimized trajectory (b), Zoby's stagnation point heat-flux (c).

6. Conclusions

This paper has provided a new approach for future manned missions, based on hight S_r/m, as a conventional aircraft. Choosing a low flight path angle $(\gamma \ll 1)$ guarantees a shallower re-entry, that is the best choice to dissipate gradually the high kinetic energy of the vehicle at high altitudes. In this way, in fact, the vehicle flies for a long time and at a rather high altitude. In addition, this kind of re-entry makes it possible to landing at different sites thanks to the rather high range covered by the spacecraft during re-entry.

Taking into account these features, a single-objective optimization has been performed to obtain the GL that gives a constant heat flux value at stagnation point, modulating α in a range comprised between [20°, 45°] inside a Mach range between [15, 25]. Have a constant GL as long as possible allows to uniformly stress the TPS and, consequently, to have a reusable vehicle.

REFERENCES

Aprovitola A. et al., *An optima heat-flux targeting procedure for LEO re-entry of resuable vehicles*, Aerospace Science and Technology, Vol. 112 (2021).

Aprovitola A., Iuspa L., Viviani A., *Thermal protetion system design of a reusable launch vehicle using integral soft objects*, International Journal of Aerospace Engineering (2019).

Chawla C., Sarmah P., Padhi R., *Suboptimal reentry guidance of a reusable launch vehicle using pitch plane maneuever*, Aerospace Science and Technology, pp. 377-386 (2010).

Dirkx D., Mooij E., *Conceptual Shape Optimization of Entry Vehicles Applied to Capsuled and Winged Fuselage Vehicles*, Switzerland: Springer Aerospace Technology, 2017.

Guo M.W., Wang D.Y., *Guidance law for low-lift skip reentry subject to control saturation based on nonlinear predective control*, Aerospace Science and Technology, pp. 372-380 (2015).

Guo M.W., Wang D.Y., *Optimal guidance for reentry vehicles based on indirect Legendre pseudospectral method*, Acta Astronautics, pp. 1176-1184 (2011).

Han Q. *et al*., *Thermal protection of a hypersonic vehicle by modulating stagnation-point heat flux*, Aerospace Science and Technology (2020).

Marley C.D., Driscoll J.F., *Modeling an active and passive thermal protection system for a hypersonic vehicle*, AIAA Scitech Forum. - Grapevine, Texas: [s.n.], 2017.

Mooij E., *Heat-flux tracking for thermal protection system testing*, AIAA/AAS Astrodynamics Specialist Conference. - San Diego, California: [s.n.], 2017.

Stanley D., *Space transportation architecture for the future*, [s.l.]: Acta Atronautics, 2000.

Vernis P., Morio V., Ferreira E., *Genetic algorithm for coupled rlv trajectory and guidance optimization*, IFAC Proc., pp. 569-574 (2007).

Viviani A. *et al*., *Aeroshape design of reusable re-entry vehicles by multidisciplinary optimization and computational fluid dynamics*, Aerospace Science and Technology (2020a).

Viviani A. *et al*., *Low speed longitudinal aerodynamics of a blended wing-nody re-entry vehicle*, Aeroshape Science and Technology (2020b).

Viviani A., Iuspa L., Aprovitola A., *An optimization-based procedure for self-generation of re-entry vehicles shape*, Aerospace Science and Technology, pp. 123-134 (2017a).

Viviani A., Iuspa L., Aprovitola A., *Multi-objective optimization for re-entry spacecraft conceptual design using a free-form shape generator*, Aerospace Science and Technology, pp. 312-324 (2017b).

Walter U., *Astronautics, The Physics of Space Flights, third edition*, Switzerland: Springer International Publishing, 2018.

Zhao D.J., Song Z.-Y., *Reentry trajectory optimization with waypoint and no-fly zone constraints using multiphase convex programming*, Acta Astronautics, pp. 60-69 (2017).

Zhou H., Wang X., Cui N., *Glide guidance for reusable launch analytical dynamics*, Aerospace science and Technology, pp. 377-386 (2020).

OPTIMIZAREA MULTI- DISCIPLINARĂ A UNEI NAVE SPAȚIALE PENTRU COBORÂREA DE REINTRARE ÎN ATMOSFERĂ DE PE ORBITE TERESTRE JOASE LA O DENSITATE DE FLUX TERMIC CONSTANTĂ

(Rezumat)

Această lucrare se referă la analiza de prefezabilitate a unei noi abordări a etapei de reintrare în atmosferă de pe orbite terestre joase pentru misiunile spațiale cu om la bord pe baza unei conversii mai lungi și mai graduale a energiei interne a vehiculului în energie termică, ceea ce înseamnă păstrarea fluxului termic constant cât şi prezența unor valori termice de vârf mai coborâte. Aceasta implică posibilitatea utilizării unor materiale mai puțin performante și prin urmare, mai ieftine. Această abordare a fost dezvoltată pentru un concept înalt inovativ aripă-corp reutilizabil cu un raport mare suprafață/ masă. Un unghi al traiectoriei de zbor, cu valoare mai mică decât cel tipic Navetei spațiale, și anume -0.1 grade, este utilizat pentru a realiza disiparea graduală a energiei totale a vehiculului. Pentru a asigura nivelul fluxului termic convectiv pentru o anumită durată de timp, abordarea selectată a traiectoriei zborului utilizează o lege prescrisă de ghidare care modulează unghiul de atac al planorului ca functie de numărul Mach. În consecință, este realizată o procedură de optimizare dezvoltată pentru a păstra constant fluxul termic pe baza unei legi parametrice de ghidare.

BULETINUL INSTITUTULUI POLITEHNIC DIN IAŞI
Publicat de
Universitatea Tehnică „Gheorghe Asachi” din Iaşi
Volumul 68 (72), Numărul 1-4, 2022
Secţia
ŞTIINŢA ŞI INGINERIA MATERIALELOR

PRELIMINARY RESEARCH ON THE USE OF SYNTHETIC MAGNETITE IN THE CONSERVATION AND RESTORATION OF ARCHAEOLOGICAL IRON. STUDY ON THE POSSIBILITY OF USING FERROFLUIDS BASED ON SYNTHETIC MAGNETITE AS POLISHING MEDIA

BY

ILIE COJOCARIU[*]

“Gheorghe Asachi” Technical University of Iași,
Faculty of Materials Science and Engineering, Iași, Romania

Received: June 21, 2022
Accepted for publication: July 29, 2022

Abstract. In this paper, we study the state of art and some possibilities of using ferrofluids based on synthetic magnetite, as a polishing media for archaeological iron objects in particular. The purpose of this treatment is to prepare the surfaces to be varnished, but also to ensure their resistance to further corrosion.

The principle of the method is to immerse the objects to be treated in this way in a ferrofluid which is agitated in a magnetic, ultrasonic or mechanical field. The ferrofluids used may contain, in addition to magnetic particles, other non-magnetic abrasive particles (synthetic quartzite in this case). The transport liquid may be non-ionic (aromatic solvents, oils) or ionic (distilled water or solutions of acids or bases), compatible with the chemical character of the particles used. Suspended particles show their abrasive character on the microsurfaces, resulting in their superfinishing.

The synthetic magnetite used is obtained by coprecipitation, using methods that require two precursors and methods that require a single precursor and reducing or oxidizing agents for the second precursor. Coprecipitation reactions

[*]*e-mail*: ilie.cojocariu@student.tuiasi.ro

take place either at room temperature or at high temperatures (<90ºC). Magnetite synthesized in this way is used raw, or is chemically stabilized with citric acid, as a surfactant, to obtain the characteristics of a ferrofluid.

Quartzites used as additional abrasive material are obtained by acid precipitation of sodium silicate and are kept in suspension by magnetic particles as a result of the properties of ferrofluids.

The study in this paper analyzes the effectiveness of the method in terms of an optimal formulation of a ferrofluid with high durability and controlled chemical composition.

This method allows the simultaneous polishing of all surfaces of the object, regardless of their complexity or location (exterior or interior). In the case of iron objects of archaeological origin, the effectiveness of this treatment can be studied by optical microscopy (especially in polarized light) or electron microscopy.

Keywords: Archaeological iron, conservation, restauration, ferrofluids, magnetite, polishing media.

1. Introduction

The method proposed for study in this paper involves immersing objects to be polished in a medium (a ferrofluid in this case) containing abrasive particles of nanometer size. The whole assembly is stirred in a magnetic, ultrasonic or mechanical field. The main purpose of this treatment is to improve the corrosion resistance by superfinishing the micro-surfaces to the level of metal grains. The luster obtained in such operations has a secondary role.

A ferrofluid is a fluid consisting of ferromagnetic, ferromagnetic, or paramagnetic colloidal particles suspended in a carrier liquid, which may be chemically organic or inorganic. I chose ferrofluids based on synthetic magnetite because they have some special features. These ferrofluids react under the action of external magnetic fields, and can be actuated by them.

Ferrofluids, like any nanofluid, are characterized by the fact that Brownian agitation exceeds the natural tendency of sedimentation due to gravity, and in the case of synthetic magnetite, it can be further stabilized by surfactants. The type of surfactant is very important, because the final stability depends on it (Petrenko *et al.*, 2018; Vasilescu *et al.*, 2018). This chemical stabilization reduces the tendency of agglomeration by the appearance of repulsive forces (electrostatic or steric repulsions) between the individual particles, as well as between the individual particles and the vessel walls. The stability of the ferrofluid increases, and there are areas of minimal magnetic interaction between the particles, where non-magnetic or magnetic abrasive particles can be kept in equilibrium other than those in the composition of the ferrofluid.

The magnetoreological finishing is different from the proposed process, because the fluids change their viscosity under the action of a magnetic field of variable intensity, applied between the polishing tool and the workpiece. In his work, (Mutalib *et al.*, 2019) the main methods of magnetoreological finishing and the characteristics of the fluids used are described.

There are essential differences between ferrofluids and magnetorheological fluids. (Vékás, 2008) Ferrofluids contain particles with nanometric dimensions (15-100 nm), while in magnetorheological fluids they are of the order of micrometers (1-20 μm). In ferrofluids the maintenance of suspended particles is attributed to Brownian motion, while in magnetorheological fluids, it depends only on the evolution of the external magnetic field. Brownian motion is negligible in this case. Also, the aggregation of particles in magnetorheological fluids is more intense and reversible, being their main feature.

2. Materials and Methods

2.1. Materials and reagents

The following materials and reactants were used for the synthesis of synthetic magnetite in the form of nanoparticles: anhydrous ferric chloride ($FeCl_3$, purity 99.98%, from Lach-Ner); ferrous sulfate ($FeSO_4 \cdot 7H_2O$, 98% purity, from Chemical Company); Mohr salt ($(NH_4)_2$ Fe $(SO_4)_2$ $.6H_2O$, 99.7% purity, from Chemical Company); ammonium hydroxide or aqueous ammonia solution (NH_4OH, concentration 25%, from Chemical Company); sodium hydroxide (NaOH, purity 98.5%, from Chemical Company); potassium iodide (KI, 99.5%, from Chemical Company); perhydrol (H_2O_2, 30%, from Chemical Company).

Sodium silicate, transparent, of technical purity and specific gravity 1.4 kg/liter was used as raw materials for the synthesis of synthetic quartzites: citric acid ($C_6H_8O_7$, 99.5% purity, from Sigma-Aldrich).

Ferric chloride is used as a precursor to the ferric ion, Fe (III), and ferrous sulfate and Mohr salt are used as precursors to the ferrous ion, Fe (II). Ammonium hydroxide or sodium hydroxide are the reactants used in the coprecipitation reaction. Potassium iodide and perhydrol are another category of reactants, acting as reducing or oxidizing agents, if only one kind of precursor (for Fe (III) or for Fe (II)) is initially used, the other precursor being to be obtained by partial reduction or oxidation of the original precursor.

Sodium silicate is used as a precursor for the synthesis of synthetic quartzites by acid precipitation with citric acid solution.

2.2. Synthesis of Fe3O4 nanoparticles

The method used for the synthesis of magnetite is by coprecipitation, from aqueous solution (Schwaminger *et al.*, 2020).

2.2.1. Magnetite from two precursors

The precursors used, anhydrous ferric chloride ($FeCl_3$) and ferrous sulfate ($FeSO_4$. $7H_2O$), will supply the two species of iron ions, trivalent (Fe^{3+}) and divalent (Fe^{2+}). Their atomic ratio must be Fe^{3+} / Fe^{2+} = 2/1.

Some authors, (Sadighian *et al.*, 2021) weigh the gram equivalent of the required amounts of moles of substance. For a lighter and more accurate, volumetric dosing, we prepared the initial solutions with molar concentrations (for example, a 0.1M $FeCl_3$ solution and a 0.1M FeSO4*7H_2O solution. 0.1M, etc.). Equal volumes of these solutions will contain equal amounts of substance, in moles. Thus, we mixed 200 ml of 0.1M $FeCl_3$ solution and 100 ml of 0.1M $FeSO_4$*7H_2O solution. This mixture contains a mixture of iron ions Fe^{3+} / Fe^{2+} = 2/1, as it contains 0.2 x 0.1 moles of ferric chloride and 0.1 x 0.1 moles of hydrated ferrous sulphate.

In this solution, heated to 80°C and then homogenized by ultrasound, ammonium hydroxide (NH_4OH, 25%) is added dropwise. The rate of magnetite synthesis depends on the rate of addition of the reactant. The reactions that take place are the following:

$FeCl_3$ (aq) Ferric chloride (Iron (III) chloride)	+	$3NH_4OH$ (aq) Ammonium hydroxide	→	**$Fe(OH)_3$** (s) Ferric hydroxide (Iron (III) hydroxide	+	$3NH_4Cl$ Ammonium chloride	(1)
$FeSO_4$ (aq) Ferrous sulphate (Iron (II) sulphate	+	$2NH_4OH$ (aq) Ammonium hydroxide	→	**$Fe(OH)_2$** (s) Ferrous hydroxide (Iron (II) hydroxide	+	$(NH_4)_2SO_4$ Ammonium Sulphate	(2)

The general reaction:

2 $Fe(OH)_3$ (s) Ferric hydroxide (Iron (III) hydroxide	+	$Fe(OH)_2$ (s) Ferrous hydroxide (Iron (II) hydroxide	→	**Fe_3O_4** Magnetite (Iron (II/III) oxide	+	4 H_2O	(3)

In simplified form, the synthesis reaction of magnetite can also be written as:

$$Fe^{2+} + 2\,Fe^{3+} + 8\,OH^{-} \rightarrow Fe_3O_4 + 4H_2O \quad (4)$$

After completion of the reaction, the reaction vessel is kept at 80°C for another two hours, then allowed to cool to room temperature. The magnetite thus formed can be stored as such in the residual solution (mixture of ammonium chloride and ammonium sulphate), but presents the risk of agglomeration (clustering), or it can be washed with distilled water by known processes (magnetic separation and elimination by-products by repeated rinsing). Mohr salt can be used instead of ferrous sulphate, a double sulphate of iron and ammonium, also in the form of 0.1M solution. (Higher concentrations may be used, but all precursor solutions must have the same concentration).

Magnetite from two precursors

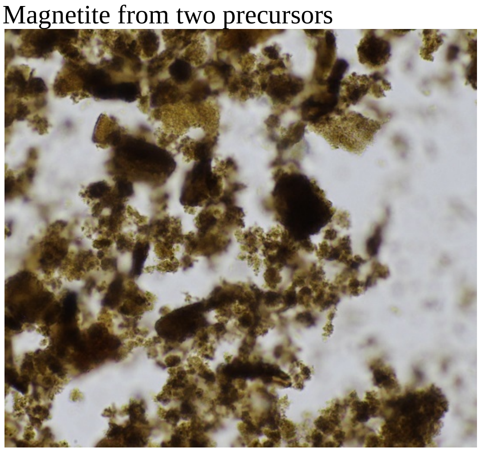

Fig. 1 – Clusters of magnetite (40 x photo).

2.2.2. Magnetite from a single precursor

There are methods of synthesizing magnetite using a single kind of precursor, which provides either the ferric ion or the ferrous ion. The second precursor is obtained from the first by reduction or oxidation reactions, as appropriate.

In the case of ferric chloride, potassium iodide (KI) or metallic iron (for example in the form of steel wool or iron filings) may be used as reducing precursors.

Using potassium iodide, the reduction from Fe(III) to Fe(II) follows the simplified reaction:

$$3\,Fe(III)(aq) + I^{-}(aq) \rightarrow 2Fe(III)aq + Fe(II)(aq) + 0.5I_2(s) \quad (5)$$

By mixing 300 ml of $FeCl_3$ (0.1M) solution with 100 ml of 0.1M KI, a solution is obtained in which the atomic ratio of $Fe^{3+} / Fe^{2+} = 2/1$ will be met, as 200 ml of FeCl3 will provide 0.2 x 0.1 mole containing Fe(III), and the remaining 100 ml $FeCl_3$ will be reduced by KI to a precursor containing 0.1 x 0.1 mole Fe(II). The coprecipitation and synthesis reaction of magnetite takes place by the addition of ammonium hydroxide, as in the case of the use of two initial precursors. Temperatures can be between room temperature and 80°C, and pH = 9÷11. Reaction by-products are removed by the usual magnetic separation processes and multiple rinses.

The reduction of ferric chloride with metallic iron in the form of steel wool or iron filings, proceeds according to the reaction:

2 $\mathbf{FeCl_3}$ (aq)	+	**Fe** (s)	→	3 $\mathbf{FeCl_2}$ (aq)	(6)
Ferric Chloride		Iron metal		Ferrous Chloride	
(Iron (III) chloride)				(Iron (II) chloride	

In practice, add amounts of metallic Fe over the $FeCl_3$ solution, until completely reduced.

The end of the reaction is indicated by the change in color to green or blue, depending on the concentration used and may take several hours. Exact stoichiometric calculations cannot be made because the overall reaction is more complex. As ferrous chloride ($FeCl_2$) is formed, the thermodynamic conditions for magnetite synthesis are also met. Part of the initial ferric chloride reacts with the newly formed ferrous chloride, the result, visible, being the decantation of magnetite. This phenomenon was observed when using a 0.1M solution of $FeCl_3$, at room temperature, without adding another reactant (ammonium hydroxide or sodium hydroxide). If the reaction vessel is closed and the chlorine cannot leave the system, the reaction described above is complete until the ferric chloride is completely depleted.

Magnetite from $FeCl_3$ and steel wool

Fig. 2 – Initially.

Fig. 3 – After four hours.

Finally, ferrous chloride, water, magnetite, and excess metallic iron are found in the reaction vessel.

Magnetite from $FeCl_3$ and steel wool

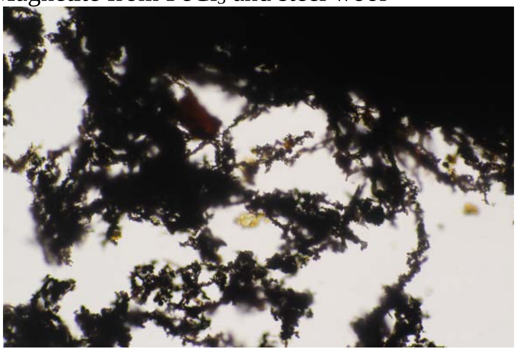

Fig. 4 – Magnetite retains the shape of the iron from which it comes. (40 x photo).

By filtration, the ferrous chloride can then be used as a precursor in the synthesis of magnetite by coprecipitation. Prolonged storage of the FeCl2 solution thus obtained results in the decantation of a quantity of akaganeite and the oxidation to iron oxychloride (FeOCl), which in turn is unstable in water or atmospheric humidity, with the formation of FeOOH and hydrochloric acid. The oxygen in the atmospheric air can be replaced by the oxygen provided by perhydrol, and thus ferrous chloride can be used as the only initial precursor in the synthesis of magnetite.

Magnetite synthesis reactions by partial oxidation of ferrous chloride are:

$$Fe^{2+} + 2\,(OH)^- \rightarrow Fe(OH)_2 \quad (7)$$

$$3\,Fe(OH)_2 + 0.5\,O_2 \rightarrow Fe(OH)_2 + 2\,FeOOH + H_2O \quad (8)$$

$$Fe(OH)_2 + 2\,FeOOH \rightarrow Fe_3O_4 + 2\,H_2O \quad (9)$$

2.3. Synthesis of synthetic quartzites

A straightforward process for the synthesis of quartzites (high purity SiO_2 particles) is the acid precipitation of sodium silicate. The acid used may be hydrochloric acid (Rahman and Padavettan, 2012), or sulfuric acid (Hernández-Palomares and Espejel-Ayala, 2022), but virtually any mineral or organic acid can lead to the precipitation of silica from sodium silicate. I chose citric acid because it is also the surfactant used to stabilize magnetite.

The precipitation reaction follows the relation:

$$\underset{\text{Sodium silicate}}{3\,Na_2SiO_3} + \underset{\text{Citric acid}}{2\,C_6H_8O_7} \rightarrow \underset{\text{Silica (quartzite)}}{3\,SiO_2} + \underset{\text{Sodium citrate}}{2\,Na_3C_6H_5O_7} + 3H_2O \qquad (10)$$

The size of these quartzites must be small enough to be supported in suspension by the Brownian motion and the specific repulsive forces that occur in ferrofluids, but large enough to have an abrasive effect on the surfaces they come in contact with. Several factors such as sodium silicate solution concentration, stirring speed, citric acid solution concentration, working temperature, can influence the size of these particles and also tend to agglomerate.

A technically pure sodium silicate solution with a specific gravity of 1.4 kg / liter was used. Distilled water was used for dilution in various proportions. A 10% citric acid solution was used for precipitation, initially, then 5%, 2% solutions were tested. The stirring was performed mechanically, ultrasonically and combined. Initially, gels of various consistencies are obtained which, by drying in air under normal conditions, collapse, and fragment, having a high degree of fragility.

The settling times in the distilled water for each of the products thus obtained and previously ground shall be timed. Dimensional sorting can be done by fractional decantation.

Synthetic quartzites (particles left in suspension)

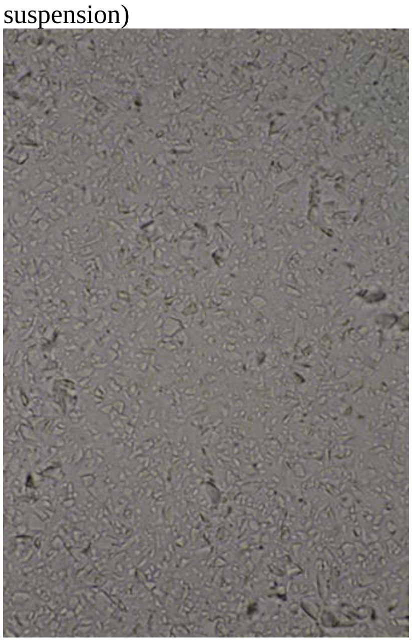

Fig. 5 – After 3 minutes.

Fig. 6 – After 60 minutes.

2.4. Preparation of ferrofluids based on synthetic magnetite

The main role of the ferrofluids studied in this paper is to support in suspension the abrasive particles (quartzites) and to agitate the transport fluid. The agitation of the ferrofluid can be magnetic, ultrasonic, or mechanical. Two types of synthetic magnetite-based ferrofluids will be studied: chemically stabilized and non-stabilized.

It is expected that synthetic magnetite nanoparticles stabilized with a surfactant will not show an abrasive effect on surfaces due to the appearance of those repulsive forces between individual particles or between particles and vessel walls, having a lubricating rather than abrasive effect. The abrasive effect can be improved by adding abrasive particles of different hardness. In particular, will be studied the abrasive effect of simple, unstabilised ferrofluids (transport fluid only at different pH and unstabilized magnetite) and of stabilized ferrofluids with citric acid and the addition of abrasive particles (transport liquid at various pH, quartzite and / or unstabilized magnetite).

A ferrofluid with synthetic magnetite and quartzite

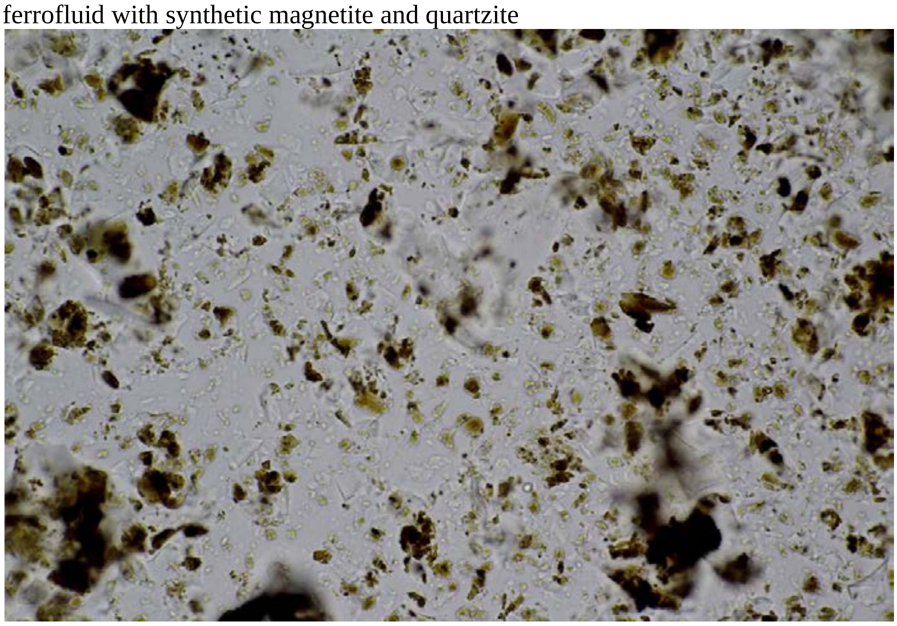

Fig. 7 – Magnetite clusters covered with quartzite and excess quartzite (40 x photo).

3. Analysis of results

3.1. Microscopic analysis in polarized light

The microscopic study in polarized light of the structure of metallic materials is based on the fact that while the reflection of plane polarized light on polished and chemically unattached surfaces of anisotropic optic bodies obtains elliptical polarized light, the reflection of plane polarized light by polished and chemically unattached surfaces of optically isotropic bodies no elliptically polarized light is obtained. From an optical point of view, metals with a cubic crystallization network are optically isotropic, anisotropic being metals with a tetragonal, rhombic, or hexagonal crystallization network. In the case of iron, freshly polished samples are optically isotropic, and most iron oxides are optically anisotropic.

Using crossed Nicols on an optical isotropic sample (cubic metal), not chemically attacked, results in extinction (the microscopic field is dark), which is maintained by rotating the sample around the optical axis of the microscope. In contrast, using crossed Nicols on an anisotropic optical metal grain, it appears bright, and when the sample rotates around the optical axis of the microscope, the metal grains periodically change their brightness, with 4 positions of maximum brightness and 4 positions of extinction.

By this method can be observed both the appearance (initiation) of corrosion, by the appearance of thin, optically anisotropic layers on the iron surface (initially optically isotropic), but also their elimination by superfinishing in ferrofluids based on synthetic magnetite.

3.2. Electron microscopy

Electron microscopy has the following advantages: with SEM, structural details become available up to the nanometer scale. This allows accurate characterization of microscopic defects or nanoscale deviations from process specifications that could not be observed with other instruments. High resolution is often important in quality control. We can observe on a micro and nanometric scale, obtaining vital information on the quality of surfaces. For this purpose, the Phenom ProX electron microscope will be used, from the endowment of the Conservation and Restoration Laboratory of Putna Monastery. The surface details can be studied up to optical magnifications of 27 - 160 X, and electronically, to magnitudes between 160 - 350000 X.

Preliminary research on the synthesis of magnetite, the synthesis of synthetic quartzites and ferrofluids based on synthetic magnetite was carried out using an Olympus CX 33 optical microscope, up to 40 X optical magnitudes, to which were added the magnifications obtained by digital zoom.

4. Study case

The case study was carried out on a batch of approximately 20 globular buttons, discovered in a voivodship necropolis from the Church of St. Elijah Suceava, 2019 campaign. (Unpublished, currently being published by Prof. Ion Mareș, archaeologist).

Two types of ferrofluids based on synthetic magnetite and synthetic quartzite were used:

1. The first, composed of distilled water, magnetite, quartzite, and non-ionic detergent (P100), pH = 6-7 for the removal of humic residues and physical-mechanical adhesions.

2. The second, composed of distilled water, magnetite, quartzite and ammonium hydroxide, pH = 12-14. (For removal of copper-specific corrosion products).

Both ferrofluids were stirred in an ultrasonic bath. The total treatment time was about 15 minutes. After this preliminary treatment, it is possible to determine the composition of the constituent alloy and to determine the nature of the corrosion products remaining on the surface of the buttons (possibly Fe).

Fig. 8 – Before treatment.

Fig. 9 – Intermediate phase.

The treatment will continue until obtaining surfaces that give an aesthetic aspect but also ensure the long-term stability of the objects.

5. Conclusions

The aim of this study was to obtain synthetic magnetite and synthetic quartzites from precursors by simple laboratory methods. This allows the formulation of ferrofluids in which synthetic magnetite can be stabilized or unstabilized, of strictly controlled composition (very important).

The transport liquid can cover the entire pH scale, depending on the specifics of the situation.

It is a "smooth" process, as no additional pressure is used on the treated object.

Both exterior and open interior surfaces can be polished simultaneously.

Unstabilized ferrofluids could have an abrasive effect on surfaces they come in contact with, similar to cleaning technologies in the jewelry industry, but on a nanometric or micrometric scale. (With Magnetic Polishing Machine, Polishing Vibratory Machine, Rotary Tumbler Polishing Mashine, and other).

REFERENCES

Hernández-Palomares A., Espejel-Ayala F., *Precipitated silica, alkali silicates and zeolites from construction and demolition waste materials*, Journal of Cleaner Production, 348 (March), 131346 (2022), doi: 10.1016/j.jclepro.2022.131346.

Mutalib N.A. *et al.*, *Magnetorheological finishing on metal surface: A review*, IOP Conference Series: Materials Science and Engineering, 469(1) (2019), doi: 10.1088/1757-899X/469/1/012092.

Petrenko V.I. *et al.*, *On the impact of surfactant type on the structure of aqueous ferrofluids*, Colloids and Surfaces A: Physicochemical and Engineering Aspects, 541, 222-226 (2018), doi: 10.1016/J.COLSURFA.2017.03.054.

Rahman I. A., Padavettan V., *Synthesis of Silica nanoparticles by Sol-Gel: Size-dependent properties, surface modification, and applications in silica-polymer nanocompositesa review*, Journal of Nanomaterials, (2012), doi: 10.1155/2012/132424.

Sadighian S. *et al.*, *A Facile Synthesis of Fe 3 O 4 @SiO 2 @ZnO for Curcumin Delivery*. (2021), doi: 10.33263/BRIAC126.79948002.

Schwaminger S.P., Syhr C., Berensmeier S., *Controlled Synthesis of Magnetic Iron Oxide Nanoparticles: Magnetite or Maghemite?*, *Crystals*, 10(3), 214 (2020), doi: 10.3390/cryst10030214.

Vasilescu C. *et al.*, *High concentration aqueous magnetic fluids: structure, colloidal stability, magnetic and flow properties*, *Soft Matter*, 14(32), 6648-6666 (2018), doi: 10.1039/C7SM02417G.

Vékás L., *Ferrofluids and magnetorheological fluids*, CIMTEC 2008 - Proceedings of the 3rd International Conference on Smart Materials, Structures and Systems - Smart Materials and Micro/Nanosystems, 54, 127-136 (2008), doi: 10.4028/www.scientific.net/AST.54.127.

CERCETĂRI PRELIMINARE PRIVIND UTILIZAREA MAGNETITEI SINTETICE ÎN CONSERVAREA ȘI RESTAURAREA FIERULUI ARHEOLOGIC. STUDIU PRIVIND POSIBILITATEA UTILIZĂRII FEROFLUIDELOR PE BAZĂ DE MAGNETITĂ SINTETICĂ CA MEDII DE LUSTRUIRE

(Rezumat)

În această lucrare, studiem stadiul actual și unele posibilități de utilizare a ferofluidelor pe bază de magnetită sintetică, ca mediu de lustruire, în special pentru obiectele arheologice din fier. Scopul acestui tratament este de a pregăti suprafețele ce urmează a fi lăcuite, dar și de a asigura rezistența acestora la o coroziune ulterioară.

Principiul metodei constă în a scufunda obiectele de tratat, într-un ferofluid care este agitat într-un câmp magnetic, ultrasonic sau mecanic. Ferofluidele utilizate pot conține, pe lângă particulele magnetice, și alte particule abrazive nemagnetice (cuarțit sintetic în acest caz). Lichidul de transport poate fi neionic (solvenți aromatici, uleiuri) sau ionic (apă distilată sau soluții de acizi sau baze), compatibil cu caracterul chimic al particulelor utilizate. Particulele în suspensie își manifestă caracterul abraziv pe microsuprafețe, rezultând suprafinisarea lor.

Magnetita sintetică utilizată se obține prin coprecipitare, folosind metode care necesită doi precursori și metode care necesită un singur precursor și agenți reducători sau oxidanți pentru cel de-al doilea precursor. Reacțiile de coprecipitare au loc fie la temperatura camerei, fie la temperaturi ridicate (<90ºC). Magnetita astfel sintetizată este folosită brută, sau este stabilizată chimic cu acid citric, ca surfactant, pentru a obține caracteristicile unui ferofluid.

Cuarțitele utilizate ca material abraziv suplimentar sunt obținute prin precipitarea acidă a silicatului de sodiu și sunt ținute în suspensie de particule magnetice ca urmare a proprietăților ferofluidelor.

Studiul din această lucrare analizează eficacitatea metodei în ceea ce privește obținerea unei formule optime a unui ferofluid cu stabilitate ridicată și compoziție chimică controlată.

Această metodă permite lustruirea simultană a tuturor suprafețelor obiectului, indiferent de complexitatea sau locația acestora (exterior sau interior). În cazul obiectelor din fier de origine arheologică, eficacitatea acestui tratament poate fi studiată prin microscopie optică (în special în lumină polarizată) sau microscopie electronică.

BULETINUL INSTITUTULUI POLITEHNIC DIN IAŞI
Publicat de
Universitatea Tehnică „Gheorghe Asachi" din Iași
Volumul 68 (72), Numărul 1-4, 2022
Secţia
ŞTIINŢA ŞI INGINERIA MATERIALELOR

METALLIC MATERIALS WITH DAMPING CAPACITY FOR AUTOMOTIVE APPLICATIONS

BY

TEODORA IRINA BIRNOVEANU[1,*], SEBASTIAN MISTREANU[1], ANA MARIA SCRIPCARIU[1], ANA-MARIA ROMAN[1], CIPRIAN PARASCHIV[2] and NICANOR CIMPOEŞU[1]

[1]"Gheorghe Asachi" Technical University of Iași,
Department of Materials Science and Engineering, Iași, Romania
[2]"Grigore T. Popa" University of Medicine and Farmacy, Iași, Romania

Received: August 8, 2022
Accepted for publication: September 12, 2022

Abstract. Some metallic materials present a high damping capacity that can be used in various industrial applications. The damping capacity of materials is directly connected to internal friction of the materials. The technique follows the extreme behavior of metals such as high or low internal friction. In physics, the study of internal friction serves to better understand the dynamics of crystal networks, providing an easy way to determine the diffusion coefficients, to measure the solubility of solid solutions and low concentrations of impurities, to investigate the network and the interaction between them and not only them. Internal friction studies primarily aim to use damping capacity as a means of studying internal structure and atomic motion in solids. The method provided information on the diffusion, ordering and solubility of interstitial atoms and was used to determine the density of dislocations. The vibration amplitudes used in this type of research are small and the stresses that occur are low. Another aspect of the research is the determination of the values used in the technique, in terms of energy dissipation in the parts subject to vibrations. The research refers to the determination of the damping capacity of the material, in the case of relatively large amplitudes encountered in practice.

Keywords: damping capacity, internal friction, metallic materials.

[*]Corresponding author; *e-mail*: irinasofi@yahoo.com

1. Introduction

A vibrating body, completely isolated from the environment, has the property to convert the mechanical energy of vibration into heat and it is called internal damping or friction. The first term is used by engineers, the second by physicists (NHTSA, 1990).

If metals act as perfectly elastic materials when required by nominal forces situated below the limit of elasticity, there will be no internal friction. However, the fact that the damping effects can be observed at stress levels much lower than the elastic limit shows that metals have a low real elastic limit, if such a limit exists. The effects of internal friction (or damping) are manifested by the appearance of a phase difference between the applied voltage and the resulting specific deformation. This process appears due to the application of low voltages, and atomic, thermal or magnetic rearrangements (Huang, 2002). A significant area of inelastic behavior is known as inelasticity. This problem is related to the effects of internal and independent friction of the amplitude of the vibration. The inelastic behavior occurs due to thermal diffusion, atomic diffusion, relaxation of stresses in the grain boundary areas, ordering due to stresses and magnetic interaction. Some static phenomena such as the post-elastic effect are related to inelastic behavior. The internal friction resulting from cold plastic deformation depends very much on the amplitude, so it is not an inelastic phenomenon (Sapuan *et al.*, 2005). Experience shows the free oscillations of a body dampen over time. Ignoring the contribution of the external environment to the attenuation of oscillations, its causes reside inside the solid and are called "internal friction". Sound absorption in solids, damping of the free oscillations of a torsion pendulum is due to internal friction. During the damping of free oscillations, the macroscopic and mechanical energy is gradually transformed, and is taken over by macroscopic systems of atoms or even isolated atoms, causing an equivalent amount of heat. The internal friction processes are therefore irreversible (Sapuan *et al.*, 2005).

In the conditions of a forced situation, in which the specimen is made to vibrate at a constant amplitude, a measure of the internal friction is the relative decrease in the energy on each cycle. The vibration energy is proportional to the square of the amplitude, so that the logarithmic decrement can be expressed by the relation:

$$\delta = \frac{\Delta W}{2W} \tag{1}$$

Where: ΔW is the energy loss per cycle, and W is the vibration energy at the beginning of the cycle.

In the case of performing experiments by forced vibrations, it is customary to determine the resonance curve, and the logarithmic decrement for a resonance curve is given approximately by the relation:

$$\delta = \frac{\pi(f2-f1)}{fr} \tag{2}$$

It is necessary to obtain an expression of the damping capacity of the material based on the temperature / time gradient. For low depreciation values, the loss factor is related to other definitions of depreciation through the following relationships in accordance with (Cole and Sherman, 1995).

$$Q^{-1} = \frac{\psi}{2\pi} = \eta = \frac{\delta}{\pi} = tan\phi = \frac{E''}{E'} = 2\xi = \frac{\Delta W}{2\pi W} \quad (3)$$

Where: Q^{-1} - quality factor; Ψ - specific depreciation; E' - modulus of elasticity; E'' - loss module; η - loss factor; δ - logarithmic decrement; ξ - depreciation ratio; W - the energy introduced into the system during the charging of a cycle.

An expression is given for the loss factor and the total mechanical energy input will be compared to the energy dissipated by the material. Next, it is assumed that the stress is in the elastic domain and in connection with the deformation by the modulus of elasticity $\sigma = \varepsilon \bullet E$, the deformation is defined as $\varepsilon = S / L$, ε - deformation, S - displacement and L - length.

Energy can be expressed as mechanical work:

$$W = \int F dx \quad (4)$$

Where: W is the mechanical work, F - the imposed force and x - the coordinate of the chamber or the energy can be expressed as heat: $W = Tc_pV \bullet \rho$ (where: T - temperature, c_p - latent heat, V - sample volume and ρ - density).

The loss factor is defined as ΔW / $2\pi W$ where ΔW represents the mechanical work transformed into heat during a charging cycle and W represents the total elastic energy introduced into the system during a charging cycle (Murphy, 1998).

The mechanical energy introduced into the system per unit time is given by the following equation and multiplied by the frequency f:

$$W_{mec} = f \int_0^S F dx = \left\{ dx = L\frac{DF}{AE} \right\} = F \int_A^F \frac{FL}{AE} dF = f\,\frac{F^2L}{2AE} \quad (5)$$

The energy transformed into heat per unit time is given by the exchange of temperature by its derivative in the following equation:

$$W_{înc} = \frac{dT}{dt} c_p V_\rho = \frac{dT}{dT} c_p AL\rho \quad (6)$$

Where: dT / dT represents the heating rate, A - the area per section and L - the length of the bar.

Using the previous expressions, we obtain:

$$\eta = \frac{(dT/dt)c_pAL\rho}{2\pi f(F^2L/2AE)} = \frac{(dT/dt)c_pA^2\rho E}{\pi f F^2} \quad (7)$$

The equation shows that for a particular material with known thermo-physical properties, geometry and test parameters, the derivative time/temperature has a value on the damping of the material.

In the last decade, specialists in the field of intelligent materials, especially those studying shape memory alloys, have noticed a new property that has not been investigated or applied until now. This ability to dissipate mechanical energy is called by specialists as high internal friction.

Shape memory alloys, especially those based on copper, have high internal friction compared to other metallic materials, especially in the field of transformation temperatures (Davoodi *et al.*, 2008a). Below are some results from current studies conducted on shape memory alloys, following internal friction.

The transformation temperatures and the characteristics presented by the shape memory alloys vary greatly depending on the changes in composition and allow their classification into three groups according to the transformation temperatures they possess.

The first group consists of alloys with transformation temperature (TM) below room temperature and certainly far from the Curie temperature (-TC that is close to 370 K in most alloys). The third group contains alloys with TM > TC while the alloys in the second group are intermediate, with the transformation temperature close to room temperature (Murphy, 1998).

The classic internal friction behavior is represented by an internal friction peak together with a minimum of elasticity modulus, occurring in the temperature range of martensitic transformations and, in the special case of a thermoelastic martensite appears a big internal friction peak in the martensitic state.

For a material undergoing a phase transformation with the coexistence of two phases over a given temperature range, the total value of the internal friction peak results from three contributions, as shown in Eq. (8) (Motors General, 1992).

$$IF_{tot} = IF_{tr} + IF_{PT} + IF_{int} \tag{8}$$

Where: IF_{int} represents the intrinsic damping part of two coexisting phases; IF_{tr} is the contribution of the internal friction of passage between phases and occurs only with a temperature variation, being related to kinetic transformations; IF_{PT} is the contribution of internal friction different from that due to phase transformation, regardless of temperature and occurs only during the structural transformation of the alloy.

The contribution of the internal transition friction (IF_{tr}) has the most important contribution to the formation of the internal friction peak ("peak") for low frequencies (approx. 1Hz). This part of the internal friction depends on external parameters such as the amplitude of the load, the frequency and speed of heating / cooling (Motors General, 1992).

2. The process of developing a new front bumper for the passenger car

The front bumper absorbs kinetic energy in the case of an accident by bending at low-speed impact and by deformation at high-speed impact. Due to the safety rules at different speeds, together with the environmental restrictions for old vehicles, the design level of complexity of the damping system has increased.

From the design phase, the new bar must be flexible enough to reduce the injuries of the passenger and occupant on the right side, but also to remain intact at low speed impact. It also must be strong enough to dissipate kinetic energy at a high speed impact. Reinforcing the bar plays an important role in passenger safety and also in increasing the possibility of using biodegradable and recyclable materials to reduce environmental pollution. Developing the right shape and a viable system of analysis procedures can prevent shape re-modification.

On the other hand, the analysis of most of the effective parameters that lead to higher resistance of the bar, increases the efficiency of production development. Cross section, longitudinal curvature, fastening method, rib thickness and strength are some of the significant design parameters in the production of the car front bumper.

The design of a metal element is the preliminary stage of product development and analysis. The stage of completion of the design process clearly predicts the failure (s) if any, before mass production. Passenger vehicles represent 90% of the registered group of vehicles.

In 2009, an estimated 9 640 000 vehicles were involved in police-reported accidents, 95% (9 161 000) being passenger vehicles. More than 45 435 of these vehicles were involved in fatal accidents and of which 80% (36 252) were passenger vehicles. More than 23 000 passengers in passenger cars lost their lives in road accidents in 2009 and an estimated 1.97 million people were injured (NHTSA, 1990).

Most of the studies mentioned above emphasize the nature and type of material but also the concept of selection and numerical analysis of the bumper. However, no article on the procedures for building a new car bumper can be found in the literature. That is why the research also focuses on the process of making the car bumper and completes the design and analysis methods for making new bars based on previous research. Consequently, in order to increase the performance of the impact bumpers, the correct procedure must be followed to achieve this situation. In this regard, emphasis can be placed on the parameters to be taken into account in the design, and finite element analysis procedures of the system that can be used.

3. Bar system

A bar system is a set of front and rear components of vehicles designed to moderate the kinetic energy without any damage to the vehicle in the event of a low- speed impact and to dissipate energy in the event of high speed conditions. It also serves for aesthetic and aerodynamic purposes (Johnson and Walton, 1983; Zhang *et al.*, 2009). The system that makes up the front bar consists mainly of three components: the mask, the heatsink and the bar (Sapuan *et al.*, 2005). The bumper system has changed over the past few decades due to new government safety rules and style concepts. The ability to keep the vehicle intact in high-speed impact conditions and to reduce the resulting kinetic energy are the most important factors in the selection of the bar system, in addition to weight, production process, cost, repair and machinability of materials (Fig. 1) (Alghamdi, 2000).

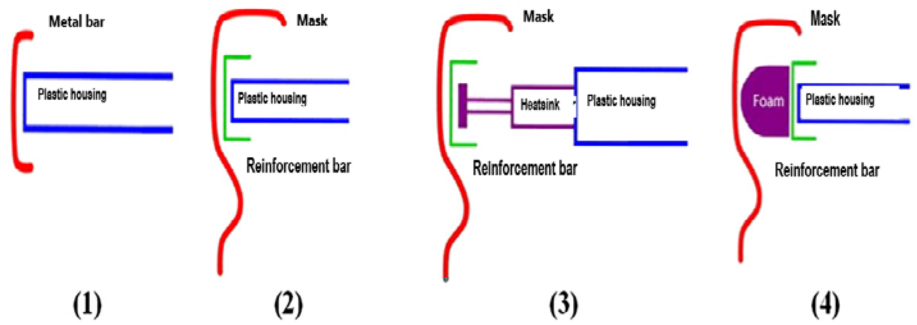

Fig. 1 – The American Institute of Iron and Steel offered several proposals for the bar system: (1) front metal bar, (2) plastic housing and reinforcing bar, (3) plastic housing, bar reinforcement and mechanical heatsinks and (4) plastic mask, foam heatsink, heatsink (AISI, 2006).

Therefore, this concept (refer to it as concept number 5) can be added to the four components of the bar system that the American Iron and Steel Institute (AISI) provided in 2003 (Fig. 2). This is a schematic view of a modified system concept from AISI for the car's bumper system.

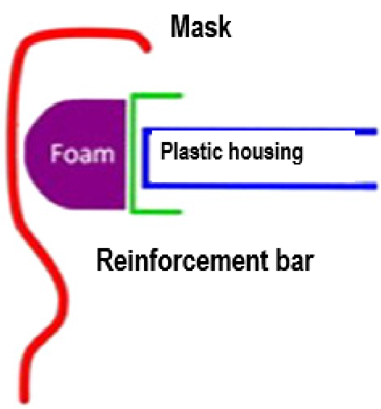

Fig. 2 – Schematic view of a modified system concept from AISI for the car's bumper system.

4. Pedestrian impact system, low intensity impact and damage impact

In this method, two types of heatsinks are considered: firstly, a low stiffness heatsink, so-called reversible heatsink, designed for low impact and pedestrian impact protection; and secondly, an energy sink, metallic or non-metallic, which can be destroyed on impact and is usually located behind the bar and attached to the main front bar.

The damping bar is the rear element of the energy absorption mechanism (Cheon, 1995).

It is usually located at the front and sometimes at the rear, on the sides of the vehicle.

However, the testing process for both parties is almost the same; the next system should be more durable than the previous one for driver safety. On the other hand, the current trend in the production of the bumper is based on aerodynamic efficiency where the realized curve should be combined in the same way in other parts of the bar system (AISI, 2006). The composite material solves this dilemma by providing the required curvature and several phases of the metal bar and decreases the weight of the bar (Miravete, 1993).

The effective parameters of structural energy absorption are longitudinal curvature, section profile (Davoodi *et al.*, 2011), metal slats (Davoodi *et al.*, 2012), thickness (Daniel *et al.*, 1999) and total cross-sectional dimensions (Kurtaran *et al.*, 2002).

Destruction resistance of the car and the bar system, which identifies the safety and performance of the car in response to impact, is another global challenge.

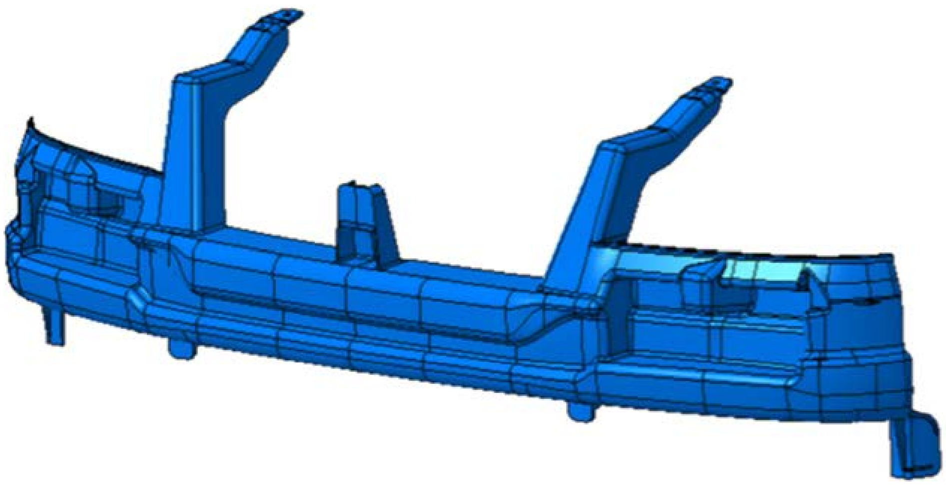

Fig. 3 – Damping bar system proposed by Samand (MehrCamPars, 2003).

If the magnitude of the discharge does not force the elastic region under low impact conditions, then the structure returns to its initial position after releasing the load (Davoodi *et al.*, 2008a; Davoodi *et al.*, 2008b).

However, if the impact load goes beyond the region of elastic resistance, then most of the collision load is absorbed by the plastic deformation (irreversible energy absorption).

The basic system should go beyond both scenarios and support the intense load resulting in high disadvantages and various interactions between different deformation modes, such as bending and stretching (Fig. 3) (Lu and Yu, 2003).

The proportion of energy absorbed by the bumper should also be satisfactory for high kinetic energy, which would preferably be dissipated by plastic deformation. In fact, the collision energy increases the stress energy in the structure and in turn releases the same kinetic energy that causes further damage to passengers and adjacent vehicles. Therefore, the structural energy of the bumper should be improved during the manufacturing process. Additionally, the ductility of the materials improves the energy absorption of the plastic. In this context, plastic compounds are used in the bumper system when the damping energy of the plastic and the weight are performance criteria and critical design (Lu and Yu, 2003; Sudin *et al.*, 2007).

5. Bumper manufacturing parameters

The emergence of new materials, products and the development process led to a rethinking of the structural design role and the effective parameters for their improvement.

The bumper can be improved by adding several effective parameters. The efficiency of the parameters can be identified by any number of methods, such as the production of experiments (DOE) (Isaksson *et al.*, 2010), optimizations (RBDO) (Fu *et al.*, 2004) and the production analysis of sensitivity. However, the current study is not intended to identify the viability of the parameters. Variables such as thickness, curvature of the bar, strength and section profile are some of the most important parameters that can improve the energy absorption of the bumper and support the desired deflection of the bar system as defined in the production design specifications (PDSs). The optimal thickness of the bumper can strike a balance between the weight and strength of the structure to provide effective energy absorption (Baccouche *et al.*, 2007).

The nominal thickness of the bar is generally 4 mm. In any case, it is not completely constant on all sides of the bar. The extra thickness occurs in products that also use polymeric materials that have certain manufacturing constraints.

6. Steel materials

Rolled steel in the form of plates is a material with many applications.

They are characterized by strength and rigidity with favourable mass-cost ratios and allow high-speed manufacturing due to their good machinability properties.

Additionally, they offer excellent corrosion resistance when coated, high energy absorption capacity, wear resistance, fatigue resistance, excellent paint and complete recyclability.

These characteristics, plus the availability of a high strength (ultra-strong steels), have made sheet steel a very common material used in the automotive industry. Numerous types of steel offer material designers various options for any given application. Steel bumpers with elongation of up to 50% facilitate forming operations. Steel bars with a breaking strength more than1900 MPa (280 ksi) also facilitate the reduction of the mass of the bar system.

The types of steel that are commonly used for front bars are presented together with the specific properties in Table 1. Most front bars are made of solid steel (deformation resistance greater than 240 MPa). Although duplex steels are not present in Table 1, successful attempts have been completed and the front bars can now continue with weight reduction.

Table 1

Types of steel for damping bars and their characteristic properties

Material	Type	Description	Typical Flow limit MPa	Tensile strength MPa	Typical elongation %	n Value	SAE Correspondence
HR	1008/1010	Small Carbon	269	386	35	0.19	J4031010
HR	35 XLF	Microalloy	331	407	35	0.17	J2329-2
HR	50 XLF	Microalloy	403	480	31	0.17	J2340 340x
HR	55 XLF	Microalloy	439	505	29	0.16	J2340 380x
HR	60 XLF	Microalloy	475	531	27	0.15	J2340 420x
HR	70 XLF	Microalloy	527	600	26	0.13	J2340 490x
HR	80 XLF	Microalloy	587	673	22	0.12	J2340 550x
CR	1008/1010	Small Carbon	296	331	35	0.2	J403 1010
CR	DR210	Resistant on small section	220	360	40	0.2	J2340 210
CR	35 XLF	Microalloy	285	400	35	0.17	J2329-2
CR	40 XLF	Microalloy	315	425	33	0.16	J2340 300X
CR	50 XLF	Microalloy	376	475	28	0.15	J2340 340X
CR	55 XLF	Microalloy	418	501	27	0.14	J2340 380X
CR	60 XLF	Microalloy	459	527	26	0.14	J2340 420X
CR	70 XLF	Microalloy	530	614	20	0.12	J2340 490X
SS	T301	Austenitic	276	758	60	0.45	J405S30100
SS	T204	Austenitic	370	689	59	0.44	J405S20400

HR: HOT ROLLED SHEET; CR: COLD ROLLED SHEET; 1008/1010: LOW CARBON STEEL; XLF: MICROALLOY; SS: STAINLESS STEEL.

For comparative, Table 1 also includes similar ESA categories. The SAE Society of Automobile Engineers designates the steel categories.

There are four of them and each number represents the standard chemical composition for the steel specification. These SAE categories are not equivalent categories. This means that there are many minor differences between the SEA categories and the common categories they resemble. The differences can be significant in some applications.

Some OEM categories are called categories that can be owned in kind. The front bars, thanks to the deep stamping and the complex shape, are produced through the stamping process. Highly formable steels are required and all categories shown in Table 1 can be supplied to meet the demanding requirements of the stamping process. The front bars are powder coated, painted or chrome plated and a high quality surface is required on the steel sheet. In addition, most of the steel sheets used for formed and chromed bars are evenly polished before the stamping process.

The categories of steel that are commonly used for reinforcements, supports and reinforcing beams, are presented along with their specific properties. Most reinforcement beams are made of high-strength steel [minimum tensile strength greater than 550 MPa (80ksi)].

7. Conclusions

The shape memory effect was observed in several classes of alloys, intensely manifested in Ni-Ti and Cu-based alloys. In recent decades, a new property with significant values has been observed in these alloys, especially those based on Cu, namely the ability to dissipate mechanical energy, a property found in all materials but with different value manifestations.

The main materials used in energy dissipation are polymeric materials, rubbers, which have very high values of internal friction, but which do not benefit from the properties of metallic materials. Therefore, observing the phenomenon in the shape memory alloys, a detailed investigation of them was sought. Obtaining shape memory alloys requires special processing conditions imposed by the necessary chemical composition, which must be strictly observed.

Additionally, for conventional casting methods, new methods such as melt centrifugation or powder metallurgy have also been successfully applied.

Along with the main properties of shape memory alloys, pseudoelasticity, simple shape memory effect, free return shape memory effect, retained shape memory effect, mechanical working generator or double shape memory effect, the mechanical energy dissipation capacity has found utility in many practical applications.

REFERENCES

AISI, *Steel bumper systems for passenger cars and light trucks*, Southfield: American Iron and Steel Institute (2006).

Alghamdi A., *Smart frictional impact energy absorber*, Int J Crashworthiness **5**, 169-178 (2000).

Baccouche R., Mahmood H., Madasamy C., Wagner D., *Lightweight bumper for automobiles*, Google patents (2007).

Cheon S., Choi J.H., Lee D.G., *Development of the composite bumper beam for passenger cars*, Compos Struct **32**, 4919 (1995).

Cole G.S., Sherman A.M., *Light weight materials for automotive applications*, Mater Charact **35**, 3-9 (1995).

Daniel L., Hogg P., Curtis P., *The relative effects of through-thickness properties and fibre orientation on energy absorption by continuous fibre composites*, Composites Part B. **30**, 257-266 (1999).

Davoodi M.M., Sapuan S.M., Ahmad D, Aidy A, Khalina A, Jonoobi M., *Concept selection of car bumper beam with developed hybrid bio-composite material*, J Mater Des **32**, 4857-4865 (2011).

Davoodi M.M., Sapuan S.M., Ali A., Ahmad D., *Effect of the strengthened ribs in hybrid toughened kenaf/glass epoxy composite bumper beam*, Life Sci J **9** (1), 210-213 (2012).

Davoodi M.M., Sapuan S.M., Yunus R., *Conceptual design of a polymer composite automotive bumper energy absorber*, J Mater Des **29**, 1447-1452 (2008a).

Davoodi M.M., Sapuan S.M., Yunus R., *Development of fiber reinforced epoxy composite energy absorber for automotive bumper system*, J Polym Mater **25**, 15-21 (2008b).

Fu Y., Chuang C.H., Li G., Yang R., *Reliability-based design optimization of a vehicle exhaust system*, SAE Trans **113**, 507-518 (2004).

Huang M., *Vehicle crash mechanics*, CRC Press (2002).

Isaksson E., Jonsén P., Sundin K., Oldenburg M., *Correlation of vehicle crash model parameters to car properties in low-speed collisions: a design of experiments approach*, Int J Crashworthiness **15**, 241-249 (2010).

Johnson W., Walton A., *An experimental investigation of the energy dissipation of a number of car bumpers under quasi-static lateral loads*, Int J Impact Eng **1**, 301-308 (1983).

Kurtaran H., Eskandarian A., Marzougui D., Bedewi N., *Crashworthiness design optimization using successive response surface approximations*, Comput Mech **29**, 409-421 (2002).

Lu G., Yu T., *Energy absorption of structures and materials*, Woodhead Pub. (2003).

MehrCamPars, *GMT bumper beam of Samand* (2003).

Miravete A., *ICCM/9: composites properties and applications*, Zaragoza: Woodhead Pub Ltd. (1993).

Motors General, *SMC bumper beams improve productivity for GM*, Reinf Plast **36**, 7 (1992).

Murphy J., *The reinforced plastics handbook*, Oxford: Elsevier (1998).

National Highway Teraffic Safety Administration (NHTSA), *Laboratory test procedure for regulation Part 581 bumper standard safety assurance* (1990).

Sapuan S., Maleque M., Hameedullah M., Suddin M., Ismail N., *A note on the conceptual design of polymeric composite automotive bumper system*, J Mater Process Technol **159**, 145-151 (2005).

Sudin M.N., Harun M.R., Hamzah A.T., Anuar S., *A prototype of KBS for material selection in bumper beam design*, J Sci Technol **14**, 215-222 (2007).

Zhang Z., Liu S., Tang Z., *Design optimization of cross-sectional configuration of rib-reinforced thin-walled beam*, Thin Walled Struct **47**, 868-878 (2009).

MATERIALE METALICE CU CAPACITATE DE AMORTIZARE PENTRU APLICAȚII AUTOMOTIVE

(Rezumat)

Unele materiale metalice prezintă o capacitate mare de amortizare care poate fi utilizată în diferite aplicații industriale. Capacitatea de amortizare a materialelor este legată direct de fricțiunea internă a materialelor. In tehnică se urmărește comportamentul extrem al metalelor ca frecare internă ridicată sau scăzută. În fizică, studiul fricțiunii interne servește pentru a înțelege mai bine dinamica rețelelor de cristal, oferind o modalitate ușoară de a determina coeficienții de difuzie, de a măsura solubilitatea soluțiilor solide și a concentrațiilor scăzute de impurități, de a cerceta rețeaua și interacțiunea dintre acestea și nu numai. Studiile privind fricțiunea internă urmăresc în primul rând utilizarea capacității de amortizare ca mijloc de studiere a structurii interne și a mișcării atomice în solide. Metoda a furnizat informații cu privire la difuzia, ordonarea și solubilitatea atomilor interstițiali și a fost utilizată pentru a determina densitatea dislocațiilor. Amplitudinile vibrațiilor utilizate în acest tip de cercetare sunt mici, iar tensiunile care apar sunt scăzute. Un alt aspect al cercetării este determinarea valorilor utilizate în tehnică, în ceea ce privește disiparea energiei în părțile supuse vibrațiilor. Cercetarea se referă la determinarea capacității de amortizare a materialului, în cazul amplitudinilor relativ mari care se întâlnesc în practică.